A Study of Jet Production in $\gamma\gamma$ Collisions at TRISTAN

Kazuko Adachi

Human Life and Environmental Science Course,
Graduate School of Human Culture,
Nara Women's University
Nara 630, JAPAN

June 1998

Ph.D Dissertation

Abstract

We have studied the jet production in quasi-real $\gamma\gamma$ collisions with the TOPAZ detector at TRISTAN e^+e^-collider (KEK). The data correspond to the integrated luminosity of 287.8 pb^{-1} at center-of-mass energy of 58 GeV and are almost full data taken with the TOPAZ detector. In this thesis, jets have been reconstructed using "cone algorithm". Various properties of dijet events in $\gamma\gamma$ collisions have been investigated in detail. The results can give important information to understand the features of quasi-real photon. We also have studied the jet profile using $\gamma\gamma$ collisions and e^+e^-annihilation events. Comparing the jet widths in these events with those in other reactions, such as γp collision and $p\bar{p}$ collision, almost all jet widths seem to obey a "simple scaling law" which has been suggested by theoretical aspect.

Acknowledgments

The analysis in this thesis has carried out as a part of the TOPAZ experiment at TRISTAN. First of all, I would like to express my cordial thanks to Prof. Seishi Noguchi, Prof. Hisaki Hayashii and Prof. Noboru Fujiwara for their instructive guidances and continuous encouragements throughout my graduate student course, and for their giving me an opportunity to participating to the TOPAZ experiment. I appreciate all the members of High Energy Physics Laboratory at Nara Women's University for their warm help.

I would like to thank to all staff and graduate students in the TOPAZ collaboration. Especially, great thanks are due to Dr. Toshiaki Tauchi and Dr. Akiya Miyamoto for their kind suggestions and useful discussions. I would like to thank all of accelerator physicists and engineers of KEK for providing the stable operation of TRISTAN and achieving high luminosity. I really enjoyed working with them at KEK.

Finally I am grateful to my family and my old friends for not only the life support but also the spiritual support.

Contents

1 Introduction **1**

2 Hadron Production in Hard Photon-Photon Collision **7**

2.1 Hadron Production in e^+e^-Collider 7

2.2 Kinematics of Two-Photon Process 9

2.3 Properties of high energy real photon 10

2.4 Jet production in $\gamma\gamma$ collisions 11

2.5 QCD description of jet production in $\gamma\gamma$ collisions 14

2.6 Dijet production in $\gamma\gamma$ collisions 18

2.7 Jet Shape 22

3 Experimental Apparatus **24**

3.1 TRISTAN Accelerator 24

3.2 TOPAZ detector 26

3.2.1 Time-Projection Chamber (TPC) 31

3.2.2 Barrel Calorimeter (BCL) 36

3.2.3 End-cap Calorimeter (ECL) 37

3.2.4 Forward Calorimeter (FCL) 39

3.3 TOPAZ Trigger System 39

3.3.1 Energy Trigger 41

3.3.2 Track Trigger 43

3.3.3 Software Trigger 48

3.4 TOPAZ Data Acquisition System 48

4 Monte-Carlo Simulation **51**

4.1 Two-Photon Event Generations 51

4.1.1 Parton Generation 53

4.1.2 Hadronization 53

4.2 Detector Simulation 58

4.3 Trigger Simulation 59

5 Event Selection **62**
5.1 Two-Photon Event Selection 62
5.2 Annihilation Event Selection 66
5.3 Jet Selection 68
5.3.1 Jet Finding Algorithm 69
5.3.2 Jet E_T Correction 70
5.3.3 Jet and Dijet Event Selection 78
5.4 Background Estimation 79

6 General Properties of Dijet Event **82**
6.1 x_γ Reconstruction from observables 82
6.2 Differences between direct and resolved processes 84
6.2.1 Transverse Energy of Jet Distribution 84
6.2.2 Transverse Energy Flow Distribution 87
6.2.3 Opening Angle between Dijet 91

7 Jet Profile **94**
7.1 Definition of Jet Width 94
7.2 Correction for Jet Width 100
7.3 Systematic Errors 102
7.3.1 Binning effect 102
7.3.2 E_T dependence 103
7.3.3 Model dependence 105
7.4 Results 105
7.5 Discussions 106

8 Conclusion **112**

A Cross Section Formula for Sub-Processes **114**

B Parton Density Function inside a Photon **117**

C Raw Data Processing **122**
C.1 Data Processing Flow 122
C.2 Event Reconstruction 123
C.2.1 Track Reconstruction 123
C.2.2 Cluster Reconstruction 130

List of Figures

1.1 Four typical two-photon processes. (a) direct process, (b) VDM process, (c) one-resolved process and (d) two-resolved process. . . 4

1.2 Maximum cluster-energy distribution measured with the calorimeters in the polar angular region of $0.895 < |\cos\theta| < 0.9984$ for the sample which has two high P_T jets in the central region ($|\eta^{jet}| < 0.7$). Data (closed circle) are compared with the theoretical prediction based on the direct process only (dot-dashed histogram) and that based on the direct + resolved photon process (solid histogram). The VDM contribution is negligible for this sample. . . . 5

2.1 Electron-positron annihilation process. 8

2.2 Two-photon process. 8

2.3 Kinematical view of Two-photon process. 9

2.4 A schematical view of the cross section of hadron production as a function of the photon-virtuality Q^2. 12

2.5 Different states of quasi-real photon. Apart from bare photon state (direct), real photon can fluctuate into quark-antiquark pair without forming a hadronic bound state (anomalous), or form a vector-meson (VDM). A quasi-free parton in the anomalous as well as the VDM components contributes to the hard interaction and jets in the final state (resolved process). 13

2.6 The feynman diagram for the two-resolved process. 15

2.7 Different parametrizations for the parton distributions in the photon. (a) is u-quark distribution in LO, (b) is u-quark distribution in NLO, (c) is gluon distribution in LO and (d) is gluon distribution in NLO. 17

2.8 Initial state radiation of the gluon off the incoming parton in the hard sub-process. 20

2.9 Definition of primordial k_T. k_T is defined as the transverse momentum of the remnant-jet with respect to the direction of the initial photon. 21

3.1 An overview of The TRISTAN Accelerator. 25
3.2 The integrated luminosity accumulated par day. 27
3.3 A cross-sectional view of TOPAZ detector. 28
3.4 The global coordinate system of the TOPAZ detector. 29
3.5 A schematic view of the Time-Projection Chamber. 33
3.6 A view of TPC sector. 34
3.7 The gating grid of the TPC sector. 35
3.8 Momentum resolution of the TPC as a function of P_T. 36
3.9 A schematic view of the Barrel lead-glass Calorimeter 37
3.10 The energy distribution for Bhabha events observed with the BCL at center of mass energy of 52 GeV. 38
3.11 The energy distribution for Bhabha events observed with the ECL at center of mass energy of 52 GeV. 38
3.12 A schematic view of the Forward Calorimeter. 40
3.13 A shape of a FCL module viewed from the beam axis. 40
3.14 A block diagram of the TOPAZ trigger system. 41
3.15 A block diagram of the TOPAZ energy trigger system. 42
3.16 The principles of the track pre-trigger. 44
3.17 A TPC dE/dX wire configuration. 45
3.18 The principle of TPC ripple trigger. 46
3.19 The principle of TPC vertex finder. 47
3.20 The Z distributions of the track in the triggered event. The both lines are the cosmic ray data. The solid line is with the software trigger, and the dashed line is without that trigger. 49
3.21 A flow chart of TOPAZ online computer system. 50

4.1 The analysis flow for data and Monte-Carlo simulation. 52
4.2 The schematic view of $e^+e^- \rightarrow e^+e^-$+ hadrons. 54
4.3 The trigger efficiencies. The points with the error bars are the cosmic ray data. The solid lines are the trigger efficiencies estimated with the trigger simulations. 61

5.1 Z distribution for the reconstructed event vertex. The singly-hatched area is a signal region and the double hatched areas show the regions used to estimate beam-gas backgrounds. 65
5.2 A typical jet production in two-photon event. Left side is Y-Z view and right side is X-Y view. Detectors are indicated to BCL. Solid lines from beam interaction point are reconstructed tracks. 67
5.3 The distance between the hadron jet and the observed jet in $\eta - \phi$ plane. 72
5.4 Various correlations of jet quantities at hadron level and detector level. (a), (b), (c) and (d) is the number of jet, E_T^{jet}, η^{jet} and ϕ^{jet} correlation, respectively. 73
5.5 $E_{T\,observed}^{jet}$ distribution is fitted by Gaussian function in each $E_{T\,hadron}^{jet}$ sub-region. Notice that below and above 3.0 GeV of $E_{T\,hadron}^{jet}$, the horizontal scale is changed. 74
5.6 The E_T^{jet} correlation in $e^+e^- \rightarrow q\bar{q}$ process ($E_{beam} = 29\ GeV$). . . 75
5.7 $E_{T\,observed}^{jet}$ distribution is fitted by Gaussian function in each $E_{T\,hadron}^{jet}$ sub-region ($e^+e^- \rightarrow qq$ sample). Notice that below and above 26 GeV of $E_{T\,hadron}^{jet}$, the horizontal scale is changed. 76
5.8 The E_T^{jet} correlation between the hadron level and the observed level. The horizontal bars represent the resolution of $E_{T\,observed}^{jet}$. The dotted line corresponds to the case of $E_{T\,hadron}^{jet} = E_{T\,observed}^{jet}$. The solid line is a fit by a linear function. 77

6.1 The correlation of x_γ^- and x_γ^+. Dots are the data. 83
6.2 x_γ^{min} distribution for dijet events. Points with Error bars are data. Histograms are PYTHIA predictions with GRV-LO photon structure function. The hatched histogram is the contribution from direct process, and the dashed histogram is that from resolved process. The solid histogram is the sum of both processes. 85
6.3 E_T^{jet} distributions for the data. The solid curves are fitting results using the formula (6.2). (a) is $x_\gamma^{min} > 0.85$ and (b) is $x_\gamma^{min} < 0.85$. 86
6.4 Two cases for choosing factor k. (a) is for $k = +1$ and (b) is for $k = -1$. 88
6.5 The transverse energy flows with respected to the jet axis as a function of the rapidity difference. The points with the error bars are the data. The histogram is Monte-Carlo prediction from PYTHIA with GRV-LO photon structure function. (a) is $x_\gamma^{min} > 0.85$ and (b) is $x_\gamma^{min} < 0.85$. 89

6.6 The transverse energy flows with respected to the jet axis as a function of the azimuthal angle difference. The points with the error bars are the data. The histogram is Monte-Carlo prediction from PYTHIA with GRV-LO photon structure function. (a) is $x_\gamma^{min} > 0.85$ and (b) is $x_\gamma^{min} < 0.85$. 90

6.7 $\Delta\phi_{jj}$ distributions. (a) is $x_\gamma^{min} > 0.85$ and (b) is $x_\gamma^{min} < 0.85$. The points with the error bars are the data. The histogram at (a) is Monte-Carlo prediction from PYTHIA with GRV-LO photon structure function. In (b), the histograms are several Monte-Carlo predictions ; the solid line is with an initial state radiation and power-law k_T, the dashed line is with an initial state radiation and Gaussian k_T, and the dotted line is without an initial state radiation and Gaussian k_T. All histograms are normalized at rightmost bin. 93

7.1 The transverse energy flows with respect to the jet axis for inclusive jet events in $\gamma\gamma$ collision (central part only). The points with the error bars are the data and the solid lines are the fitting results using the formula (7.1). 96

7.2 The transverse energy flows with respect to the jet axis for dijet events in $\gamma\gamma$ collision (central part only). The points with the error bars are the data and the solid lines are the fitting results using the formula (7.1). 97

7.3 The transverse energy flows with respect to the jet axis for inclusive jet events in annihilation process (central part only). The points with the error bars are the data and the solid lines are the fitting results using the formula (7.1). 98

7.4 The transverse energy flows with respect to the jet axis for dijet events in annihilation process (central part only). The points with the error bars are the data and the solid lines are the fitting results using the formula (7.1). 99

7.5 The jet width of the Monte-Carlo simulation at the hadron level. The solid circles and the solid triangles are from two-photon and the solid squares and the solid inverse triangles are the e^+e^-annihilation. For the dijet events at the highest E_T^{jet} bin, the width of the averaged and only the second jet are plotted with the open triangle and the open square, respectively. The errors are statistical only. . 101

7.6 The jet width of the Monte-Carlo simulation at the observed level. The solid circles and the solid triangles are from two-photon and the solid squares and the solid inverse triangles are the e^+e^-annihilation. For the dijet events at the highest E_T^{jet} bin, the width of the averaged and only the second jet are plotted with the open triangle (hidden behind the solid square) and the open square, respectively. The errors are statistical only. 101

7.7 The binning effect. The triangles and the circles are the inclusive jet sample and the dijet sample, respectively. The vertical dashed line indicates factor = 1.0. The horizontal dashed line indicates no deviation from the jet width with factor = 1.0 103

7.8 The observed E_T^{jet} distribution for the e^+e^-annihilation events. . . 104

7.9 The distribution of the jet width as a function of E_T^{jet}. The solid circles and the solid triangles are from two-photon data, and the solid squares and the solid inverse triangles are e^+e^-annihilation data. The open circles, open square and open triangle are H1, UA1 ($\sqrt{s}$ = 540 GeV) and UA1 ($\sqrt{s}$ = 630 GeV), respectively. The errors include statistical and systematic errors added in quadrature. 107

7.10 The distribution of the jet width as a function of $x_T \equiv 2E_T^{jet}/\sqrt{s}$, where $\sqrt{s}$ represents the center-of-mass energy of initial collisions. The solid circles and the solid triangles are from two-photon data, and the solid squares and the solid inverse triangles are the e^+e^-annihilation data at $\sqrt{s_{e^+e^-}} = 58\ GeV$. The open circles are H1 data at $\sqrt{s_{ep}} =$ 297 GeV. The open square and open triangle are UA1 data at $\sqrt{s}$ = 540 GeV and $\sqrt{s}$ = 630 GeV, respectively. The errors include statistical and systematic errors added in quadrature. 108

7.11 Comparison of TOPAZ data with the PYTHIA predictions. The solid circles and the solid triangles are from two-photon data, and the solid squares and the solid inverse triangles are the e^+e^-annihilation data. The solid line with open circles is a PYTHIA prediction with the parton shower. The dashed line with open triangles is the same prediction without the parton shower. 109

7.12 Comparison of TOPAZ data with the PHOJET predictions. The solid circles and the solid triangles are from two-photon data, and the solid squares and the solid inclusive triangles are the e^+e^-annihilation data. The solid line with open circles is PHOJET predictions included the soft components. The dashed line with the open triangles is the same predictions without the soft components (*i.e.* the hard process only). The error bars of open symbols are statistical only. 111

B.1 Generic Feynman diagram for deep-inelastic $e\gamma$ scattering: A probing photon with large virtuality $P^2 \equiv -q^2$ scatters off the (quasi-) real target photon (with virtuality $p^2 \simeq 0$) to produce a hadronic final state. 117

B.2 Measurements of the photon structure function F_2^γ/α. The data(full symbol) are drawn as a function of the parton momentum fraction x_γ(ref.[69]). 119

B.3 Feynman diagrams that contribute to $\gamma^*\gamma$ scattering. (a) a lowest order (QPM) contribution, (b) and (c) are examples of perturbative QCD corrections in the flavor non-singlet and singlet sector, respectively, and (d) non-perturbative contributions described by the VDM. All these contributions are formally summed in (e). . . 120

C.1 A flow chart of TOPAZ offline analysis system. 124

C.2 TPC sector coordinate. 125

C.3 The flow chart of TPC track reconstruction. 126

C.4 The helix parametrization of the charged track by TPC. 128

List of Tables

3.1 A summary of TOPAZ sub-detectors. 30
3.2 A summary of TOPAZ new sub-detectors. 31

4.1 The relations between the sub-processes and the classes. q' also represent an antiquark. 57
4.2 The conditions for PYTHIA. 57
4.3 The conditions for PHOJET. 58
4.4 The charged track trigger conditions for used data. The first errors of Integrated Luminosity indicate the statistical errors, and the second errors are systematic errors. The data at $\sqrt{s}$ = 57.6-59.95 GeV were for energy scan. The center of mass energy had changed in order of 59.7 GeV, 58.2 GeV, 59.2 GeV, 58.45 GeV, 58,7 GeV, 58.95 GeV, 59.95 GeV and 57.6 GeV. 60

5.1 The numbers of survived events at each selection cut. 66
5.2 The number of jets in $\gamma\gamma$ collision at each selection cut. 78
5.3 The number of dijet event in $\gamma\gamma$ collision at each selection cut. . . 79
5.4 The number of jets in e^+e^-annihilation event at each selection cut. 79
5.5 The number of dijet events in e^+e^-annihilation event at each selection cut. 79
5.6 The background contribution to inclusive jet event (%). $E_T^{jet} \geq 2$ GeV and pseudo-rapidity condition is $|\eta^{jet}| \leq 1.0$. 80
5.7 The background contribution to inclusive jet event (%). $E_T^{jet} \geq 2$ GeV and pseudo-rapidity condition is $|\eta^{jet}| \leq 0.7$. 80
5.8 The background contribution to dijet event (%). $E_T^{jet1} \geq 3$ GeV, $E_T^{jet2} \geq 2$ GeV and pseudo-rapidity condition is $|\eta^{jet1}| \leq 1.0$ and $|\eta^{jet2}| \leq 1.0$. 81
5.9 The background contribution to dijet event (%). The conditions of E_T^{jet} are same as the Table. 5.8. Pseudo-rapidity condition is $|\eta^{jet1}| \leq 0.7$ and $|\eta^{jet2}| \leq 0.7$. 81

6.1 The acceptance and purity for each sample. (%). 84

7.1 The number of jet and the number of dijet event detected in a each E_T^{jet} region. 98
7.2 The correction factors for inclusive jet sample. The errors are statistical only. 102
7.3 The correction factors for dijet sample. The errors are statistical only. 102
7.4 The jet widths measured for three different E_T^{jet} regions. 105
7.5 The corrected jet width. The first errors are statistical and the second ones are systematic. 105

C.1 The parameters in the helix function. 129

Chapter 1

Introduction

Overview

The purpose of the high energy (or particle) physics is to study the ultimate constituents of matter and the nature of the interactions between them. The experimental research of high energy physics was started in 1950s in that time particle accelerators were built in the first time. Since then, the energy of accelerators have been increased gradually and several kind of particles like pions, electrons, protons or neutrinos were used as beam particles. The analyses of the scattering reactions in the accelerators have led to a vast amount of discoveries and results.

A recent typical high energy experiment uses collider type accelerators where two beam particles with opposite direction collide each other such as the electron-positron (e^+e^-) collider, electron-proton (ep) collider and proton-anti-proton ($p\bar{p}$) colliders. A typical energy achieved in these colliders are from several 10 GeV to almost 1000 GeV.

In the hadron production in these high energy collisions, the final hadronic state shows clear jet-like structure, where jet means a collimated particle flow originating from the interaction point. These phenomena are clear evidences that elementary particles such as quarks and gluons inside the hadron play an important role in the reaction. In fact it is known that the production cross sections in these processes are well described in terms of the known dynamics such as electroweek interaction and quantum chromodynamics (QCD). In particular, QCD plays an essential role in the hadron collider experiments and the final hadronic states in e^+e^- collider.

Comparing the reactions of e^+e^-, ep and $p\bar{p}$, the mechanism of the high energy reactions which include real (or almost real) photons, such as $\gamma\gamma$ and γp collisions,

has been relatively less understood until quite recently. This is caused by the fact that the high energy photon beams were not available until recently. So far the radiative photons from electron beams can only be used since the photon itself can not be accelerated. The other reason is related to the nature of the real photon itself. The photon is well known as the gauge particle which mediates the electromagnetic interactions. However, at high energies $E_\gamma \geq O(1)\ GeV$, the photon can fluctuate into a quark-anti-quark pair and behaves like a hadron. Then the photon takes part in the strong interaction processes. These processes are described by QCD.

In addition, there are another sources of the complication in the photon. In the low energy reactions which involve real photons, it is known that the phenomenological model called the vector-meson dominance model (VDM), where the photon is assumed to behave like vector mesons such as ρ, ω and ϕ, describes the behavior of the photon relatively well. These low energy phenomena, however, are out of the scope of the perturbative QCD predictions. In the treatment of the photon structure function, the results of the VDM are incorporated in the part of some kinds of parametrization as the input distribution.

In 1987, the electron-positron collider TRISTAN at High Energy Laboratory in Tsukuba (KEK), started its operation. In this collider, the interaction of the almost real photons ($\gamma\gamma$) could be studied in many aspects and some of these results were reported for the first time. The relatively large photon-photon center-of-mass energies allow for quantitative study of the QCD aspects of the $\gamma\gamma$ reactions and the partons coming from the photons.

Photon-Photon Collisions

The dual nature of the photon leads to rich phenomena in real $\gamma\gamma$ collisions. Examples of diagrams contributing to the hadron production in real $\gamma\gamma$ collisions in e^+e^-experiments are shown in Figs. 1.1. Historically, only first two diagrams ; (a) the direct photon process ; and (b) the vector-meson dominance model (VDM) process [5], have been taken into account for the experimental analysis. In the direct process, photons couple to quarks directly and produce quark anti-quark pairs at large angles having high transverse momentum (P_T). The quarks are then hadronized into ordinary hadrons such as π, K, $\cdots$ mesons. If the momentum is large enough, jet-like structure might be observed in the final state. On the other hand, in the VDM process, the photon is treated as a vector-meson (ρ, ω, ϕ, $\cdots$) which has the same quantum number as that of the photon. The final hadronic state in this process has relatively low P_T.

Recently, the existence of another important classes of the diagrams which contribute to $\gamma\gamma$ collisions, as shown in Fig. 1.1 (c) and (d), were proposed [4], [6]. Following the notation in reference [13], we call them "resolved" photon processes since one or both of photons are "resolved" into their hadronic constituents, *i.e.* quark and gluon. If only one photon is resolved into its partonic components, and interacts with the other photon as shown in Fig. 1.1 (c), the process is called "one-resolved" process. On the other hand, the process where both photons are resolved into their partonic constituents is called "two-resolved" process; an example is shown in Fig.1.1 (d). The prediction of cross sections for the resolved photon processes can be given by a perturbative-QCD. The basic formula of the resolved photon process is very similar to that used in the high P_T jet production in hadron-hadron (pp, $p\bar{p}$) collisions. In these hadron-hadron collisions, if P_T of the final-state jets are large enough, partons inside the hadron can be treated as quasi-free particles, because of the asymptotic free nature of the strong force. The jet cross section is given as a convolution of the parton distribution in the hadron (*i.e.* the structure function of the hadron) and the cross section of the parton-parton scattering. Similarly, it is possible to define the parton distribution inside the photon. This parton distribution in the photon is an important parameter to describe the hadron production in many reactions which involve real photons.

Predicted cross sections for the one-resolved and two-resolved processes are the same order as that for the direct process at the TRISTAN energy region, and increase rapidly with increasing of the beam energy. Thus the understanding of these reactions is important for the future high energy e^+e^- colliders. In addition to the magnitude of the cross section, another distinct feature of the resolved photon process is the existence of the remnant-jets which is originating from remaining constituents in the photon. These remnant components might be produced predominantly along the beam direction.

In the previous experiments carried out at the PEP and the PETRA e^+e^- colliders [7][8][9], the data of the hadron production in $\gamma\gamma$ collisions were compared only with the direct and VDM contributions. Although the reason was not well understood in that time, a significant excess of the data over the direct and VDM predictions was already observed. The existence of the resolved photon processes was first confirmed by the AMY group at TRISTAN [10]. They showed the data on multi-hadron production in $\gamma\gamma$ collisions which could be reproduced by the prediction based on the resolved photon process. However, this early experiment of the multi-hadron production in $\gamma\gamma$ collisions was not possible to compare to theoretical predictions directly. The production of actual reconstructed jets (using

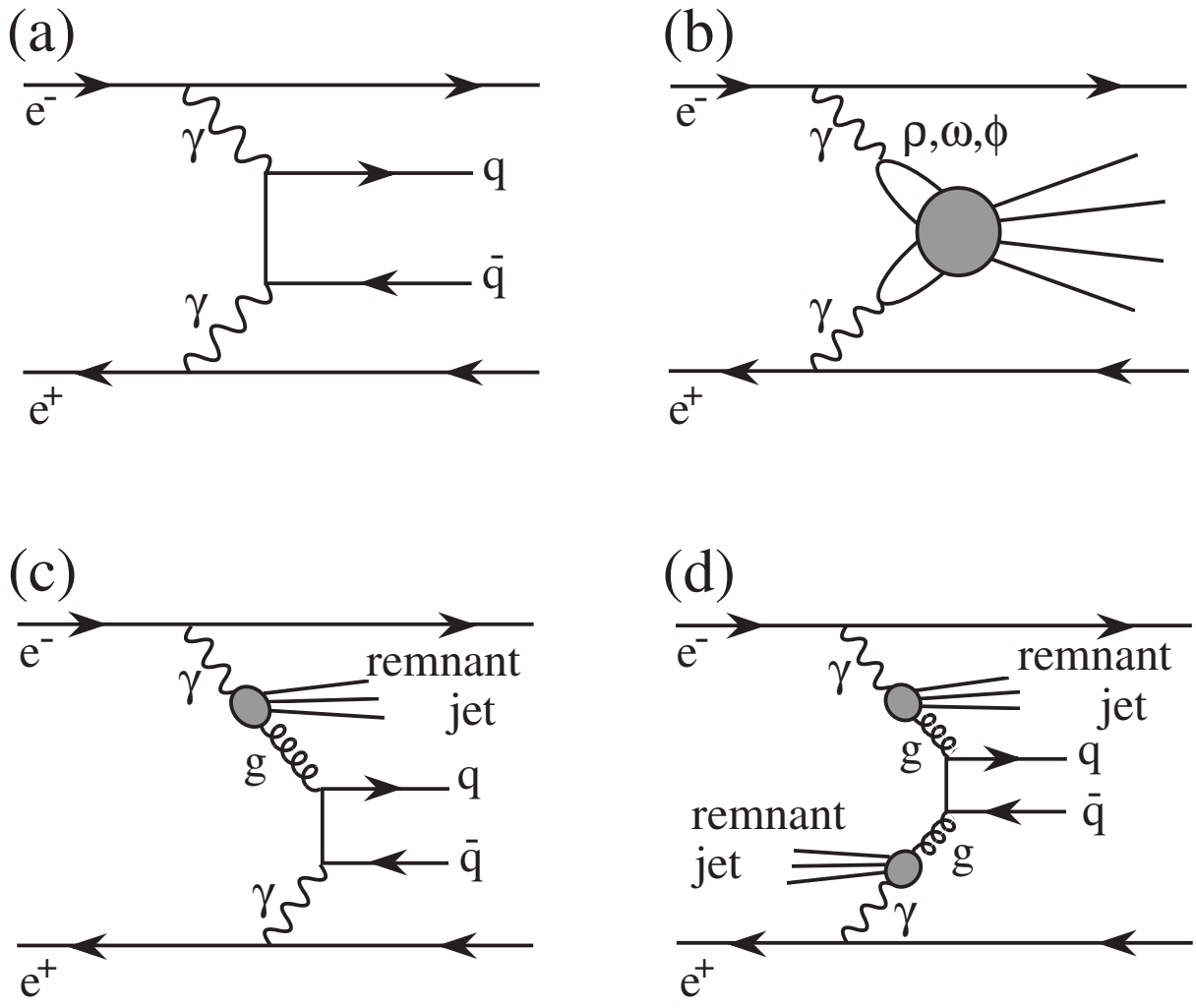

Figure 1.1: Four typical two-photon processes. (a) direct process, (b) VDM process, (c) one-resolved process and (d) two-resolved process.

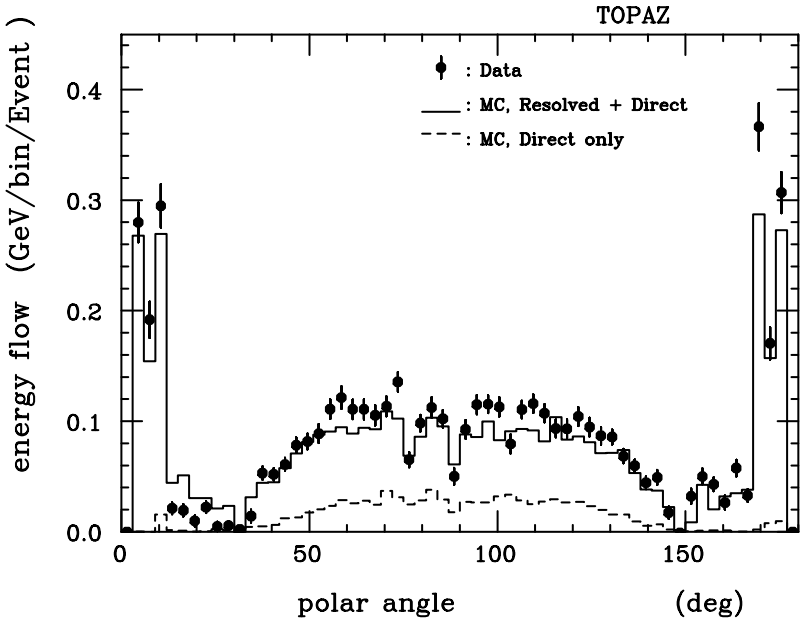

Figure 1.2: Maximum cluster-energy distribution measured with the calorimeters in the polar angular region of $0.895 < |\cos\theta| < 0.9984$ for the sample which has two high P_T jets in the central region ($|\eta^{jet}| < 0.7$). Data (closed circle) are compared with the theoretical prediction based on the direct process only (dot-dashed histogram) and that based on the direct + resolved photon process (solid histogram). The VDM contribution is negligible for this sample.

a cone algorithm) has been studied recently, first by the TOPAZ group [38] and then by the AMY group [11]. The TOPAZ group also reported an evidence for the associated remnant-jet activity in the small-angle detectors. Fig. 1.2 shows the distribution of the particle energy flow for the sample which has two high P_T jets in the central region. In this figure, large activities are clearly observed in the small angle region ($0.972 < |\cos\theta| < 0.9984$). The evidence for the resolved photon processes and its remnant-jets were also observed in γp collisions at HERA [12].

In this thesis, we study the high energy aspects of the $\gamma\gamma$ collisions using the data taken from the TOPAZ detector at TRISTAN e^+e^- collider. In particular, we concentrate on the study of the following two aspects : (1) the general properties of the dijet events, and (2) the jet-profile in $\gamma\gamma$ collisions. The results are compared

with QCD predictions and the results from other experiments. In particular, in the analysis of the jet-profile, the jet widths are compared with those from various other reactions such as the jets in e^+e^-, γp as well as $p\bar{p}$ collisions and their similarity as well as difference have been studied.

The thesis is organized as follows. We review the general formalism of the two-photon process and the properties of the jet in Chapter 2. In Chapter 3, we describe the TRISTAN accelerator and the TOPAZ detector. The trigger system and the data aquation system are also referred here. We explain the Monte Carlo simulations in Chapter 4. In Chapter 5, dijet event selection criteria used in this analysis are described. In Chapter 6, properties of dijet event and in Chapter 7, the shape of jet in $\gamma\gamma$ collisions are studied in detail. Finally, we summarize this analysis in Chapter 8.

Chapter 2

Hadron Production in Hard Photon-Photon Collision

This chapter gives theoretical backgrounds relevant to this analysis. We describe, (i) the kinematics in photon-photon collisions in e^+e^-collider, (ii) theoretical expectations of properties of the real photon and the motivations of the study of high energy $\gamma\gamma$ collisions, (iii) a basic formalism of the jet production in $\gamma\gamma$ collisions and (iv) observables in a dijet event. Finally we introduce the concept of the primordial k_T in the photon as well as the jet-shape variables, which have been studied in detail in this thesis.

2.1 Hadron Production in e^+e^-Collider

In e^+e^-collider, there are two different processes which contribute to the hadron production.

$$e^+e^- \rightarrow \text{hadrons} \tag{2.1}$$

$$e^+e^- \rightarrow e^+e^- + \text{hadrons} \tag{2.2}$$

In the first process, electron and positron annihilate into single virtual time-like photon, which subsequently materializes into hadrons as shown in Fig.2.1. The cross section of the quark pair ($q\bar{q}$) production is given by

$$\sigma(e^+e^- \rightarrow q\bar{q}) = \frac{4\pi\alpha_{em}^2}{3s} N_c e_f^2 = \frac{87\text{nb}}{s} N_c e_f^2 \tag{2.3}$$

where α_{em} ($\equiv e^2/4\pi \sim 1/137$). s is a square of center of mass energy, e_f is the charge of the flavor in the unit of e, N_c is the color factor ($N_c = 3$).

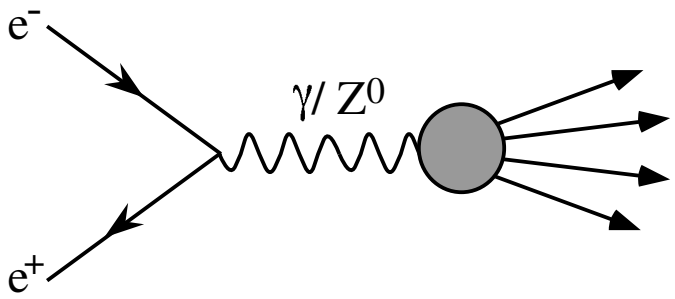

Figure 2.1: Electron-positron annihilation process.

The second one is the hadron production in two-photon process, where both electron and positron radiate space-like photons and both photons interact each other as shown in Fig.2.2. Although the cross section for two-photon processes is down by two orders of α_{em} compared to the annihilation process, the radiation of a photon leads to a characteristic double bremsstrahlung factor of $ln(s/m_e^2)$, which at sufficiently high energies can more than compensate. Here, m_e is the electron mass*. The two-photon process thus become increasingly important at higher energy colliders.

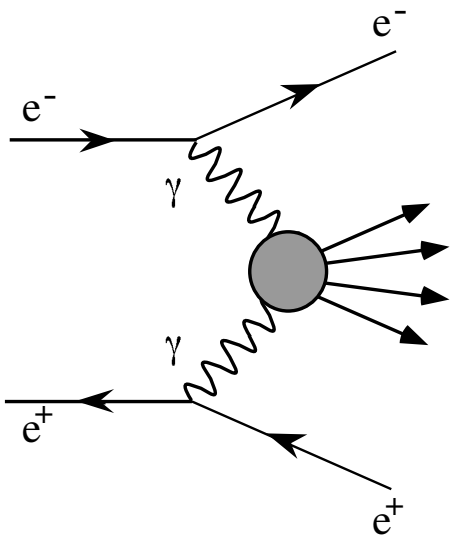

Figure 2.2: Two-photon process.

*In fact, at TRISTAN this factor becomes $ln(s/m_e^2) = ln(50^2/0.0005^2) = 23$

2.2 Kinematics of Two-Photon Process

Kinematics of two-photon process in e^+e^-collider are given in Fig.2.3. In this figure, θ_i $(i = 1, 2)$ are the scattering angles of outgoing $e^{\pm}$, respectively. In the space-like photon, Q_i^2 are defined as $Q_i^2 = -q_i^2$;

$$\begin{aligned} Q_i^2 &\equiv -q_i^2 = -(p_i - p_i')^2 \\ &= -2m_e^2 + 2E_iE_i' - 2P_iP_i'\cos(\theta_i) \end{aligned}$$

where p_i and p_i' denote the four-momentum of outgoing electron (or positron) and incoming electron (positron), respectively†. $q_i = p_i - p_i'$ denotes the four-momentum transfer between outgoing and incoming electrons. The invariant mass of the $\gamma\gamma$-system W is given by,

$$W^2 \equiv (q_1 + q_2)^2.$$

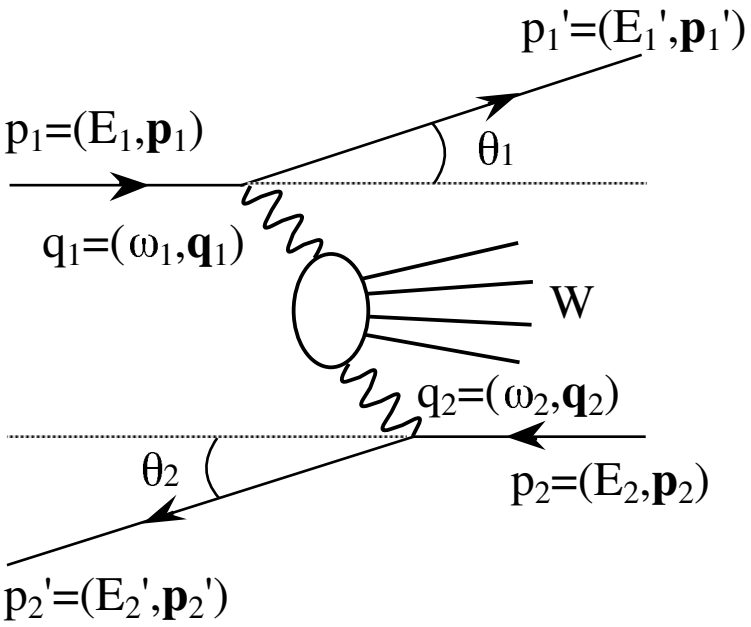

Figure 2.3: Kinematical view of Two-photon process.

The Q^2 represent the virtuality of the photon and can become very small value.

†Hereafter we will not distinguish electron and positron

For example, the minimum Q^2 is given by taking $\theta = 0$ in Eq.(2.4) as

$$Q^2_{min} = \frac{m_e^2 z_\gamma}{1 - z_\gamma}, \tag{2.4}$$

where $z_\gamma = E_\gamma / E_{beam}$ is the energy fraction of the photon radiated from beam electron. At TRISTAN, Q^2_{min} has a value about $\sim 10^{-7}\ GeV^2$.

It is often called that the photon is almost (quasi-) real when its virtuality is $Q^2 \sim 0$, while the photon is virtual when $Q^2 \gg 0$[‡]. Since the probability that electron emits a photon is proportional $1/Q^2$, the cross section in two-photon processes are dominated by the collision of two photons which have very small virtuality, *i.e.* by the (quasi-) real $\gamma\gamma$ collisions.

In this thesis, we will study the jet and dijet production in $\gamma\gamma$ collisions at e^+e^-collider.

$$e^+e^- \to (e^+ + e^-) + jet + (jet) + X. \tag{2.5}$$

In order to ensure that the reaction occurs in the (quasi-) real $\gamma\gamma$ collisions, we limited the maximum scattering angle of both electron and positron to be less than 3.2°, by imposing the "anti-tag" condition in the event selection. With this anti-tag condition, the photon virtuality runs from 10^{-7} to 3 GeV^2. The mean value of the Q^2 is approximately $< Q_i^2 > \sim 10^{-4}\ GeV^2$. In the latter section, the process of Eq.(2.5) will be written simply as

$$\gamma\gamma \to jet + (jet) + X, \tag{2.6}$$

in order to emphasize that we are studying the hard (quasi-) real $\gamma\gamma$ collisions.

In the jet analysis described later, we will require the transverse energy of the jet should be greater than 2∼3 GeV. This condition is equivalent that we are studying the center of mass energies of $\gamma\gamma$ in the range $5 < W < 35\ GeV/c^2$, which is expected to be large enough for the application of perturbative-QCD.

2.3 Properties of high energy real photon

The photon is the well known particle which mediate the electro-magnetic forces. The interaction of high energy photons with the leptons is very well described by the electro-weak theory. If the virtuality of the photon Q^2 is large, the interaction with hadrons (or quarks) is also relatively well known. For example, for time-like photon ($Q^2 = q^2 = s$), the behavior is well studied in the hadron production in

[‡]In more precisely, smallness of the Q^2 is judged by comparing to the value of QCD Λ_{QCD} parameters, where Λ_{QCD} has the value about 0.2∼0.3 GeV^2.

e^+e^-annihilation processes. As is given in Eq.(2.3), the cross section basically decreases as $1/Q^2$ as the photon virtuality $Q^2 = s$ increases,

$$\sigma_{time-like\ photon} \propto \frac{1}{Q^2}, \tag{2.7}$$

except for the resonance region of ρ, ω, ϕ, J/Ψ and Υ (Fig.2.4).

On the other hand, for the space-like region, the process correspond to the deep-inelastic ep collisions, where the behavior of the photon is also well-known and is used as a probe to study the structure of the proton (nucleon).

The cross section of deep-inelastic scattering can be written as

$$\frac{d\sigma_{space-like\ photon}}{dxdQ^2} = \frac{4\pi\alpha_{em}^2}{xQ^4}((1-y)F_2) \tag{2.8}$$

$$\propto \frac{1}{Q^4}, \tag{2.9}$$

and decreases as $1/Q^4$ as the virtuality of photon increases (see Appendix B).

On the other hand, interaction of the (quasi-) real photon with hadron (or real photon) is the most unknown area of high energy collisions to date and has developed an interesting field of QCD. It is noted that the $Q^2 = 0$ point (*i.e.* real photon) is a singular point of the above cross section formula of time-like as well as space-like photon.

Historically, in the first generation of photon-nucleon scattering (γN) experiments as well as photon-photon scattering ($\gamma\gamma$) experiment, the vector meson dominance model (VDM) has been introduced as a very good approximation in the quantitative description of the experimental data. In this model, the photon has a well-defined probability of fluctuating into vector mesons.

In the current view of the QCD theory, the (quasi-) real photon state is expected to fluctuate into $q\bar{q}$ state (Fig.2.5). Because of this nature of the (quasi-) real photon, the photon can interact in various ways as described in the following subsection.

2.4 Jet production in $\gamma\gamma$ collisions

In both high energy $\gamma\gamma$ and γp collisions, the QCD predicts the process where the photon couples directly with quarks, leading to hard parton scattering and jets in the final states (direct photon). A second QCD predictions is that a quasi-free partons in the $q\bar{q}$ bound state contribute to the hard collisions and jets in the final state (resolved photon).

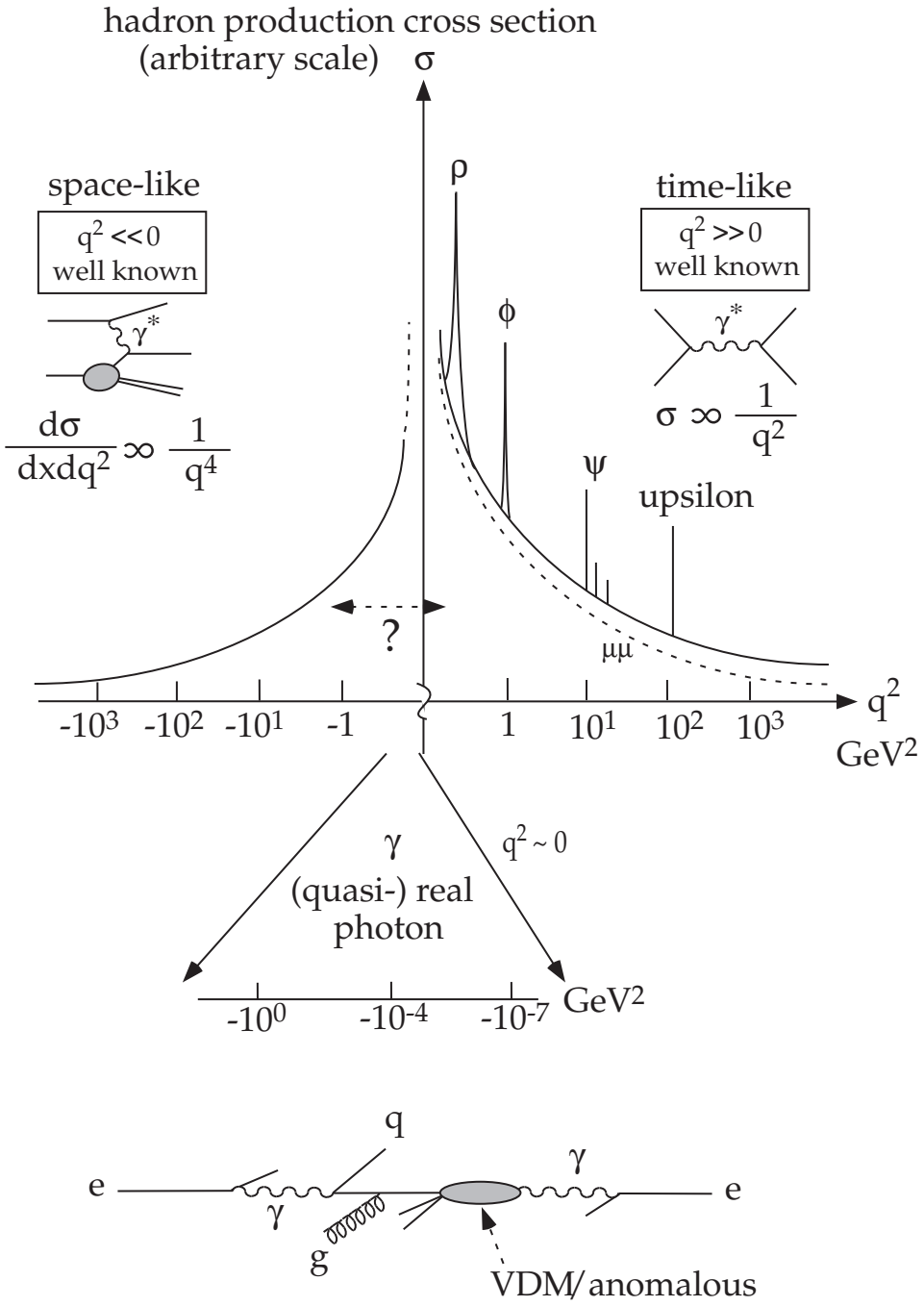

Figure 2.4: A schematical view of the cross section of hadron production as a function of the photon-virtuality Q^2.

In $\gamma\gamma$ collisions these two type of the interactions (direct and resolved), result three different classes. We call them as a direct, one-resolved and two-resolved processes. In the direct process, both photons couple to quarks directly producing high transverse momentum jet in the final state (Fig1.1 (a)). In the one-resolved process, one photon couples to the quark directly and interact with the partonic component of other photon (Fig.1.1 (c)). In the two-resolved process, both photon is resolved and two parton interact (Fig.1.1 (d)). In the resolved photon processes, one expect the production of the remnant-jet in the direction of the resolved photons. Since the photon is radiated to the almost same direction of the beam, the remnant-jet is expected in the very low angle region. The existence of the remnant-jet is the most distinct difference between direct and resolved processes.

As shown in Fig.2.5, some theorists expect that the resolved photon consists of two components which are called as "anomalous" and "VDM" components. In the anomalous component, real photon fluctuate into $q\bar{q}$ pair without forming a hadronic bound state. While in the VDM component, $q\bar{q}$ makes a bound state like usual hadrons and forms a vector-meson [26]. In this scheme, a quasi-free parton in the VDM component as well as the anomalous component can also contribute to the hard interaction. Experimentally, the difference between two components can be seen from the transverse momentum distribution of the remnant-jet with respect to the beam axis (more details are described in section 2.6).

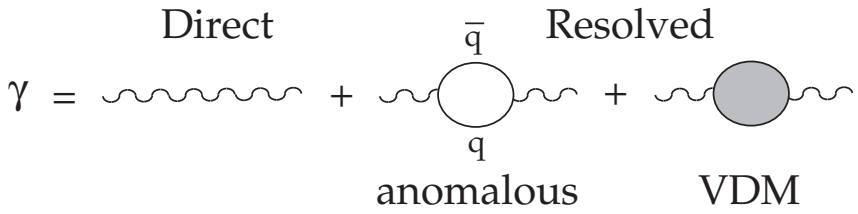

Figure 2.5: Different states of quasi-real photon. Apart from bare photon state (direct), real photon can fluctuate into quark-antiquark pair without forming a hadronic bound state (anomalous), or form a vector-meson (VDM). A quasi-free parton in the anomalous as well as the VDM components contributes to the hard interaction and jets in the final state (resolved process).

2.5 QCD description of jet production in $\gamma\gamma$ collisions

The general expression of the cross section for hard $\gamma\gamma$ interactions in e^+e^- collider is given as follows [13] :

$$\frac{d\sigma(e^+e^- \to e^+e^-X)}{dP_T} = \int f_{\gamma/e^-}(x_1)dx_1 f_{\gamma/e^+}(x_2)dx_2 \; q^\gamma(x_3,\mu^2)dx_3 q^\gamma(x_4,\mu^2)dx_4 \cdot \frac{d\hat{\sigma}(\hat{s},\hat{t},\hat{u})}{dP_T}, \quad (2.10)$$

where $f_{\gamma/e^\pm}$ are the photon flux factors which represent the number of photons radiated from electron, q^γ are the parton (quark and gluon) distribution functions inside the photon and $\frac{d\hat{\sigma}}{dP_T}$ is the differential cross section for the hard sub-processes. The P_T is the transverse momentum (or energy) of the scattered partons, x_1 and x_2 are the photon energies scaled by the beam energy (E_{beam}) and the x_3 and x_4 are the parton energies scaled by the original photon energy. $\hat{s} = x_1x_2x_3x_4s$ is the squared invariant energy of the sub-processes with ($\sqrt{s} = 2E_{beam}$). Finally μ^2 is a typical energy scale in the hard scattering. The transverse momentum $\mu = P_T^2$ or $\frac{1}{4}P_T^2$ are used in the actual calculation of the cross section.

The given form of Eq.(2.10) is valid only for two-resolved process. For the direct process, both q^γ have to be replaced by delta functions $\delta(1-x_i)$ ($i = 3$ and 4). For the one-resolved process, either $q^\gamma(x_3,Q^2)$ or $q^\gamma(x_4,Q^2)$ is replaced by $\delta(1-x_i)$.

There are one sub-process, $\gamma\gamma \to q\bar{q}$, in the direct process and two sub-processes, $\gamma q \to gq$, and $\gamma g \to q\bar{q}$, in one-resolved process. In the two-resolved process there are nine sub-processes as is listed below. (1) $q_i + q_i \to q_i + q_i$, (2) $q_i + q_j \to q_i + q_j$, (3) $q_i + \bar{q}_i \to q_i + \bar{q}_i$, (4) $q_i + \bar{q}_i \to q_j + \bar{q}_j$, (5) $q_i + \bar{q}_j \to q_i + \bar{q}_j$, (6) $q_i + \bar{q}_i \to g + g$, (7) $q_i + g \to q_i + g$, (8) $g + g \to q_i + \bar{q}_i$ and (9) $g + g \to g + g$. Here suffixes i and j indicate quark flavors.

The cross section formula in each sub-process are summarized in Appendix A.

Photon flux

The above expression Eq.(2.10) is obtained by applying the equivalent real-photon approximation to nearly on-shell virtual photons emitted by the beam electrons [14]. In the equivalent real-photon approximation, the photon flux factor can be written as [15],

$$f_{\gamma/e}(x_\gamma) = \frac{\alpha_{em}}{2\pi x_\gamma}\left(1+(1-x_\gamma)^2\right) ln\frac{P^2_{max}}{P^2_{min}} - \frac{\alpha_{em}}{\pi}\frac{1-x_\gamma}{x_\gamma}, \quad (2.11)$$

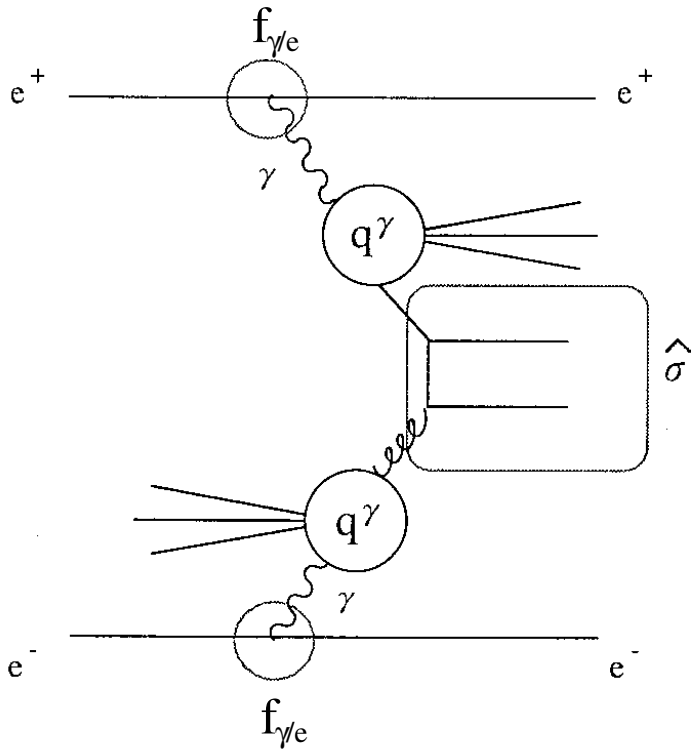

Figure 2.6: The feynman diagram for the two-resolved process.

where

$$P^2_{min} = m_e^2 \frac{x_\gamma^2}{1-x_\gamma}. \tag{2.12}$$

Here, P^2_{min} is the kinematical minimum of the photon virtuality. P^2_{max} is given by

$$P^2_{max} = min(P^2_{max,kin}, Q^2), \tag{2.13}$$

where $P^2_{max,kin} = 2E^2_{beam}(1-x_\gamma)(1-\cos\theta_{max})$ is the maximum photon virtuality determined by the experimental anti-tag condition. Q^2 is a typical scale of the reaction which is determined by the dynamical condition that the cross section is damped for highly virtual photons. P^2_{max} was mainly determined by this anti-tag condition.

Parton distribution function in the photon

The parton distribution functions of the photon can be extracted from the measurement of the photon structure function $F_2^\gamma(x,Q^2)$ in deep inelastic electron-photon scattering, and the QCD evolution functions (Altarelli-Palisi equation). In the leading order, the relation between $F_2^\gamma(x,Q^2)$ and the quark-distribution

function $q^\gamma(x,Q^2)$ is given by

$$F_2^\gamma(x,Q^2) = x\Sigma e_q^2 q^\gamma(x,Q^2). \tag{2.14}$$

For convenient applications, the parametrization of the parton distributions were introduced, which contain the parton momentum distributions at some scale Q_0^2 and their Q^2 evolutions, where F_2^γ is used for a input distribution at some scale $Q^2 = Q_0^2$. For details, see Appendix B.

Today more than a dozen of parametrization sets exist and most of them are available via the PDFLIB [19]. A typical quark distribution and gluon distribution functions are shown in Fig.2.7 [20].

The quark distributions in the photon agree in the range $0.1 < x < 0.9$ to the level of 30 % in various parametrizations. Since the photon structure function (F_2^γ) is not so sensitive to its gluon component, the gluon distribution function is essentially unconstrained by the F_2^γ data. Some details of each parametrization are given below.

GRV parametrization

The Glück-Reya-Vogt (GRV) parametrization [22] is the first NLO fit of $\vec{q}^\gamma$; a LO version is also available. This parametrization is based on the same "dynamical" philosophy as the earlier fits of protonic [23] and pionic [24] densities by the same authors. The idea is to start from a very simple input at a very low Q_0^2 (0.25 $(GeV/c)^2$ in LO, 0.3 $(GeV/c)^2$ in NLO) ; this scale is assumed to be the same for p, π and γ targets. The observed, more complex structure is then generated dynamically by the evolution equations.

$$\vec{q^\gamma_{0,GRV}}(x) = \kappa\frac{4\pi\alpha_{em}}{f_\rho^2}\vec{q^\pi_{0,GRV}}(x). \tag{2.15}$$

This input is motivated from VDM ideas, where f_ρ^2 determines the $\gamma \to \rho$ transition probability ($f_\rho^2/4\pi \simeq 2.2$), and κ has been introduced to describe contributions from heavier vector mesons (ω, ϕ,...). In fact, κ is the only free parameter in the ansatz ; it was determined to be $\kappa = 2$ (1.6) in LO (NLO). However, it should be clear that Eq.(2.15) is an "assumption" that has to be tested experimentally ; in particular, it is not obvious that the parton densities in a pion resemble those in a vector meson, or that QCD is applicable at such small input scales. On the possible side, the GRV parametrization ensures a smooth onset of the charm density, using an x-dependent threshold. Moreover, care has been taken on spilt the NLO parametrizations for $\vec{q}^\gamma$ into LO and NLO pieces ; only the former should be multiplied with NLO pieces of hard cross sections.

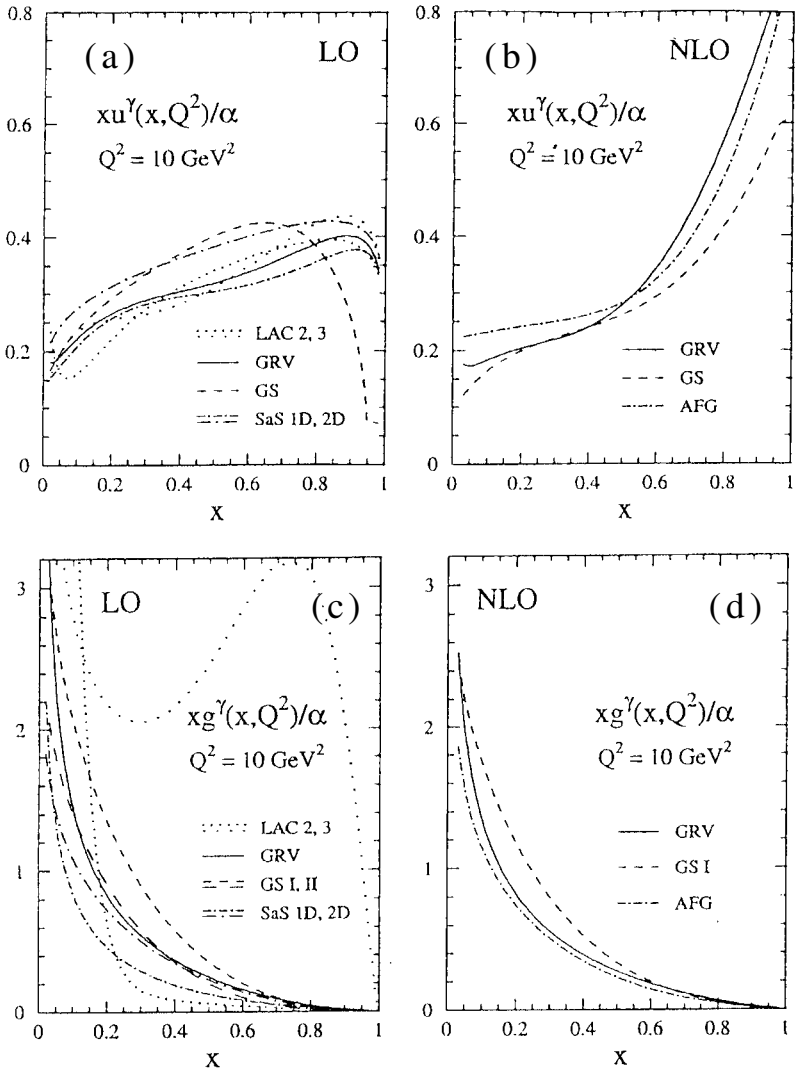

Figure 2.7: Different parametrizations for the parton distributions in the photon. (a) is u-quark distribution in LO, (b) is u-quark distribution in NLO, (c) is gluon distribution in LO and (d) is gluon distribution in NLO.

SaS parametrization

Schuler-Sjöstrand (SaS) parametrizations [25] are based on a similar philosophy as the GRV parametrization, by assuming that at a low $Q_0 \simeq 0.6\ GeV/c$ the perturbative component vanishes (SaS1). However, while the normalization of the non-perturbative contribution is taken from the VDM (including ρ, ω and ϕ contributions with fixed normalization), the shape of the quark and gluon distributions are fitted from data. Although the SaS parametrizations are available in LO only, the authors attempt to estimate the scheme dependence (formally an NLO effect) providing a parametrization with $Q_0 = 2\ GeV/c$; however, in this case the normalization of the fitted "soft" contribution had to be left free, and its shape is much harder than one what expects from hadronic parton densities. Again two sets of parametrizations are available, using different schemes (SaS2D, SaS2M).

2.6 Dijet production in $\gamma\gamma$ collisions

In high energy collisions, the final state consists of a collection of hadrons called a jet.

If both jets in the final states are detected, the kinematics of the hard parton scattering sub-process are determined. Assuming the lowest order two partons $\rightarrow$ two partons ($2 \rightarrow 2$) scattering, convenient observables to describe the final-state partons are their transverse momenta (P_T) and rapidities (η)[†] in the laboratory system. The transformation from the parton center-of-mass system (CM) to the laboratory system (LAB) is given by

$$P_{T_i}^{LAB} = P_{T_i}^{CM}, \tag{2.16}$$

$$\eta_i^{LAB} = \eta_i^{CM} + \eta^{boost}. \tag{2.17}$$

Here the intrinsic transverse momentum of the partons from the photon and the target particle have been neglected. Since the parton configuration in the parton center-of-mass system is back-to-back, their rapidity sum is,

$$\eta_1^{CM} + \eta_2^{CM} = 0. \tag{2.18}$$

Using Eq.(2.17) and Eq.(2.18), the boost of the parton center-of-mass system with respect to the laboratory system can be calculated by the parton rapidities in the laboratory system :

$$\eta^{boost} = \frac{\eta_1^{LAB} + \eta_2^{LAB}}{2} \equiv \bar{\eta}.$$

The rapidity difference is Lorentz invariant under boosts along the beam axis :

$$\eta_1^{LAB} - \eta_2^{LAB} = \eta_1^{CM} - \eta_2^{CM} \equiv \eta^*.$$

The scaling variables $x_{\gamma 1}$, $x_{\gamma 2}$ are defined as the momentum fraction of the parton in the parent photon and are related to η_1^{LAB} , η_2^{LAB} by :

$$x_{\gamma 1} = \frac{x_T}{2}(\eta_1^{LAB} + \eta_2^{LAB}), \tag{2.19}$$

$$x_{\gamma 2} = \frac{x_T}{2}(\eta_1^{LAB} - \eta_2^{LAB}), \tag{2.20}$$

with $x_T = 2p_T^{jet}/\sqrt{s_{e^+e^-}}$. Rewriting Eq.(2.19) and Eq.(2.20) with $\bar{\eta}$ and η^*, we obtain :

$$x_{\gamma 1} = x_T e^{\bar{\eta}} cosh(\frac{\eta^*}{2}) \tag{2.21}$$

$$x_{\gamma 2} = x_T e^{-\bar{\eta}} cosh(\frac{\eta^*}{2}). \tag{2.22}$$

Using the original definition of the (pseudo)-rapidity

$$\eta = \frac{1}{2}\ln\left(\frac{E+p_z}{E-p_z}\right) \tag{2.23}$$

$$\sim -ln(tan\frac{\theta}{2}) \tag{2.24}$$

the $x_{\gamma 1/2}$ can be also written as

$$x_{\gamma 1/2} = \frac{\sum_j^{parton}(E \pm P_Z)_j}{\sum_i^{all}(E \pm P_Z)_i} \quad , \tag{2.25}$$

where the numerator is the sum of two partons (jets) in the final state, while the denominator is the sum of all final state hadrons including the remnant-jets. In the analysis of the dijet events, this last equation is used to reconstruct the parton momentum fraction in the photon (x_γ).

Initial state radiation and Primordial k_T of parton inside a photon

The above argument neglects several important issues which might be affect and observed in the actual experiment. In the lowest order $2 \to 2$ partons scattering,

† When θ is the scattering angle, $P_T = P \cdot sin\theta$, $\eta = -ln(tan\frac{\theta}{2})$.

the final state partons should be back-to-back in azimuthal (r-ϕ) plane. However they may not be exactly back-to-back because of several reasons given below.

(1) The detector resolution and the hadronization effect might smear the original parton direction.

(2) The virtuality of the photon Q^2 is not exactly zero, which provide some transverse momentum to the initial photons.

Apart from these relatively trivial effects, there are additional dynamical reasons which might change the dijet azimuthal distribution from back-to-back.

(3) The initial state radiation of the gluon from the incoming partons in the hard sub-process.

(4) Primordial (intrinsic) transverse momentum (k_T) of the parton within the photon.

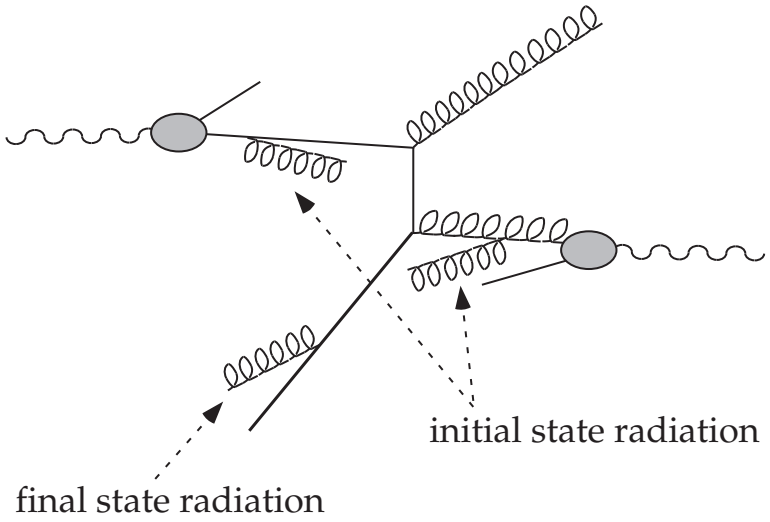

Figure 2.8: Initial state radiation of the gluon off the incoming parton in the hard sub-process.

Fig.2.8 shows the initial state radiation in the hard sub-process. In QCD, the final state radiation as well as this initial state radiation of the gluon are expected and are described by the parton shower program in the event generator programs.

Fig.2.9 gives the definition of the primordial k_T within the photon. Here the k_T is defined as the transverse momentum of the remnant-jet with respect to the original photon direction. As is shown in Fig.2.5, theorists expect there might be two different kinds of $q\bar{q}$ state in the fluctuation from the photon [26] [27] [28]

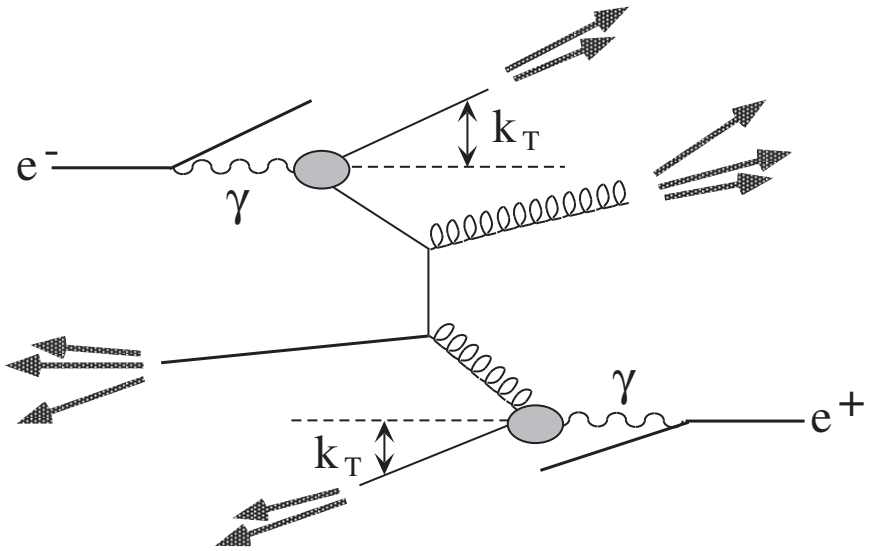

Figure 2.9: Definition of primordial k_T. k_T is defined as the transverse momentum of the remnant-jet with respect to the direction of the initial photon.

[29]. One is the "anomalous" state where $q\bar{q}$ is loosely bounded. The other is the vector meson (hadron) state where $q\bar{q}$ makes a bound state like usual hadrons.

It is expected that these two different components result the different form in the k_T distribution. For anomalous photons the power-law k_T distribution is expected :

$$\frac{dN}{dk_T^2} \propto \frac{1}{k_T^2 + k_0^2}, \tag{2.26}$$

where k_0 is a parameter in the order of a few 100 MeV. On the other hand, when the photon is seen as usual hadrons in the VDM component, the parton inside the hadron (VDM-photon) expected to have a exponential form

$$\frac{dN}{dk_T^2} \propto exp(-\frac{k_T^2}{2\sigma^2}). \tag{2.27}$$

This form is motivated from the Fermi-motion of the parton inside the hadron (photon). The σ parameter is expected about $\Lambda_{QCD} \sim 0.2$~0.3 GeV .

We will test these expectation from the azimuthal angle distribution of the dijet event. The effects of the initial state radiation and the primordial k_T exist only in the resolved photon processes, since there are no initial quark and photon structure in the direct process. If the direct and resolved processes can be separated in event-by-event, one can study these effects independently from other trivial effects of (1) and (2).

2.7 Jet Shape

Recently, there has been a lot of attention to the internal structure of jets in hadron collision both from experiment and theoretical sides [32] [31].

One of the most popular measures of jet structure in hadron collisions is the jet shape; the fraction of the jet's energy within a cone of a given size, centered on the jet direction. The jet shape is a simple measure of how widely jet's energy is spread. The width of the jet-shape (*i.e.* jet-width) is also a convenient measure in the study of the dependence of the jet shape as a function of jet-transverse momentum (or energy) E_T or in the comparison between various kind of high energy collisions including $p\bar{p}$, γp and $\gamma\gamma$. Experimentally, the jet-shape or jet-width can be measured from the transverse energy (E_T) flow with respect to the jet axis.

Theoretically, the jet shape in the high-energy collisions is expected to be mainly determined from the gluon radiations in the final state parton as well as the initial state radiation. At sufficient high energy, where non-perturbative hadronization effects are negligible, the jet shape should be calculable by perturbative QCD. In QCD, the jet-shape is given essentially from the ratio of the energy weighted next-leading-order cross section ($2 \to 3$ sub $-$ process) and the lowest-order parton cross section ($2 \to 2$ sub $-$ process) :

$$f(E_T^{jet}, \eta, R, r) = \frac{\int dE_T E_T \frac{d\sigma_{NLO}^{jet}}{dE_T dr}}{\int_R dr \int dE_T E_T \frac{d\sigma_{LO}^{jet}}{dE_T dr}}, \tag{2.28}$$

where E_T is a transverse energy of the "particle" at the distance (r) from the jet axis. E_T^{jet} is the transverse energy of jet and R is the jet-cone radius (a detailed definition of jet-cone R will be given in section 5.3.1). So far for the jet-shape only leading-order calculation of the jet-shape is available (This is included in general event generator), and complete NLO is not yet available. Therefore the prediction itself is not so accurate.

Below we will give more qualitative discussion about the jet shape. The jet shape (or width) generally depends on the jet-E_T and pseudo-rapidity η and cone-radius r as well as initial beam particles. However, in QCD some universality are expected since it is only determined from the shower evolution of the partons. From the equation Eq.(2.28), one can learn that (1) $f(E_T^{jet}, \eta)$ is proportional to $O(\alpha_s)$ since the numerator is proportional to α_s^3, whereas the denominator is $O(\alpha_s^2)$, (2)$f(E_T^{jet}, \eta)$ is dimensionless. This means the E_T^{jet} dependence should be included in the function f a part of dimensionless variable [33].

From these observation, G. Kramer and S.G. Salesch suggested that the shower shape depend only of the dimensionless variable

$$x_T = \frac{2E_T^{jet}}{\sqrt{s}}. \tag{2.29}$$

Therefore, if the value of x_T is same, the jet shape might be similar for jets produced in high energy $p\bar{p}$, γp and $\gamma\gamma$ collisions, neglecting the small Q^2 dependence in α_s. They recommended for s in Eq.(2.29) to use the beam center-of-mass energy ; *i.e.* $s = s_{p\bar{p}}$ for $p\bar{p}$ collision, $s = s_{ep}$ for γp collision and $s = s_{ee}$ for $\gamma\gamma$ collision. In other word, the jet-width will be different even if jet E_T^{jet} is same in different collider if it's x_T is different. Usually, the jet-shape in $p\bar{p}$ collider, e^+e^-collider as well as γp collisions have been compared at the approximately same E_T^{jet}, and the difference of the quark initiated-jet and gluon initiated-jet are discussed. If the above suggestion is correct, we should compare the jet at the same x_T instead of the same E_T^{jet}.

This is the motivation of the analysis of the jet-width in this thesis. We measured the jet-width in $\gamma\gamma$ collisions in the range of the E_T^{jet} from 2 GeV to 9.5 GeV. In addition we measure the jet-width of e^+e^-annihilation process. Note that this is the first measurement of the jet-width in e^+e^-annihilation event, since the jet-cone algorithm itself has not been used in the analysis of the annihilation events. These results is compared with the ones in γp and $p\bar{p}$ collisions to study the E_T^{jet} (or x_T) dependence of jet-width.

Chapter 3

Experimental Apparatus

The data used in this thesis were collected with the TOPAZ detector at the electron-positron collider, TRISTAN. A brief introduction of the TRISTAN accelerator and the TOPAZ detector is given below. TOPAZ trigger system and data acquisition system are also described.

3.1 TRISTAN Accelerator

Overview

TRISTAN is a large positron-electron colliding beam facility at the National Laboratory for High Energy Physics (KEK) [40]. This accelerator is operated at the center-of-mass energies around 58 GeV. Fig.3.1 illustrates the schematic view of TRISTAN.

TRISTAN consists of three main components : a linear accelerator (LINAC), an accumulation ring (AR) and a main storage ring (MR). The LINAC is 400 m long and accelerates electrons and positrons up to 2.5 GeV. Positrons are produced by bombardment of a tantalum target with a high-current electron beam of 200 MeV from a linear accelerator placed at the upstream end of the main linac, and are then accelerated to 250 MeV by another linear accelerator located downstream of the conversion target prior to transfer to the main linac. Electrons and positrons accelerated in the main linac are injected and accumulated in the AR. The AR in a booster whose circumference in 377 m and stores electrons or positrons from the LINAC to the beam current more than 10 mA. After the accumulation, the electron or positron beam is accelerated up to 8.0 GeV and then injected into the main ring. A typical injection time from the LINAC to the MR is about 30 $minutes$. The MR has a 3018 m circumference and has

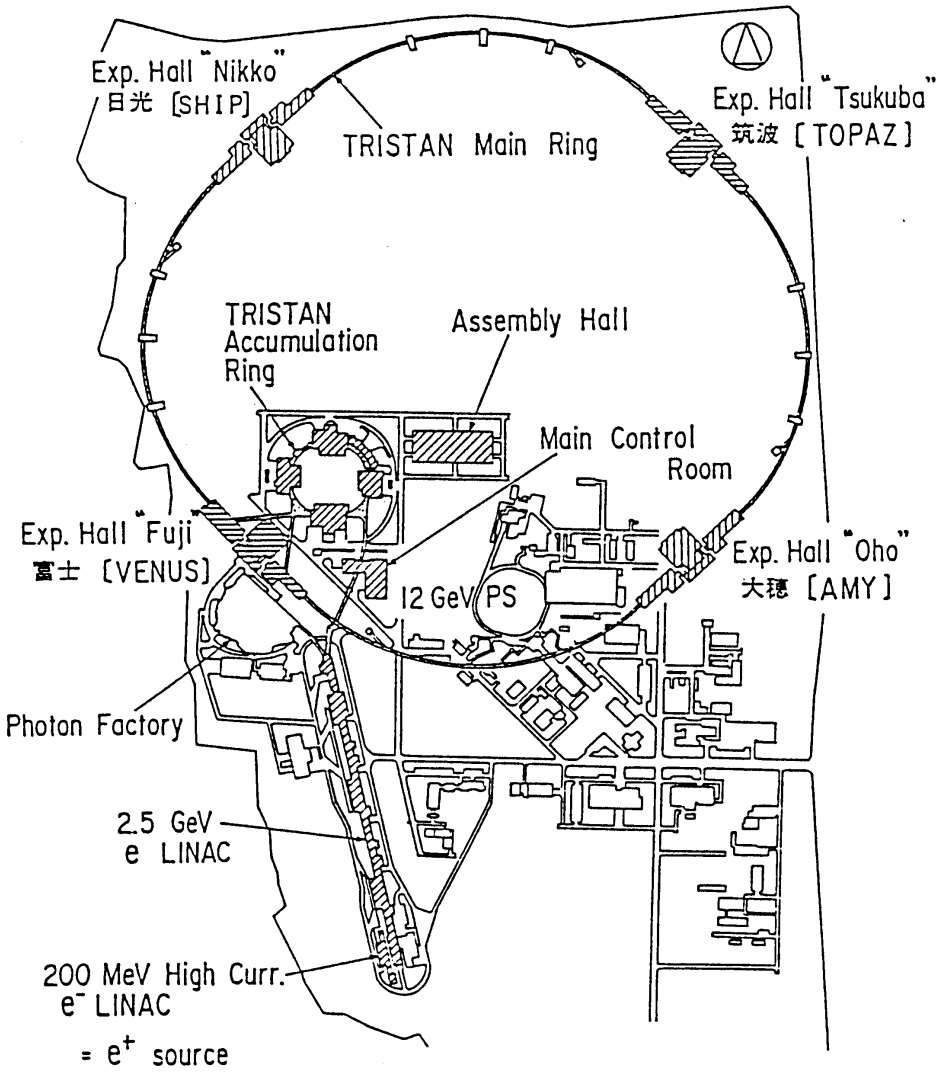

Figure 3.1: An overview of The TRISTAN Accelerator.

four straight sections 193 m long each. Two electron and two positron bunches circulate in opposite directions and collide with each other at the mid-points of the straight sections where the colliding beam detectors, AMY, TOPAZ, SHIP and VENUS, are located. The bunches collide every 5 μsec. A large portion of the straight section is allocated for RF cavities ($f_{RF} = 508.6\ MHz$) which accelerate the beams from the injection energy to the required collision energy and compensate for large energy loss by synchrotron radiation.

Experimental history

The TRISTAN experiment started in 1986 at the center-of-mass energy ($\sqrt{s}$) of 50 GeV, and since then it had been the most important tasks to raise the energy of TRISTAN as high as possible (TRISTAN Phase-I). To achieve this goal, more than thirty cavities were installed st TRISTAN until the summer of 1989. The maximum $\sqrt{s}$ was achieved to be 64 GeV.

In February 1990, TRISTAN Phase-II operation started. The emphasis of the operation was placed on achieving as high luminosity as possible. To increase the luminosity a pair of superconducting quadrupole magnets (DCS's) were installed at each collision point. The center of mass energy of TRISTAN was set at 58 GeV in order to have a sufficient operational margin for RF cavities and to minimize breakdown of cavities leading to beam losses. In consequence of these efforts, a typical integrated luminosity par day amounted about 800 nb^{-1} as shown in Fig.3.2.

The TRISTAN ended its operation in May 1995, and the total integrated luminosity collected with the TOPAZ detector until then has reached more than 300 pb^{-1}.

3.2 TOPAZ detector

The TOPAZ detector is a multi-purpose 4π detector designed to study the charged and neutral particles produced from electron-positron interaction. It was located at the northwest experimental hall, which is named TSUKUBA, of the TRISTAN MR. The cross-sectional view is shown in Fig.3.3.

In spring 1987, the TOPAZ detector was rolled into TSUKUBA experimental hall, and from then, it had been operated quite successfully. The features of the TOPAZ sub-detectors are summarized in Table 3.1.

In autumn 1989, The TOPAZ detector was upgraded to maximize the physics capability for high luminosity data taking (TRISTAN Phase-II operation). As the

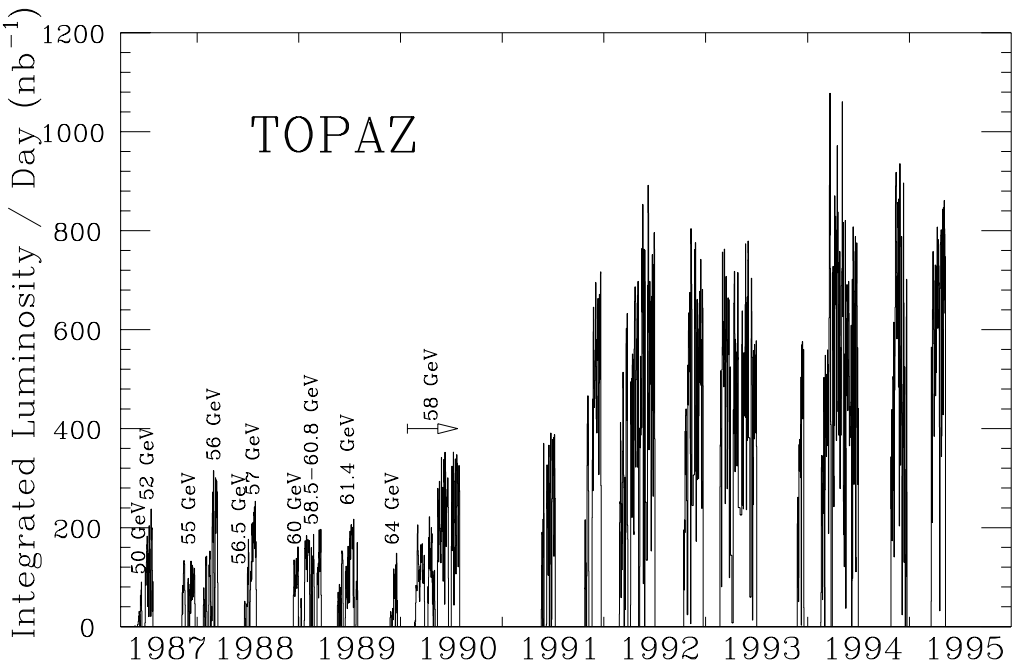

Figure 3.2: The integrated luminosity accumulated par day.

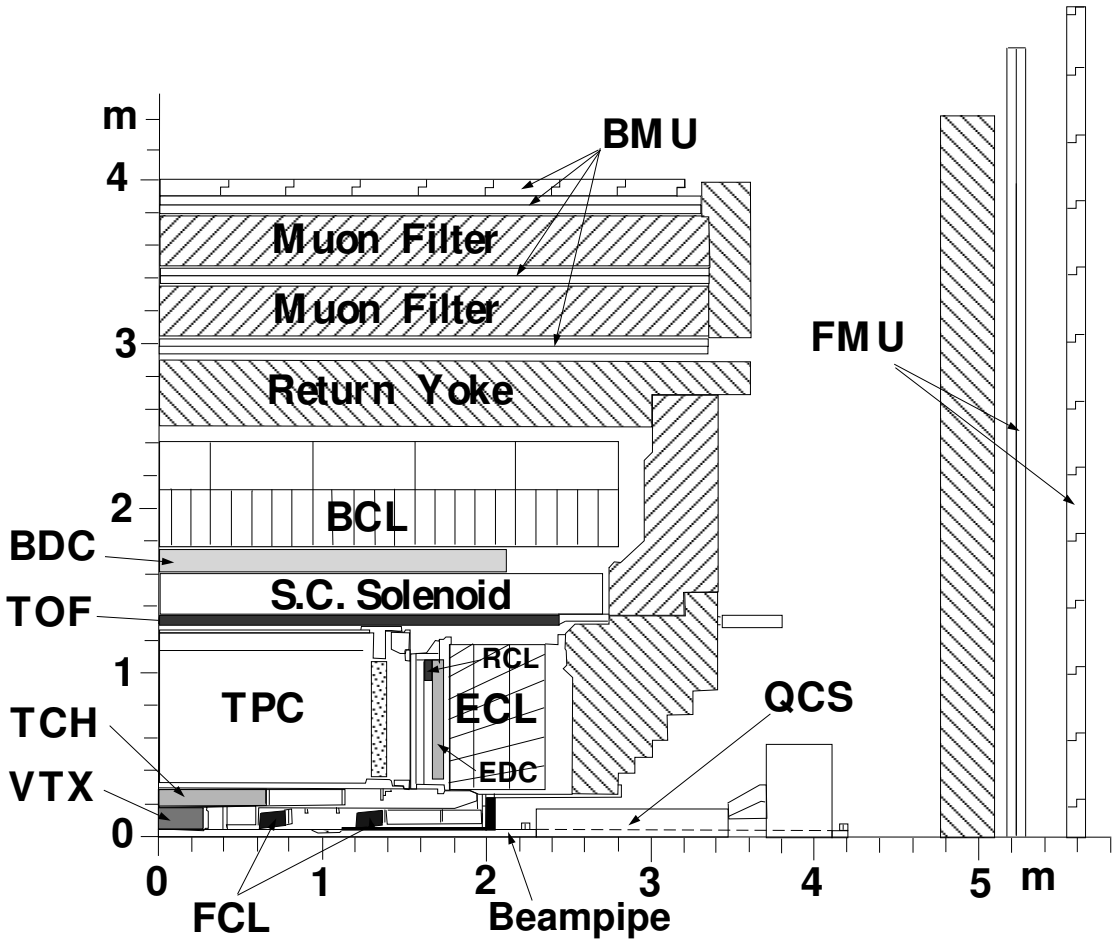

Figure 3.3: A cross-sectional view of TOPAZ detector.

result of these improvements, the TOPAZ detector became a hermetic and had better measurements of luminosity and charged particles. The features of these new sub-detectors are summarized in Table 3.2.

For detecting charged particles, Vertex-Chamber (VTX), Trigger-Chamber (TCH) and Time-Projection Chamber (TPC) were used. These detectors were placed in an axial magnetic field of 1.0 $Tesla$.

The coordinate system for the detector geometry is taken to be right-handed Cartesian as shown in Fig3.4. The X-axis is horizontal and outward from the center of the TRISTAN ring, the Y-axis is vertical and upward, and the Z-axis is parallel to the direction of the electron beam. The origin is the interaction point.

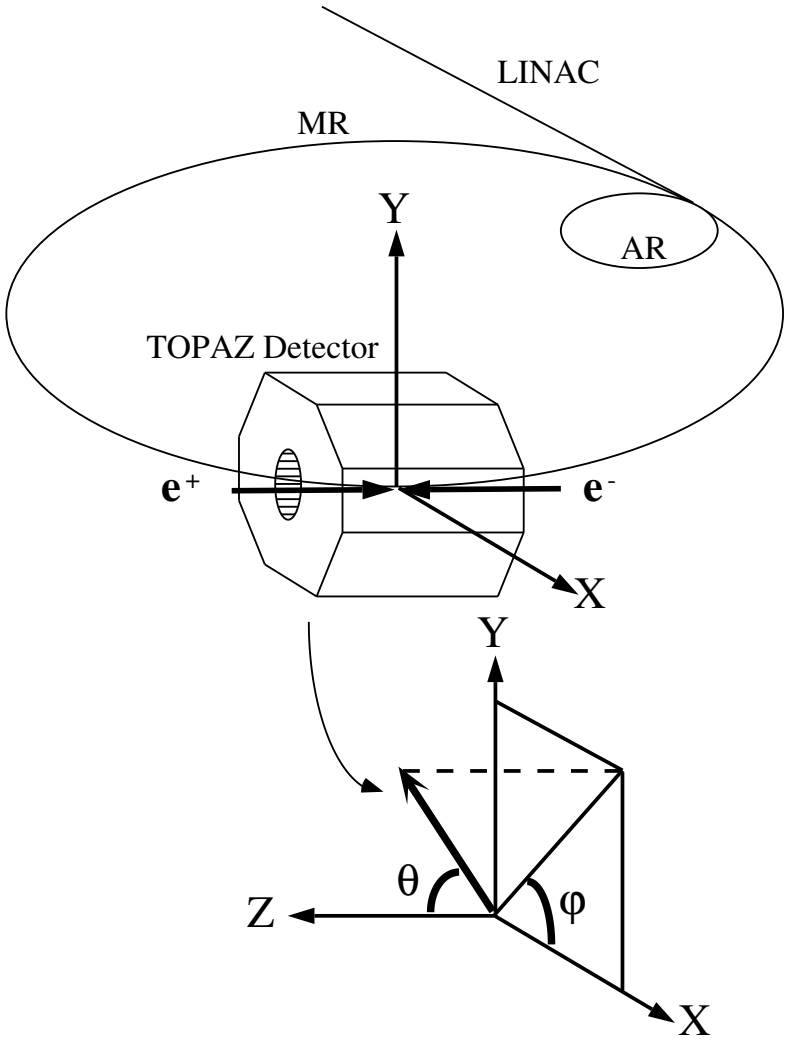

Figure 3.4: The global coordinate system of the TOPAZ detector.

Components	Material and Size	Measured Performance
Beam Pipe	171.5 mm (ϕ) 1.8 mm - thick Al	
VTX	Jet chamber, 16 sectors 25 sense wires/sector CO_2/C_2H_6 (92/8) $3atm$ $66 \leq$ r ≤ 161 mm, L = $60cm$	$\sigma_{r\phi} = 40$ μm $\sigma_{ip} = 75$ μm
TCH	Cylindrical, 8 layers 128 sense wire/layer $Ar/CO_2/CH_4$ (89/10/1) $1atm$ $220 \leq$ r ≤ 279 mm, L = 130 cm	$\sigma_{r\phi} = 250$ μm
TPC	16 sector 10 pad row, 176 wires/sector Ar/CH_4 (90/10) $3.5atm$ $364 \leq$ r ≤ 1090 mm, L = 2.2 m	$\sigma_{r\phi} = 185$ μm $\sigma_z = 335$ μm σ(dE/dX) = 4.6 % $\sigma_{pt}/p_t = \sqrt{(1.5p_t)^2 + 1.6^2}$ %
TOF	64 plastic scinti. (BC412) $\lvert\cos\theta\rvert \leq 0.85$	$\sigma_{TOF} = 210$ ps
Magnet	$2.9m(\phi) \times 5m$(L), $0.7X_0$	B = $1.0Tesla$
BDC	Streamer tube $Ar/CO_2/CH_6$ (50/50) $1atm$ 4 layers($r\phi$)	$\sigma_{r\phi} = 500$ μm $\sigma_z = 5$ μm
BCL	Lead-glass (SF6W), $20X_0$ 4300 $blocks$ $\lvert\cos\theta\rvert \leq 0.848$	$\sigma_E/E = \sqrt{(\frac{8.0}{\sqrt{E}})^2 + (2.5)^2}$ % $\sigma_\theta = 0.38$
BMU	3 layers($r\phi$), 1 layer(z) Ar/CH_4(90/10) $1atm$ $\lvert\cos\theta\rvert \leq 0.75$	$\sigma_{r\phi} = 1$ mm

Table 3.1: A summary of TOPAZ sub-detectors.

Components	Material and Size	Measured Performance
FCL	BGO + Si-strip, $15X_0$ $38 \leq \theta \leq 66\ mrad$ (LUM) $60 \leq \theta \leq 227\ mrad$ (FBC)	$\sigma_E/E = 5.0$ % (for 29 GeV electron)
EDC	Streamer tube 2 layers each in x and y. $Ar/C_2H_6(30/70)\ 1atm$ $0.866 \leq \lvert\cos\theta\rvert \leq 0.966$	
ECL	Pb-PWC Sandwich $18X_0$ thick $Ar/CH_4(95/5)\ 1atm$ $0.848 \leq \lvert\cos\theta\rvert \leq 0.978$	$\sigma_E/E = 6.7$ % (for 26 GeV electron) $\sigma_\theta = 0.7$
RCL	W-Si Sandwich, $7.0X_0$ $0.839 \leq \lvert\cos\theta\rvert \leq 0.860$	$\sigma_E/E = 17$ % (for 29 GeV electron)

Table 3.2: A summary of TOPAZ new sub-detectors.

As shown in the Fig.3.3, the TOPAZ detector is a general purpose magnetic spectrometer using a Time-Projection Chamber (TPC) [44] as the primary tracking element. TPC has eight sectors, each of which has 176 sense wires, in each of its endcaps. Inside TPC there are two additional tracking chambers: a Trigger Chamber (TCH) and a Vertex Chamber (VTX). Sixty-four plastic scintillator Time-of-Flight counters (TOF) surround TPC. There elements are located in a solenoidal magnetic field of 1 $Tesla$. A 4300-element Barrel lead glass Calorimeter (BCL) [43] located outside the superconducting magnet coil, an Endcap Pb-PWC sandwich Calorimeter (ECL) [42], a Forward Si-pad/BGO-crystal Calorimeter (FCL : FBC, LUM) [41], and a Ring Calorimeter (RCL) constitute a electromagnetic calorimeter system, hermetic down to a polar angle of 60 $mrad$. Barrel (BMU) and Forward (FMU) Muon Chambers are the outermost detectors which are used to measure muons penetrating muon filters (Muon Filter).

3.2.1 Time-Projection Chamber (TPC)

The Time-Projection Chamber (TPC) [44] is the central tracking device of the TOPAZ. TPC provides simultaneous measurements of three dimensional position and energy loss (dE/dx) of charged particles to be used for particle identifications.

TPC is also used for the trigger of charged tracks (TPC trigger). The schematic view of TPC is shown in Fig.3.5.

The axial length of the sensitive volume is about 2.0 m in Z-direction and the inner and outer radii are 0.3 and 1.1 m, respectively. TPC consists of 8 multiwire proportional chambers (sector:shown in Fig.3.6) located at each endcap side and a cylindrical pressure vessel.

Each sector has 175 anode sense wires, 175 field wires spacing 2 mm alternatively, and 10 pad rows (512 pads per one sector) on the cathode plane. The sense wires are held at 1970 V and the field wires at 200 V under the normal condition, respectively. The vessel is made from the Glass Fiber Reinforced Plastic (GFRP) and filled with a gas mixture of 90% Ar and 10 % CH_4 at 3.5 atm.

Charged particles passing through the TPC sensitive region ionize gas molecules and liberate electrons along their trajectories. These dissociated electrons drift along the direction of the electric field of 353 V/cm toward the sectors at a typical speed of 5.3 $cm/\mu sec$. This electric field is produced by supplying the negative voltage to the central membrane located in the center of the pressure vessel. These electrons finally produce avalanches around sense wires. The ion clouds produced there induced electric signals on the nearby cathode pads. The signals from wires and pads are amplified and are shaped by analogue electronics. They are then fed into charge coupled device (CCD) digitizers sampling the wave-forms in units of a 100 $nsec$ "bucket" from which the Z-positions and energy-loss (dE/dx) information are extracted. The gains of the wire signals are calibrated by the X-ray (5.9 KeV) from the ^{55}Fe sources.

Since the positive ions moves 10^4 times slower than electrons do, they would build up a positive ion clouds in the TPC sensitive region and would cause a distortion of the electric field (space charge effect). In order to reduce such an effect, the gating-grid plane is placed above the shielding-grid plane (Fig. 3.7). The gating grids are usually closed to prevent positive ions from drifting to the sensitive region and are opened only when the opening signals come from other detectors (i.e., trigger system).

The spatial and momentum resolutions are studied with cosmic rays as well as Bhabha and $e^+e^- \rightarrow \mu^+\mu^-$ events. The spatial resolution was obtained to be σ_{XY} = 185 μm and σ_Z = 335μm. By comparing two measurements in the opposing sectors in cosmic-ray events, the momentum resolution was measured to be

$$\sigma_{P_T}/P_T = \sqrt{(1.5P_T)^2 + 1.6^2}\ \%.$$

The momentum resolution as a function of momentum is shown in Fig.3.8. The dE/dx resolution was studied using minimum-ionizing pions in the beam events.

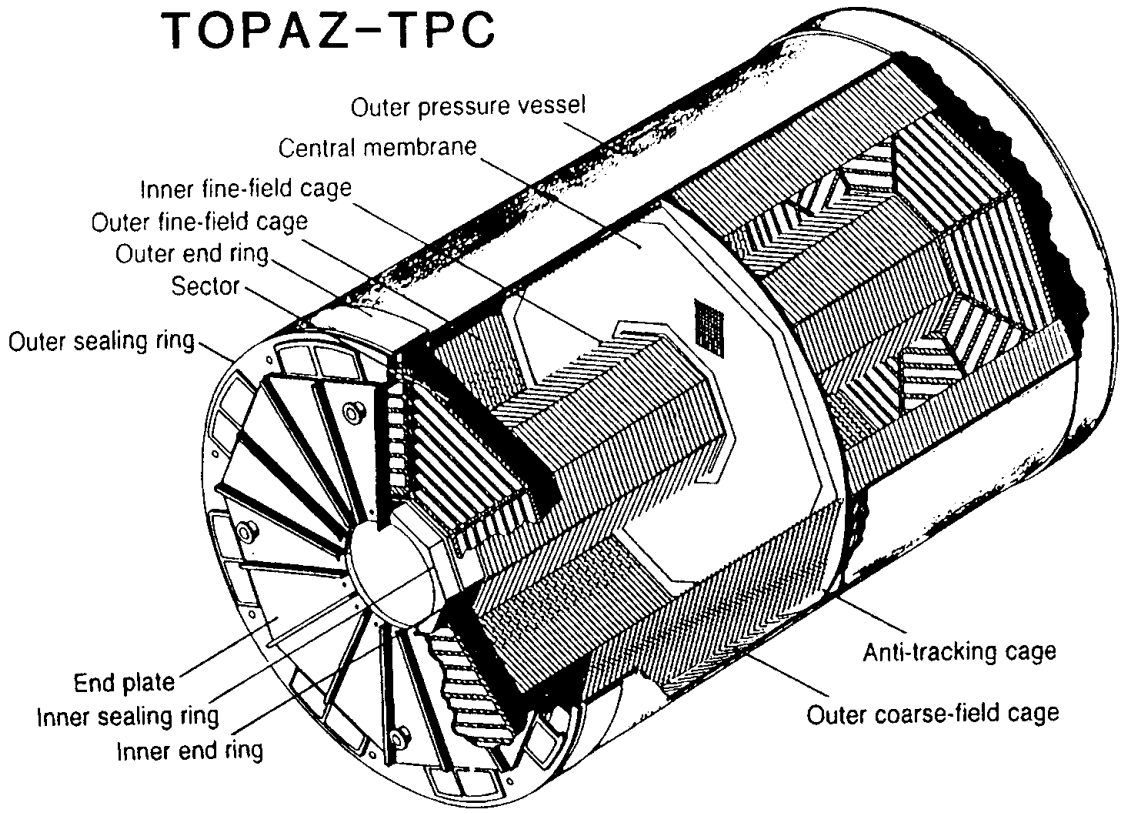

Figure 3.5: A schematic view of the Time-Projection Chamber.

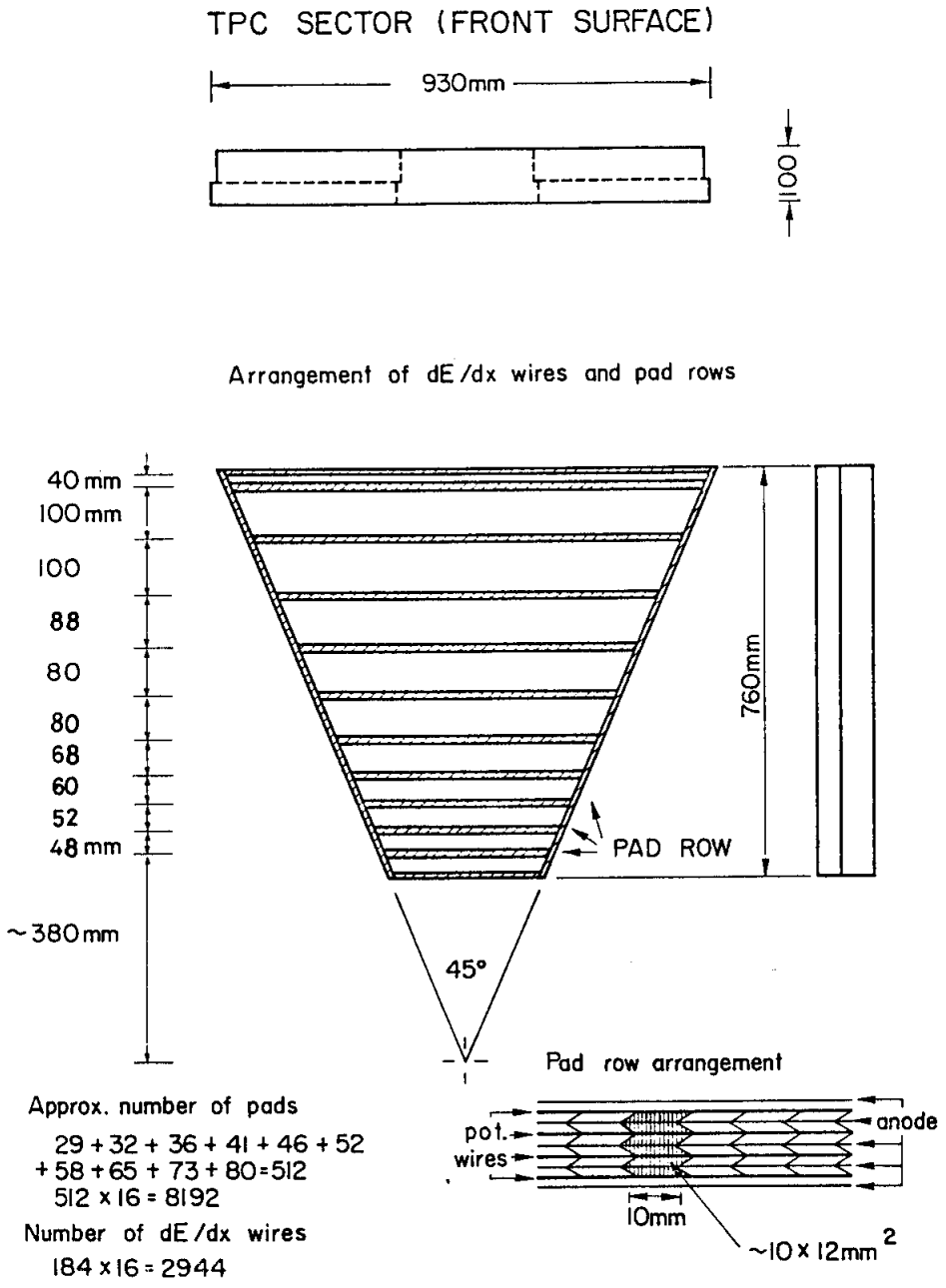

Figure 3.6: A view of TPC sector.

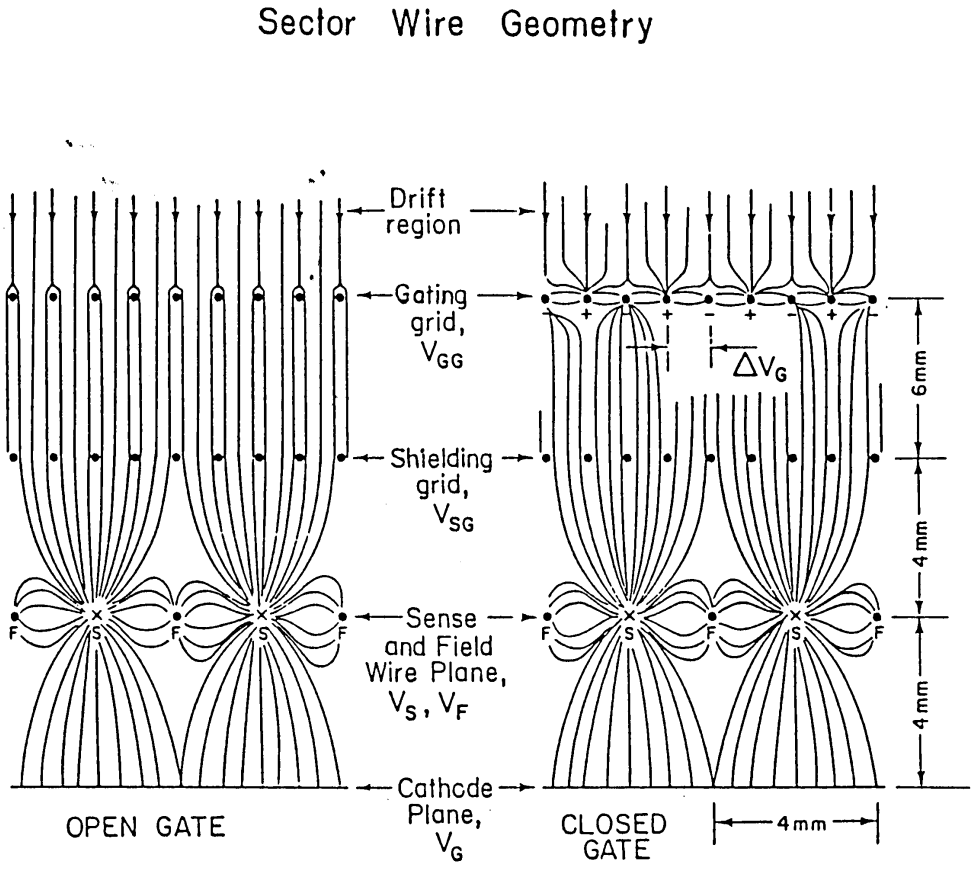

Figure 3.7: The gating grid of the TPC sector.

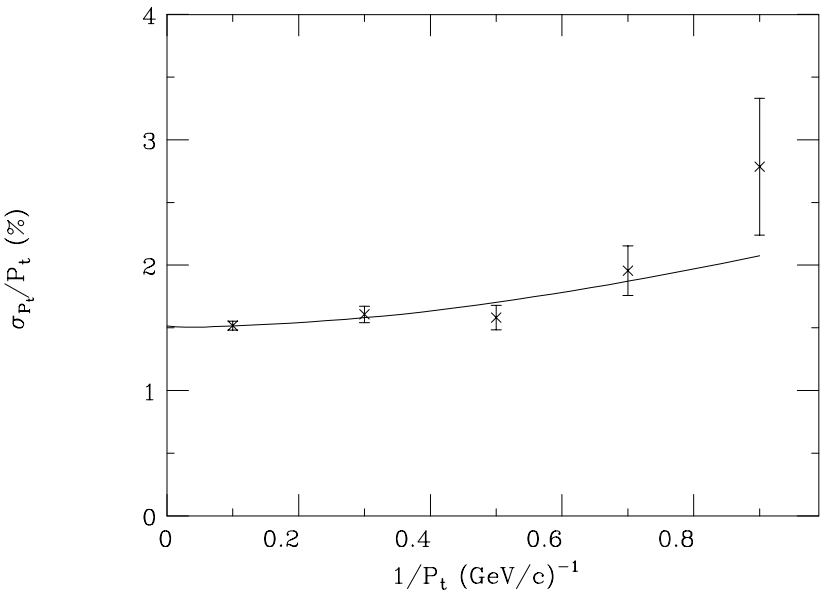

Figure 3.8: Momentum resolution of the TPC as a function of P_T.

The obtained resolution is $\sigma_{dE/dx}$ =4.6 % after all calibrations such as gas density corrections and drift-path length corrections.

3.2.2 Barrel Calorimeter (BCL)

The Barrel Calorimeter (BCL), which comprises 4300 lead-glass Čerenkov counters, has a cylindrical structure covering an angular region of $|\cos\theta| \leq 0.82$. The calorimeter is divided into 72 modules of identical shape, 8 in the ϕ (azimuthal) direction and 9 in the Z-direction as shown in Fig.3.9. Each module consists of a matrix of $12(\phi)\times5(Z)$ lead-glass counters allowing room for the service port (chimney) for the superconducting solenoidal magnet.

Each lead-glass counter is made of SF6W and has 20 radiation lengths (X_0), so that it can absorb more than 95% of the shower energies at TRISTAN's highest energy. The lead-glass blocks are tilted by 1.8° with respect to the radial line in the r-ϕ plane so that no photons coming from the interaction point escape through the counter-to-counter gaps. The Čerenkov light emitted in a lead-glass counter is detected by a photomultiplier after passing through a light guide. The signal from the photomultiplier is sent to a charge sensitive ADC and is also used for a neutral trigger. The system is calibrated by using a Xe flash lamp.

The performance of the BCL was studied by using Bhabha events. Fig. 3.10 shows the energy distribution for Bhabha events at $\sqrt{s} = 52\ GeV$. The energy

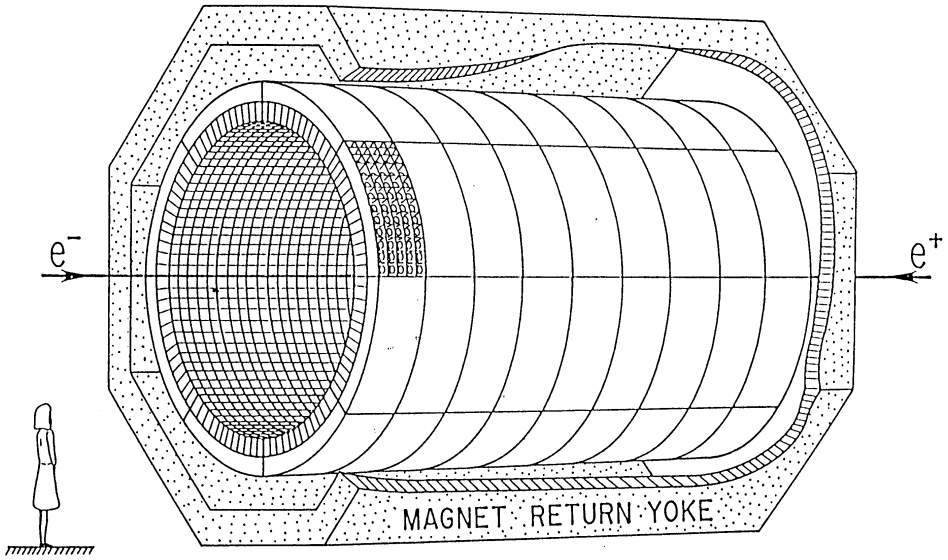

Figure 3.9: A schematic view of the Barrel lead-glass Calorimeter

and spatial resolution were determined to be $\sigma_E/E = \sqrt{(8/\sqrt{E})^2 + 2.5^2}$ % (E in GeV) and σ_θ=0.38°, respectively.

3.2.3 End-cap Calorimeter (ECL)

The end-cap calorimeter (ECL), mounted in each end-cap, is a gas sampling electromagnetic calorimeter covering an angular region of $0.85 \leq |\cos\theta| \leq 0.98$. It consists of proportional wire tubes interleaved with lead absorber, and is operated with the gas mixture of 95% Ar and 5% CH_4. The ECL is segmented into 3 modules along the beam direction; the first module comprises 8 layers with 2 mm lead absorber, the second 12 layers and the third 14 layers with 3 mm absorber, amounting to $18X_0$. One layer is made of 196 high resistive plastic tubes glued on a printed circuit (PC) board. Each of the plastic tubes has a cross section of 10×15 mm^2.

The energy distribution for Bhabha event at $\sqrt{s}$=52 GeV is shown in Fig. 3.11, and the energy resolution was obtained to be σ_E/E = 6.7 %. The polar angle resolution was measured to be $\sigma_\theta = 0.7°$.

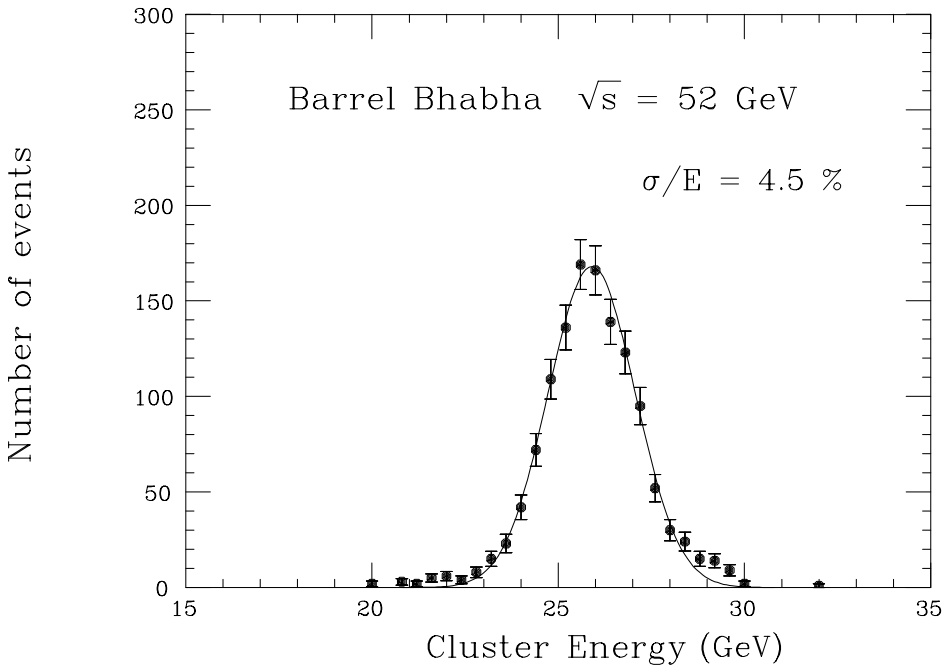

Figure 3.10: The energy distribution for Bhabha events observed with the BCL at center of mass energy of 52 GeV.

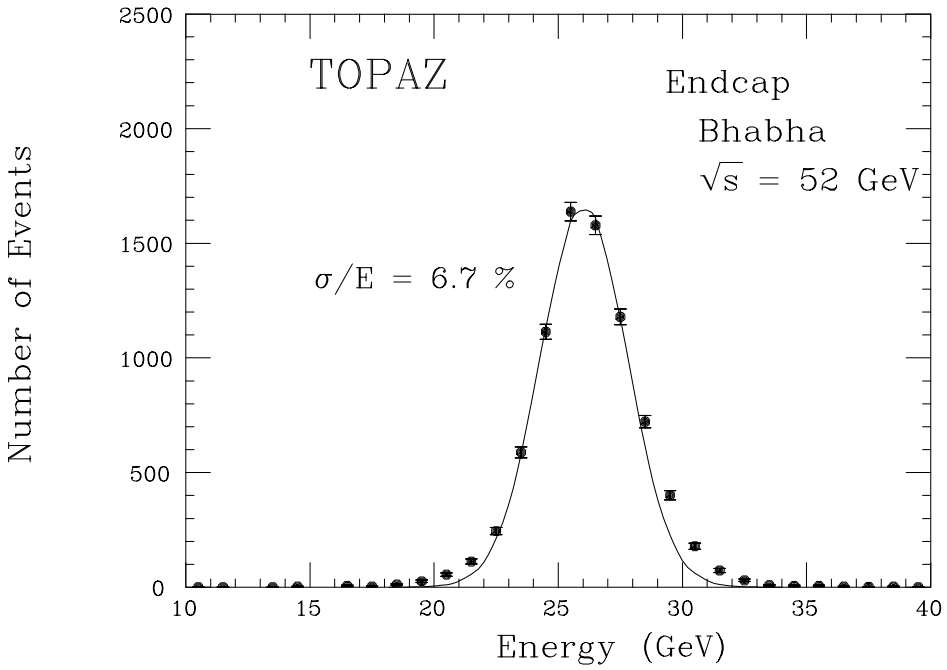

Figure 3.11: The energy distribution for Bhabha events observed with the ECL at center of mass energy of 52 GeV.

3.2.4 Forward Calorimeter (FCL)

The TOPAZ detector was upgraded in order to achieve improved performance for high luminosity e^+e^- experiment. The Forward Calorimeter (FCL) is one of the important components of new detectors which located at a small angular region (which covers polar angles from 3.2° to 13.6°) of the TOPAZ detector. The main purpose of FCL are follows : (1) To make the TOPAZ detector hermetic ; (2) To tag electrons and/or positrons in order to study two-photon processes in detail ; (3) To monitor the real time luminosity, and to measure the integrated luminosity of TOPAZ detector precisely. The old TOPAZ luminosity monitor[45] was replaced with this new FCL in 1989.

The structure of the FCL is schematically shown in Fig. 3.12. It comprises four identical modules, the two modules at $Z = \pm 60$ cm called the Forward-Backward Calorimeter (FBC) and the other two modules at $Z = \pm 12$ cm the Luminosity Monitor (LUM) for convenience. Each module is azimuthally segmented into twelve blocks, as can be seen in Fig. 3.13. Each block comprises a BGO calorimeter for energy measurements, and a silicon strip detector located in front of the BGO calorimeter for position measurements. The BGO calorimeter consists of 5.3 mm thick tungsten absorber ($1.5X_0$), 150 mm thick BGO crystal ($13.5X_0$), and a silicon photodiode readout system.

The energy resolution of the BGO calorimeter is less than 5 % from 1 to 30 GeV which was estimated by test beam measurements carried out at the IT4 test beam line of the AR and Bhabha electrons. The silicon strip detector is designed so as to keep the polar angular resolution within 5%.

3.3 TOPAZ Trigger System

The purpose of the trigger system is to pick our interesting events from huge backgrounds effectively. The time taken for the acquisition of one accepted events is about 30 $msec$. This period is called "dead time" because other trigger signals cannot be accepted. In order to keep the dead time less than 10 %, the total trigger rate should be less than 3 Hz.

The TOPAZ trigger system consists of the hardware part and the software part. Fig.3.14 shows two hardware trigger parts ; the energy trigger and the track trigger. The former is designed mainly for Bhabha events and hadronic events, while the latter is for events with small energy deposits in the calorimeters such as $e^+e^- \rightarrow \mu^+\mu^-$ events. In the software trigger, a more accurate decision is made by a multi-processor system using the timing information from TPC.

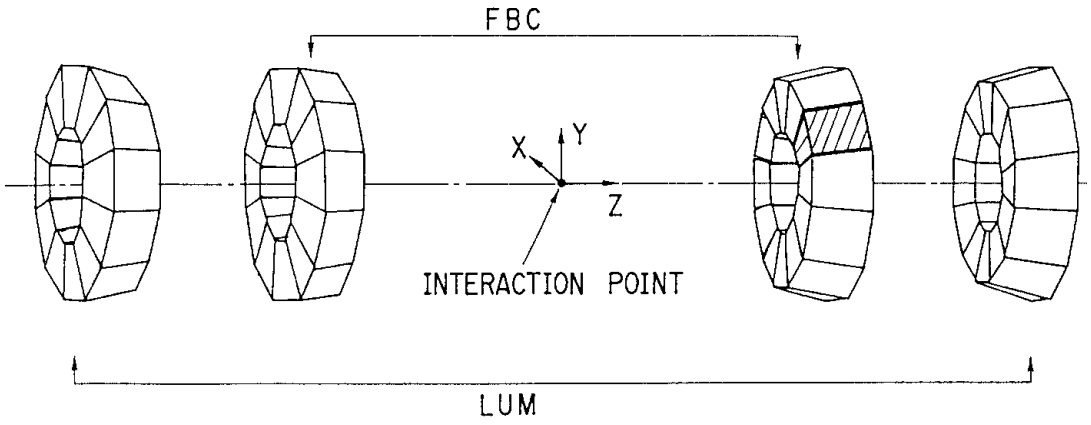

Figure 3.12: A schematic view of the Forward Calorimeter.

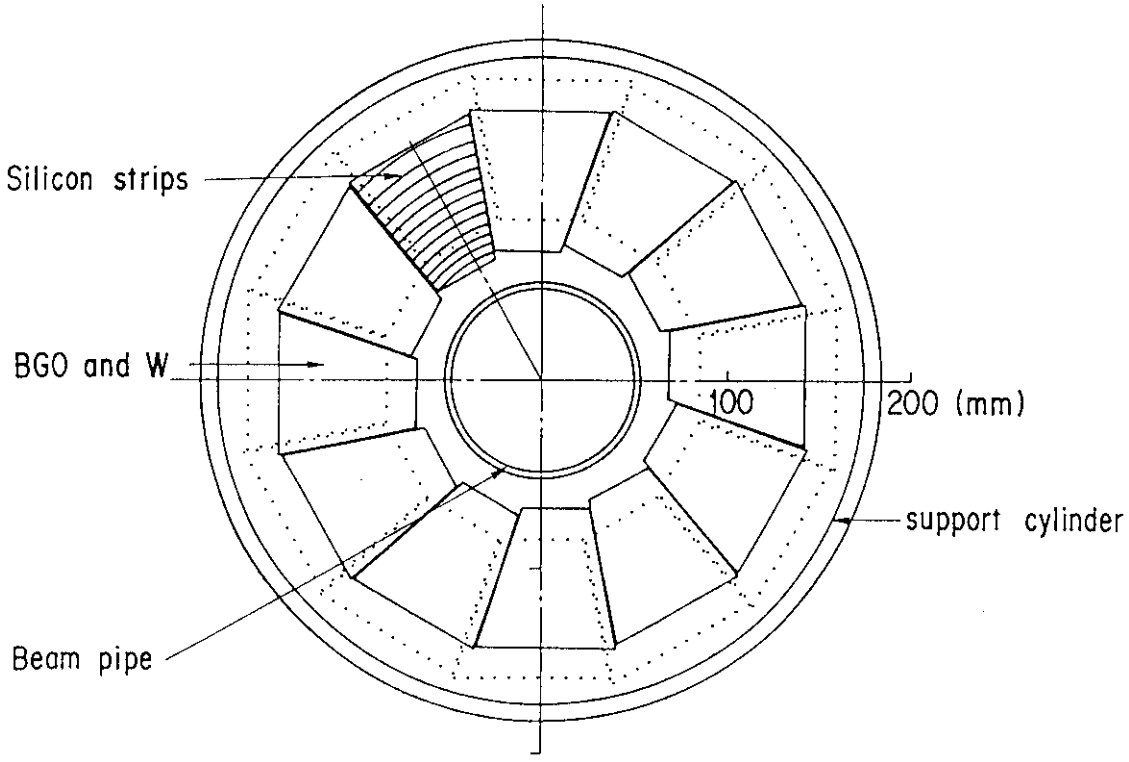

Figure 3.13: A shape of a FCL module viewed from the beam axis.

When the trigger system received a Beam Crossing Over (BC/O) signal, it opens the trigger gate. If the energy trigger or the pre-trigger is issued, the TPC gating grid is open. The energy trigger is treated as a trigger without any other condition (forced pre-trigger). In the case of pre-trigger without energy trigger, the TPC trigger decision starts. If the TPC trigger accepts the event, the software trigger starts and decides whether it is a real trigger or not.

In the next sections, we describe the energy trigger, the charged trigger and the software trigger.

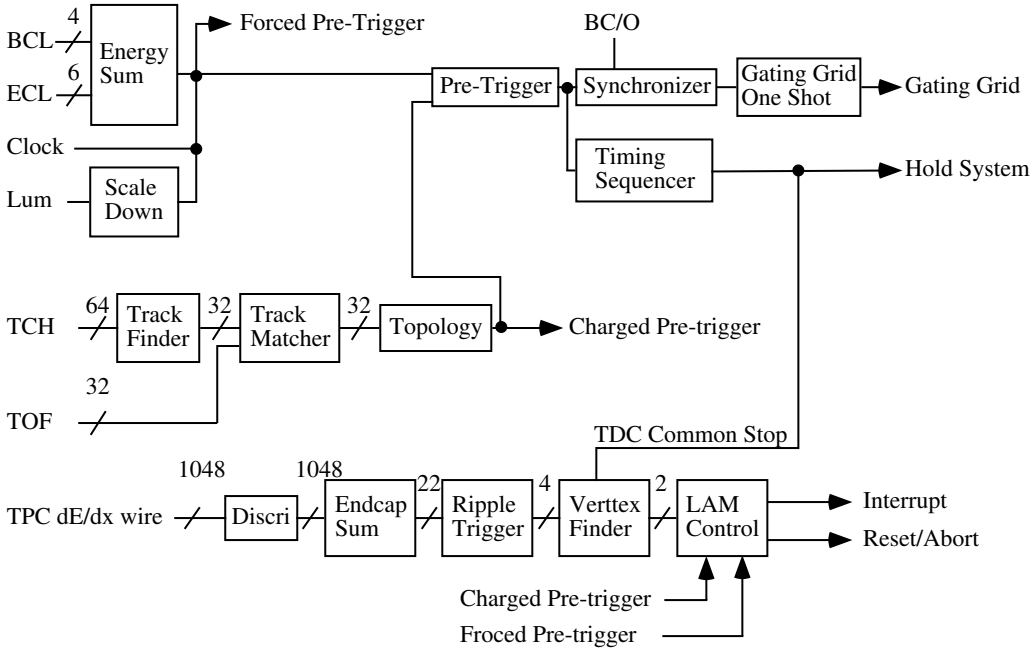

Figure 3.14: A block diagram of the TOPAZ trigger system.

3.3.1 Energy Trigger

A block diagram of the energy trigger is depicted in Fig.3.15. An energy trigger signal is generated when either one of the following conditions are met: The energy trigger signal forces the TPC gating grid to open. A typical trigger rate is ~ 1.4 Hz.

energy deposit	$\geq$	$4\ GeV$	in the BCL, or
	$\geq$	$10\ GeV$	in the ECL, or
	$\geq$	$2\ GeV$	in both ends of the ECL, or
	$\geq$	$1\ GeV$	in 2 out of 3 BCL segments.

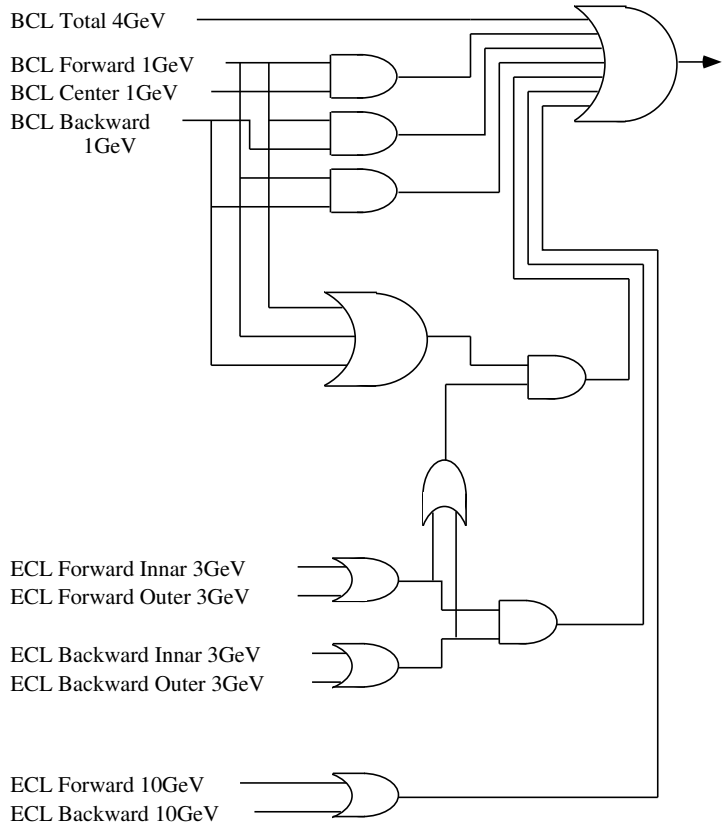

Figure 3.15: A block diagram of the TOPAZ energy trigger system.

3.3.2 Track Trigger

The track trigger is designed to accept low multiplicity events with little calorimeter energy deposit, such as $e^+e^- \rightarrow \mu^+\mu^-$ and two-photon events. The track trigger is roughly divided into two steps called charged pre-trigger and TPC trigger.

Charged pre-trigger

The pre-trigger opens the TPC gating grid to activate TPC. The pre-trigger rate is $10 \sim 100\ Hz$. The charged pre-trigger is issued when two or more tracks pass through the TCH and TOF. The track pre-trigger requires coincidence hits in the TCH and the TOF counter at the timing of BC/O. The TCH is azimuthally segmented into 64 sub-sectors. Each sector has a track finder based on the "table look-up method", using a 16K SRAM. A P_T-dependent mask is down-loaded by an online computer via a FASTBUS/CAMAC dataway. In the trigger decision, the 64 outputs from the track finder are ORed into 32 sectors. There are 64 TOF counters surrounding the TPC pressure vessel. The hit information in two adjacent counters is ORed to provide 32 sector signals. The pre-trigger recognizes the charged-track when the one hit in the TCH sector has a corresponding hit in the TOF counter as shown in Fig.3.16. The condition 1/32 : 3/32 means that one TCH sector is corresponded to the three TOF sectors, the azimuthally same one and both side of the adjacent ones. This condition determines a minimum acceptable P_T of a charged track since a low P_T track cannot hit the adequate region in the TOF. From the cosmic ray test, the charged track with $P_T > 0.3 \sim 0.7\ GeV/c$, depending the TCH-TOF combination, is triggered.

The pre-trigger is generated when at least two back-to-back track segments are found in the TCH (Fig.3.16). Each 32 sectors of TCH and TOF is paired into 16 sectors. The condition 1/16 : 7/16 means that "back-to-back" is defined to have one track segment in the TCH and another one in the seven TCH sectors, the opposite one and both side of the adjacent three's. This opening angle cut is effective to reject the spiral electron backgrounds. The opening angle condition in the used data was set to be greater than $45 \sim 70°$, depending on beam conditions.

TPC trigger

The TPC trigger uses signals from the innermost 88 sense wires. Contiguous 8 wires from one group, resulting in 11 groups. In each group, two sets of alternating four wires make two subgroups in each endcap, corresponding to 8 sectors, are

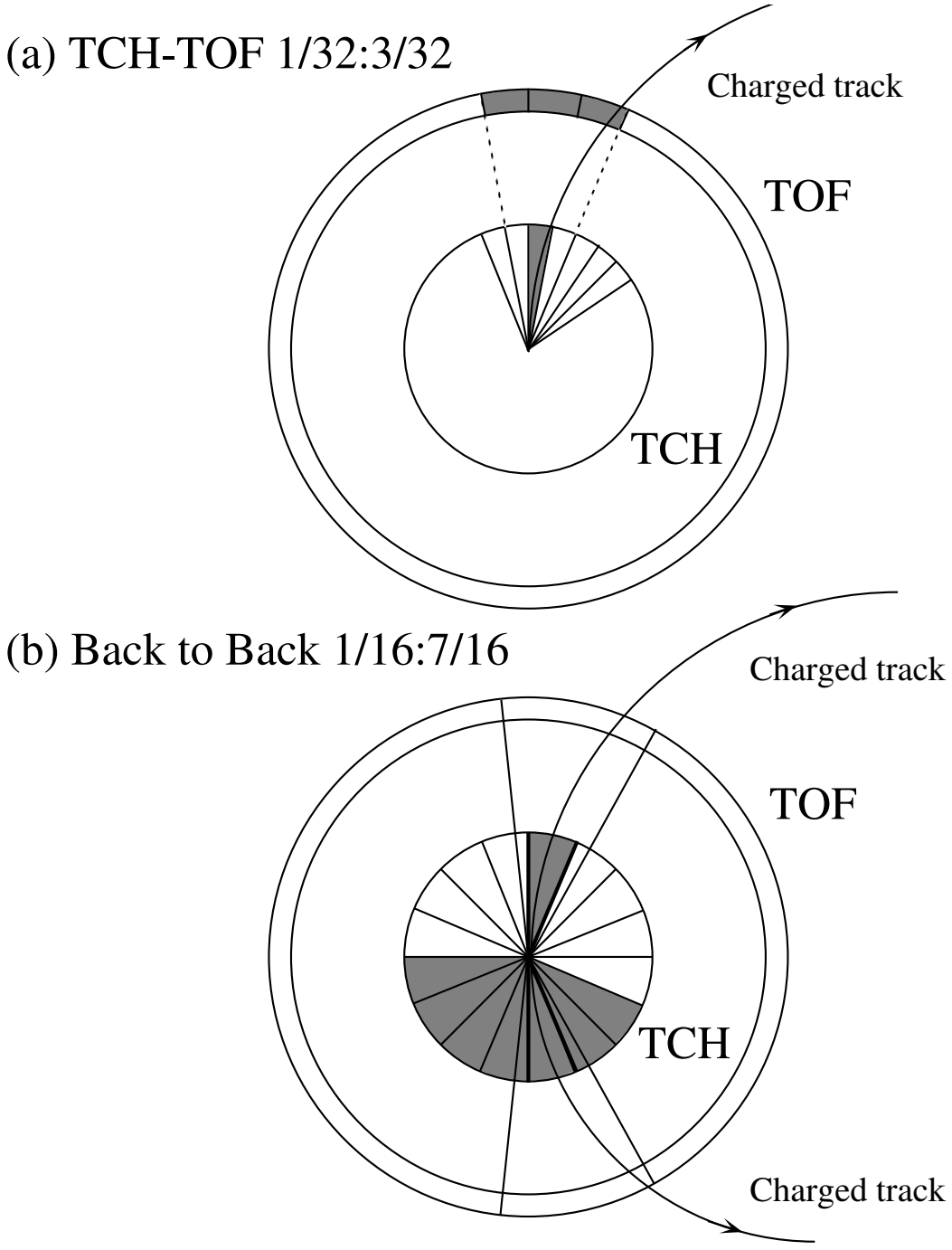

Figure 3.16: The principles of the track pre-trigger.

ANDed (Fig.3.17). Signals from 11 groups in each endcap, corresponding to 8 sectors, are ORed, and are stretched by one-shots of 1 μsec. These signals are processed by a trigger logic, named "ripple trigger". The ripple trigger requires 10 successive overlaps within them (Fig.3.18). The TPC trigger also checks the event vertex in r-Z plane. The vertex point is extrapolated with two signals, W1 and W2 in fig.3.19. The vertex cut is $\pm$ 20 cm from the interaction point in the Z-direction. This cut is crucial to reduce huge backgrounds such as beam-gas and beam-wall events.

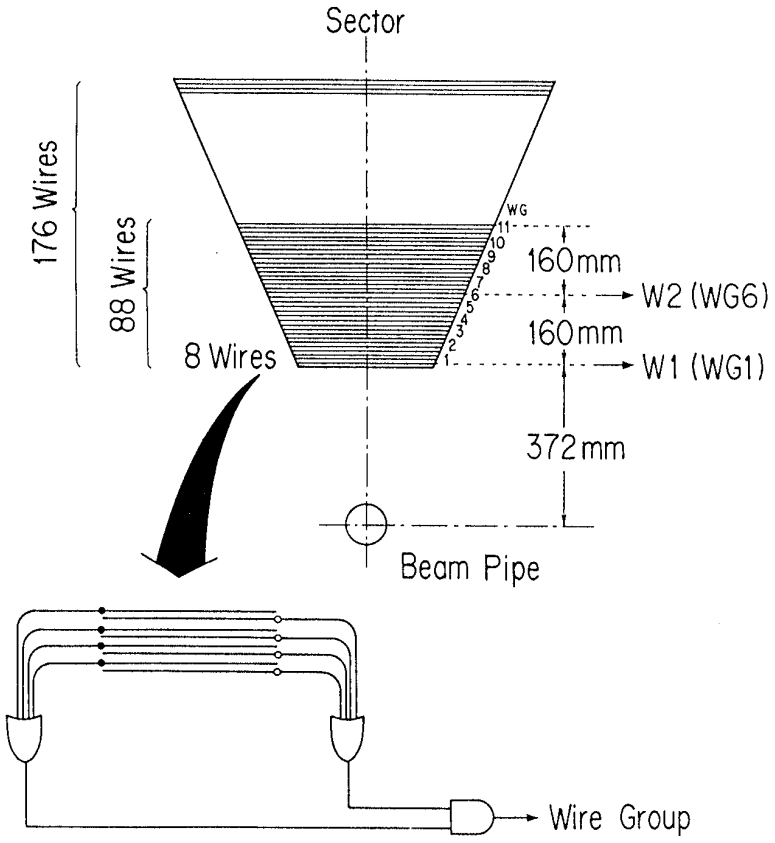

Figure 3.17: A TPC dE/dX wire configuration.

When an event is accepted by the trigger system, an interrupt signal is generated and the online computer starts data-taking, otherwise the system is reset by a Reset/Abort signal. In this trigger scheme, the trigger rate is $2 \sim 6$ Hz, and the dead time is $5 \sim 10$ %, depending on the beam condition.

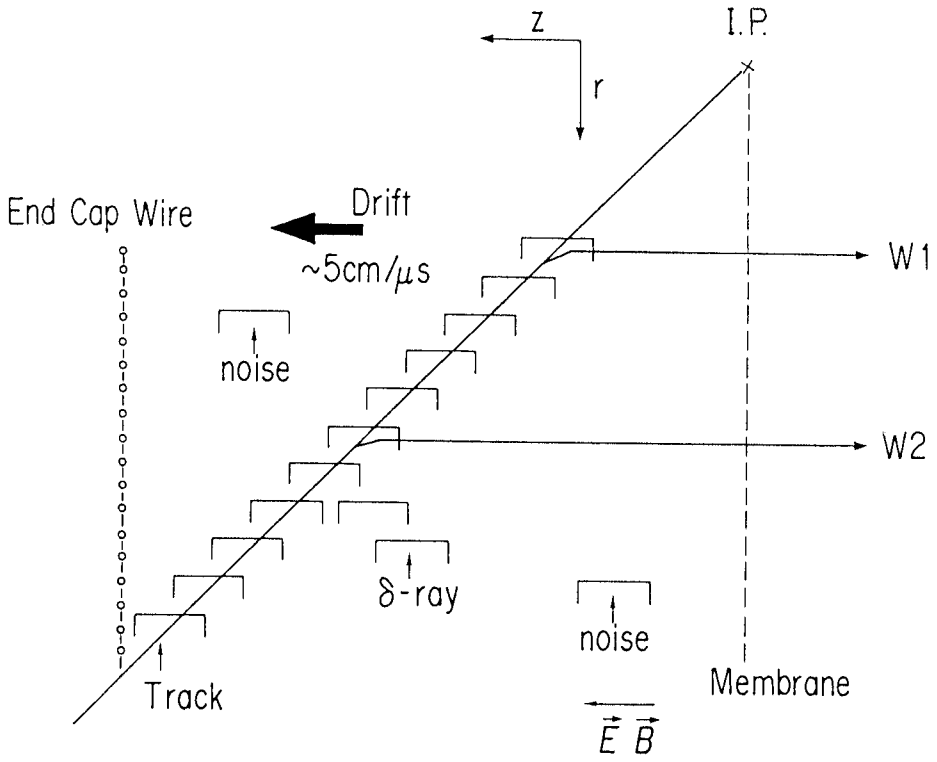

Figure 3.18: The principle of TPC ripple trigger.

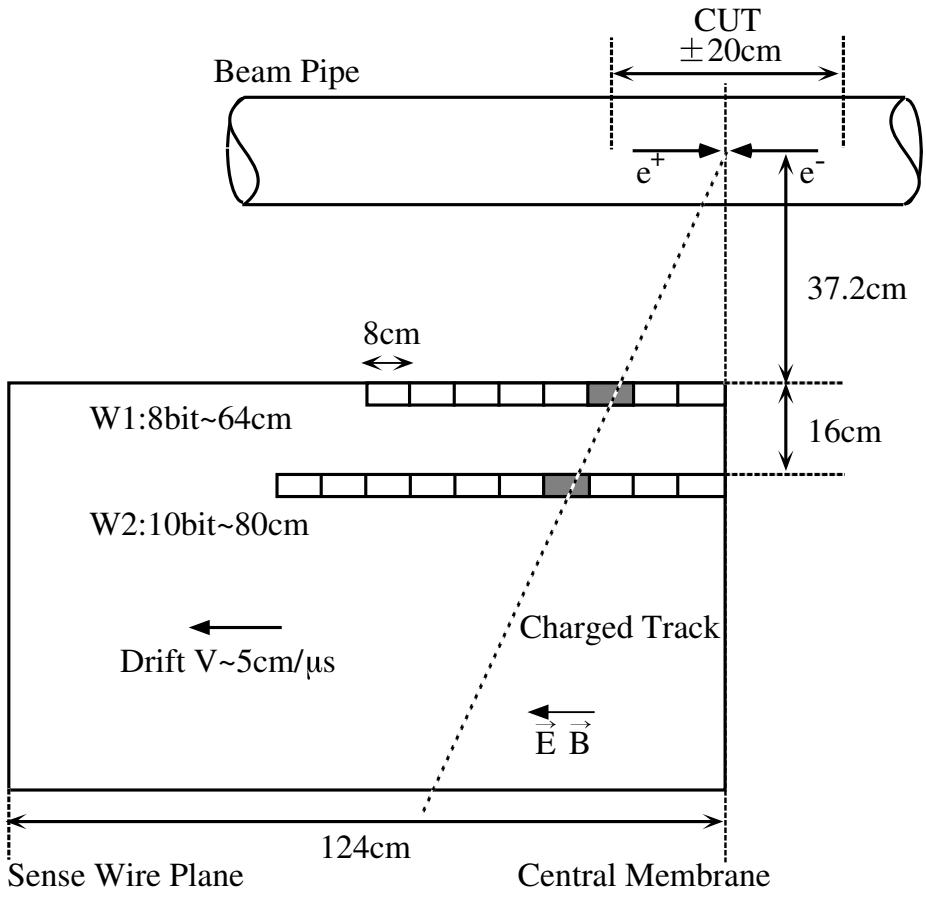

Figure 3.19: The principle of TPC vertex finder.

3.3.3 Software Trigger

The software trigger [46] was installed into TOPAZ trigger system in 1990 for the high luminosity run, because higher background was expected than Phase-I. The purpose of this trigger is to reduce the track trigger rate with small inefficiency by imposing Z resolution of the TPC trigger.

The software trigger consists of four micro-processors and TDC's. The TDC has the timing resolution of 100 $nsec$ and double pulse resolution of 1.5 μsec, which corresponds to 5 mm for spatial resolution and 7.5 cm for double track separation, respectively. The TDC reads 32 timing signals which are used in calculating the vertex point in the TPC trigger, and the four micro-processors calculate the vertex point precisely. Fig.3.20 shows the Z distributions of the track in the triggered event. The both lines are the cosmic ray data. The solid line is with the software trigger, and the dashed line is without that trigger. The FWHM of TPC triggered events is 60 cm, while that of software triggered events is 40 cm. The rate of charged track trigger was reduced to $30 \sim 40$ % with 0.5 % inefficiency.

Other trigger logics

In 1992, two new trigger logics were installed in the TOPAZ trigger system. One is called "cosmic veto trigger" which is designed to reduce the trigger rate by cosmic ray. This trigger is developed in order to save events with the energy less than 4.0 GeV without additional increase of the trigger rate. Now the threshold energy for the BCL in the energy trigger system is set to be 2 GeV.

The other is called "muon trigger", which requires the back-to-back muon event using the barrel muon chamber signals. This trigger is used to check the inefficiency of the present trigger system.

3.4 TOPAZ Data Acquisition System

The data from each detector element are taken by the online computer, VAX-11/780, via the FASTBUS system. Fig.3.21 illustrates the tasks working on the online computer. The data are then sent to the TRISTAN central computer, FACOM M-780, via an optical fiber link at $350 Kbytes/sec$. This offline computer carries out the rearrangement of the data format and quick analysis to check the data acquisition system. The data are also monitored by another VAX-11/780 connected to the online computer to verify the hardware triggers. At the same

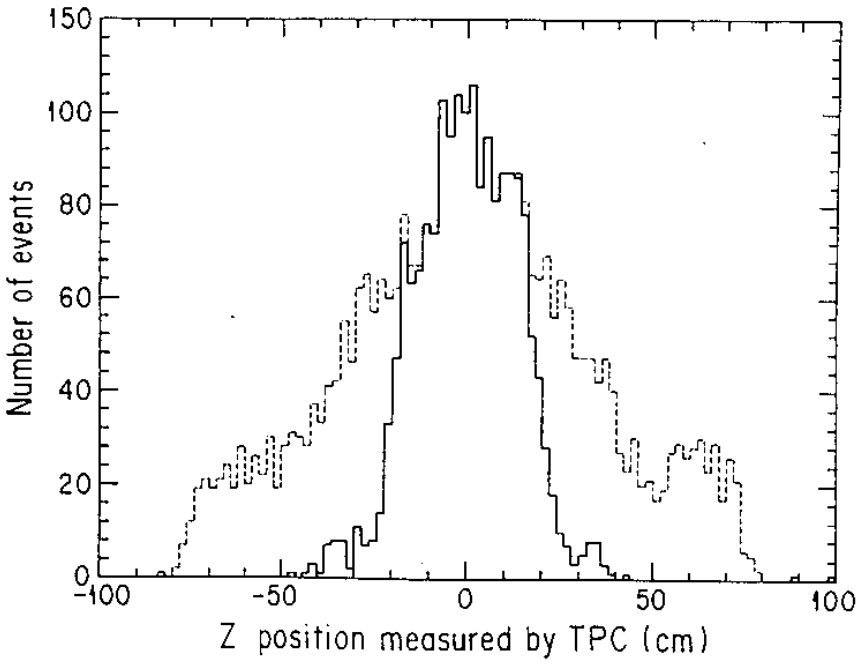

Figure 3.20: The Z distributions of the track in the triggered event. The both lines are the cosmic ray data. The solid line is with the software trigger, and the dashed line is without that trigger.

time, selected events are displayed on the screen of a high speed graphic terminal. To monitor environmental conditions, a μ−PDP 11/73 computer is employed to read temperatures pressures, gas flow rates and so on. These data are transferred to the online computer, and are included in the event record. The raw data processing methods at TOPAZ are presented in Appendix C.

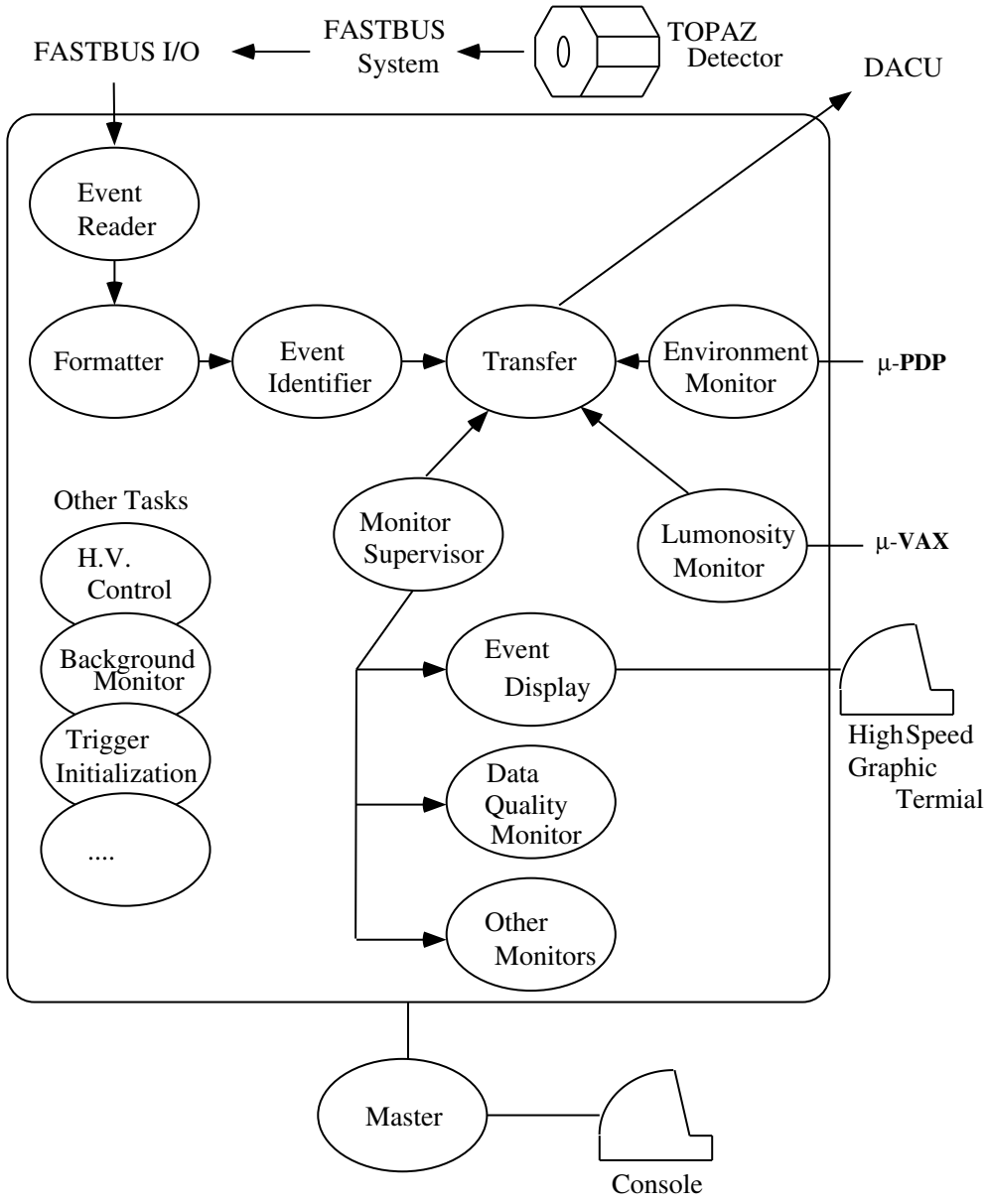

Figure 3.21: A flow chart of TOPAZ online computer system.

Chapter 4

Monte-Carlo Simulation

In this chapter, we describe the Monte-Carlo simulation used in this analysis in detail. In order to estimate the detection efficiency, the trigger acceptance of our detector and the background contributions, the Monte-Carlo simulation plays an important role. The Monte-Carlo simulation is composed of following two parts, namely, the event generation and the detector simulation. At first, the events in which we are interested are simulated according to the theoretical model with the event generator. Then generated particles are passed through the TOPAZ detector and forms the detector signals. The events generated in these steps are processed by the same event reconstruction as the data. Fig.4.1 shows the flow chart of data analysis and the Monte-Carlo simulation. The outputs from the simulator are the same format as those of the data.

4.1 Two-Photon Event Generations

In this section, the mechanism of the event generation is described. We used PYTHIA 5.720 [50] and PHOJET 1.05C [51] program packages as the two-photon event generator. Subsequently each generator is also introduced briefly.

The event generator for the process $e^+e^- \rightarrow e^+e^- + hadrons$ has following steps ;

1. $e^{\pm}$ beam particles are coming in towards each other. Each particles emit the photon according to Weizsäcker-Williams function given by Eq. (2.12).

2. Each photon is characterized by a set of parton distribution functions, which defines the partonic substructure in terms of flavor composition and energy sharing.

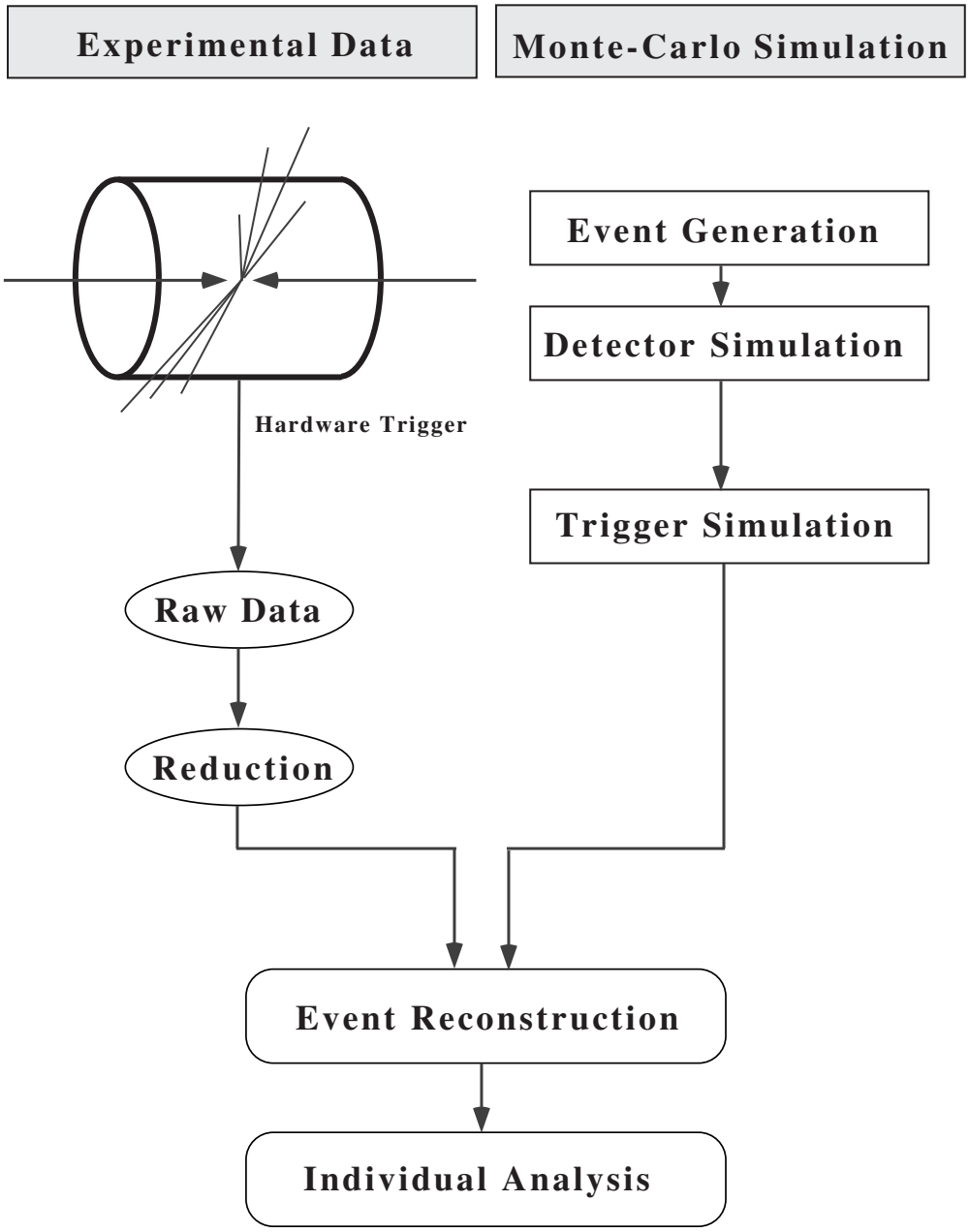

Figure 4.1: The analysis flow for data and Monte-Carlo simulation.

3. One shower initiator parton from each photon starts off a sequence of branchings, such as $q \rightarrow qg$, which build up an initial-state shower.

4. One incoming parton from each of the two showers enters the hard process, where then a number of outgoing partons are produced, usually two. It is the nature of this process that determines the main characteristics of the event.

5. Also the outgoing partons may branch, to build up final-state showers.

6. A photon remnant is left behind. This remnant may have an internal structure, and a net color charge that relates it to the rest of the final state.

7. The QCD confinement mechanism ensures that the outgoing quarks and gluons are not observable, but instead fragment to color neutral hadrons (hadronization).

8. Many of the produced hadrons are unstable and decay further.

The schematic view of this process is shown in Fig.4.2.

4.1.1 Parton Generation

Each partons is characterized by some virtuality scale Q^2, which gives an approximate sense of time ordering to the cascade. In the initial state shower, Q^2 values are gradually increasing as the hard scattering is approached, while Q^2 is decreasing in the final-state showers. Shower evolution is cut off at some lower scale Q_0, typically around 1 GeV for QCD branches. The same cut-off scale is also used to regularize the soft gluon emission divergences in the splitting kernels. PYTHIA deals with the initial- and final-state parton showers. Detailed descriptions of the initial-state and the final-state showers are found in reference [53] and [54], respectively.

4.1.2 Hadronization

The QCD perturbation theory, formulated in terms of quarks and gluons, is valid at short distances. At long distances, QCD becomes strongly interacting and perturbation theory breaks down. In this confinement regime, the colored partons are transformed into colorless hadrons. This process is called "hadronization" (or "fragmentation").

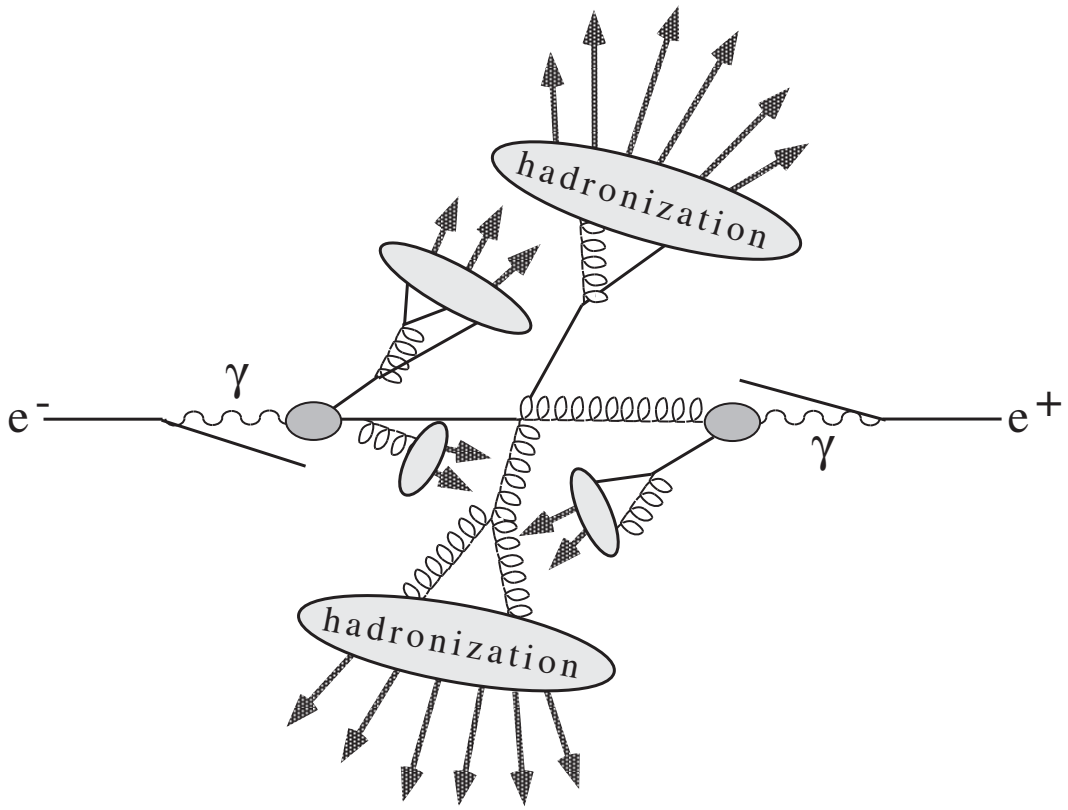

Figure 4.2: The schematic view of $e^+e^- \rightarrow e^+e^-$+ hadrons.

The hadronization process has yet to be described by the perturbative QCD. Therefore a phenomenological model to simulate the hadron production is needed. Three main models are usually distinguished, string fragmentation, independent fragmentation and cluster fragmentation. For the hadronization process, JETSET 7.408 [52] was used. JETSET is intimately connected with string fragmentation, in the form of the "Lund-Model".

To describe the properties of the hadronization, we used the fragmentation function, $f(z)$, which represents the probability that the hadron is found in the debris of a parton carrying a fraction z of its momentum. For the heavy quark (charm-quark and bottom-quark), the hadronization process is described by "Peterson function" [55],

$$f(z) \propto \frac{1}{z(1-\frac{1}{z}-\frac{\epsilon}{1-z})^2}.$$

Where parameter ϵ was set to be 0.050 for charm-quarks and 0.005 for bottom-quarks. And for the light quark, we used "symmetric Lund function"

$$f(z) \propto \frac{1}{z}(1-z)^a exp(-\frac{bm_T^2}{z}),$$

where m_T is the transverse mass of the hadron. The transverse momentum of hadron p_T is described by the Gaussian function

$$f(p_T) \propto exp(-\frac{p_T^2}{2\sigma_q^2}).$$

We set the parameters a, b and σ_q to be 0.5 GeV^{-2}, 0.84 GeV^{-2} and 0.358 GeV, respectively. These value were known to reproduce the data of the reaction $e^+e^- \rightarrow$ hadrons at LEP experiment.

PYTHIA

PYTHIA is a general purpose generator of high energy particle physics reactions. For the first approximation, photon is a point-like particle. However quantum mechanically, it may fluctuate into a charged fermion-antifermion pair as explained in section 2.3. The spectrum of $\gamma \leftrightarrow q\bar{q}$ fluctuations may be split into a low virtuality and a high virtuality part. The former part can be approximated by a sum over low mass vector-meson states, customarily restricted to the lowest lying vector multiplet. Phenomenologically, this VDM ansatz turns out be very successful in describing data. The high virtuality part, on the other hand, should be in a perturbatively calculable domain. Based on the above separation, PYTHIA distinguishes three main classes of interacting photons *i.e.*, direct, VDM and anomalous

processes. As explained in section 2.6, the resolved process comprises the VDM state and the anomalous state.

For a $\gamma\gamma$ interaction, there are six event classes as follows :

1. VDM $\times$ VDM : both photons turn into hadrons, and the processes are the same as allowed in hadron-hadron collisions.

2. VDM $\times$ direct : a bare photon interacts with the partons of the VDM photons.

3. VDM $\times$ anomalous : the anomalous photon perturbatively branches into a $q\bar{q}$ pair, and one of these (or a daughter parton) interacts with a parton from the VDM photon.

4. Direct $\times$ direct : the two photons directly give a quark pair, $\gamma\gamma \to q\bar{q}$.

5. Direct $\times$ anomalous : the anomalous photon perturbatively branches into a $q\bar{q}$ pair, and one of these (or a daughter) directly interacts with the other photon.

6. Anomalous $\times$ anomalous : both photons perturbatively branch into $q\bar{q}$ pairs, and subsequently one parton from each photon undergoes a hard interaction.

The relations between the above classes and the sub-processes in this analysis can be summarized in Table 4.1. The one-resolved process corresponds to the class of 2 and 5, and the two-resolved process corresponds to the class of 1, 3 and 6. Hereafter, we will regard both the VDM and the anomalous states as "resolved process" unless special notice is given.

The contributions from the direct and the resolved processes are mixed according to the recommendation of the model [49]. We simulated the lightquark (u, d, s) production and the heavy quark (c) production separately and then, these two distributions were normalized by these luminosities and were added. The conditions of the PYTHIA program used in this analysis are summarized in Table.4.2.

PHOJET

PHOJET is a minimum bias event generator for hadronic pp, γp and $\gamma\gamma$ interactions. The interactions are described within the Dual Parton Model (DPM) [56] in terms of reggeon and pomeron exchanges. Regge arguments are combined with

Sub-process		class
Direct	$\gamma\gamma \to q\bar{q}$	4
One-resolved	$\gamma q \to qg$	2,5
	$\gamma g \to q\bar{q}$	
Two-resolved	$qq' \to qq'$	1,3,6
	$q\bar{q} \to q'\bar{q}'$	
	$q\bar{q} \to gg$	
	$qg \to qg$	
	$gg \to q\bar{q}$	
	$gg \to gg$	

Table 4.1: The relations between the sub-processes and the classes. q' also represent an antiquark.

Item	Condition
Center of mass energy	58.0 GeV
Minimum $\hat{P}_T$ of parton	1.6 GeV/c for light quark production
Maximum Q^2 scale	2.6 $(GeV/c)^2$
Mass of charm quark	1.35 GeV/c^2
Photon structure function	GRV-LO
Multiple interaction	on

Table 4.2: The conditions for PYTHIA.

perturbative QCD to get an almost complete description of the leading event characteristics. Special emphasis is taken on diffractive and soft interactions. Soft and hard interactions are unitarized together leading to the possibility to have multiple soft and hard scattering in one event. The conditions are summarized in Table.4.3.

Item	Condition
Center of mass energy	58.0 GeV
Minimum $\hat{P}_T$ of parton	2.0 GeV/c
Photon structure function	SaS1D
Multiple interaction	on

Table 4.3: The conditions for PHOJET.

4.2 Detector Simulation

After being produced by the Monte-Carlo event generator, each event swims in the TOPAZ detector simulator. The structures and materials in the TOPAZ detector are precisely described in the simulator and the behavior of the particles in the detector is emulated step-by-step along its path. At each step, such interactions as the energy loss, the multiple scattering and the bremsstrahlung take place according to the probabilities associated with them. In the dense materials, the Electron Gamma Shower (EGS) code is used to simulate electromagnetic interactions. The nuclear interaction is handled by the GEISHA code [57]. The finite beam size of the TRISTAN accelerator is accounted for by smearing the nominal interaction point by a Gaussian distribution in the X-Y plane. The short-lived particles such as K_S, π_0 and Λ are decayed in the simulator leaving the secondary vertex information.

In the TPC region the averaged energy loss in the gas is calculated according to a formula determined from the minimum ionizing pions in data, knowing the velocity and charge of the particle. The Landau fluctuation is taken into account by smearing the energy loss so as to be consistent with the experimental distribution. The smeared energy loss is translated to a pulse height on the corresponding wire to be sampled in order to mimic the digitized outputs. Because the time profile of the wire signal was experimentally found to be independent of the track angle, a single pulse-height shape function is used to calculate the pulse height

in each time bucket. The pulse height is digitized if it is above the threshold, and is recorded as wire information. Pad signals are generated using the pulse heights of the relevant five wires near to the pad rows. The avalanches on the five wires induced a charge along the pad row. We assume that the induced charge is a Gaussian distribution, and is proportional to the corresponding wire pulse heights. The width of the Gaussian and the weight factors for the five wires are determined experimentally [59].

In the BCL region, the electromagnetic showering process is simulated using the "Bootstrap method" [58]. In the bootstrap method, the energy deposits of the particles are calculated using the program EGS when the energy of the particle is relativity high. However, since the EGS takes relatively longer CPU time when the particle energy becomes low, another method is used when the energy of the particle becomes than 100 MeV. This method is based on the table search of the pre-calculated shower energies corresponding to various incident energies of particles and gives the fast-calculation of the shower energy. The calculated shower energy is finally translated into the pulse heights of photomultipliers attached to the each lead glass counter.

In the ECL region, the shower simulation is carried out by using EGS code without any complication.

4.3 Trigger Simulation

The charged track trigger conditions which determine the minimum P_T threshold of the tracks are directly related to the experimental results when we analyze the two-photon events. The detection efficiencies for two-photon events are in general sensitive to the charged track trigger condition because of their low momentum and low multiplicity of tracks. Through the experiments, the charged track trigger conditions are changed according to the beam conditions. The conditions in each experimental period are summarized in Table. 4.4. These changes of the trigger conditions were took into account in the Monte-Carlo simulator.

The minimum P_T threshold of the track pre-trigger was determined by the combination of the TCH and TOF signals. Fig.4.3 shows the trigger efficiency curve as a function of the track P_T. The points with the error bars are the measurements by taking cosmic rays. The solid lines are the trigger efficiencies estimated from the trigger simulations. The charged tracks whose P_T is greater than 0.35, 0.50 and 1.0 GeV/c can be triggered almost perfectly with the TCH-TOF trigger conditions of 1/32 : 7/32, 1/23 : 5/32 and 1/32 : 3/32. Both results

$\sqrt{s}$	Integrated Luminosity			Track trigger condition			
				pre-trigger		TPC	Software
(GeV)	(pb^{-1})			TCH-TOF	Back to Back	trigger	trigger
58.0	1.640	± 0.030	± 0.028	1/32-3/32	1/16-3/16	1/8-5/8	on
58.0	0.394	± 0.010	± 0.007		1/16-7/16	1/8-3/8	
58.0	2.015	± 0.030	± 0.034		1/16-3/16		
58.0	0.343	± 0.013	± 0.006				
58.0	4.422	± 0.049	± 0.075				
58.0	12.17	± 0.080	± 0.207				
58.0	7.405	± 0.066	± 0.126	1/32-7/32	1/16-9/16		
58.0	20.56	± 0.134	± 0.350				
58.0	4.391	± 0.050	± 0.075				
58.0	35.80	± 0.143	± 0.609				
58.0	8.296	± 0.070	± 0.141		1/16-5/16		
58.0	16.88	± 0.100	± 0.287				
57.6-59.95	9.868	± 0.084	± 0.168				
58.0	48.89	± 0.171	± 0.831				
58.0	4.004	± 0.048	± 0.068				
58.0	6.349	± 0.067	± 0.108				
58.0	3.237	± 0.048	± 0.055	1/32-5/32			
58.0	34.08	± 0.157	± 0.579				
58.0	16.14	± 0.108	± 0.274				
58.0	1.664	± 0.035	± 0.028				
58.0	4.581	± 0.058	± 0.078				
58.0	27.93	± 0.128	± 0.475				
58.0	16.78	± 0.099	± 0.285				

Table 4.4: The charged track trigger conditions for used data. The first errors of Integrated Luminosity indicate the statistical errors, and the second errors are systematic errors. The data at $\sqrt{s}$ = 57.6-59.95 GeV were for energy scan. The center of mass energy had changed in order of 59.7 GeV, 58.2 GeV, 59.2 GeV, 58.45 GeV, 58,7 GeV, 58.95 GeV, 59.95 GeV and 57.6 GeV.

from the trigger simulations and the cosmic ray events agree within the error bars.

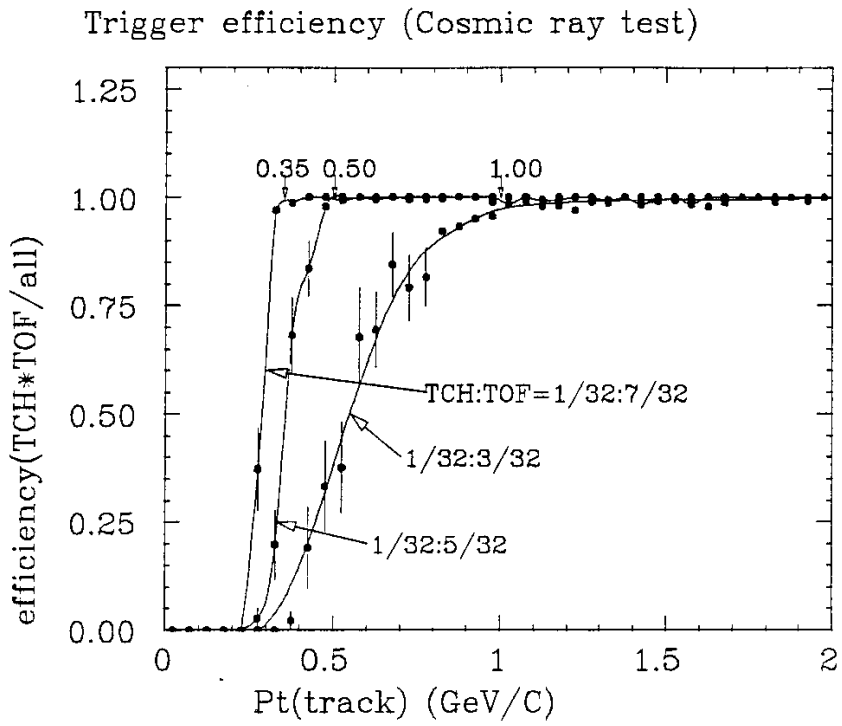

Figure 4.3: The trigger efficiencies. The points with the error bars are the cosmic ray data. The solid lines are the trigger efficiencies estimated with the trigger simulations.

Chapter 5

Event Selection

In this chapter, we describe the selection criteria for the hadronic events in the two-photon process ;

$$e^+e^- \rightarrow (e^+e^-) + \text{hadrons},$$

as well as that in e^+e^-annihilation process[†] ;

$$e^+e^- \rightarrow \text{hadrons}.$$

The former process is also called "$\gamma\gamma$ collisions" ;

$$\gamma\gamma \rightarrow hadrons,$$

since we select only events that the final state electrons are scattered in low angle region. With the selected hadronic events, we search for jet production by using jet cone algorithm.

Data used in this analysis correspond to the integrated luminosity of 287.8 pb^{-1}, which are almost full data taken with the TOPAZ detector in the data taking period from 1987 to 1995. The backgrounds contained in the final sample are also estimated from data themselves and Monte-Carlo simulation.

5.1 Two-Photon Event Selection

The hadronic event comprises charged tracks and the neutral clusters. For the TOPAZ detector, the former are detected with a Time-Projection Chamber (TPC) and the latter with a Barrel Calorimeter (BCL), Endcap Calorimeter (ECL) and Forward Calorimeter (FCL). We first describe the conditions used to select "good"

[†] e^+e^-annihilation events are used for analysis of jet profile in Chapter 7.

charged tracks and neutral clusters. Where "good" means that tracks and clusters are well-measured with those devices. To ensure this point, we need to limit fiducial volume of those devices and energy (momentum) ranges of clusters (tracks).

Charged track conditions

We imposed the following conditions for the charged tracks ;

(i) Minimum distance between a charged track and the beam interaction point ($|Z_{closest}|$, $|R_{closest}|$) :
Z-direction : $|Z_{closest}| \leq 15\ cm$,
X-Y plane : $|R_{closest}| = \sqrt{X^2_{closest} + Y^2_{closest}} \leq 4.0\ cm$,

(ii) Absolute value of the cosine of the polar angle ($|cos\theta|$) :
$0.02 < |cos\theta| \leq 0.85$,

(iii) Transverse momentum (P_T) :
$P_T \geq 0.10\ GeV/c$,

(iv) Number of degrees of freedom in track fitting (NDF) :
NDF ≥ 3,

(v) Unique determination of a track in track fitting.

The condition (i) selects tracks which originated from the beam interaction point. As will be described later, the condition of $|Z_{closest}|$ is set loosely in order to study the effects from beam-gas backgrounds. The condition (ii) means that the track exists within the TPC sense volume avoiding the TPC central membrane, which is located at $\theta = 90°$. The conditions (iii), (iv) and (v) ensure that a track is cleanly reconstructed even if the track can not reach the outer vessel of TPC.

Neutral cluster conditions

For neutral clusters, following conditions were used ;

(i) Deposit energy in FCL (E_{FCL}) :
$E_{FCL} \geq 0.5\ GeV$,

(ii) Deposit energy in ECL (E_{ECL}) :
$E_{ECL} \geq 0.3\ GeV$,

(iii) Deposit energy in BCL (E_{BCL}) :
$E_{BCL} \geq 0.2\ GeV$,

(iv) Absolute value of the cosine of the polar angle of ECL ($|cos\theta_{ECL}|$) :
$0.848 \leq |cos\theta_{ECL}| \leq 0.966$.

(v) Absolute value of the cosine of the polar angle of BCL ($|cos\theta_{BCL}|$) :
$|cos\theta_{BCL}| \leq 0.83$.

The conditions (i), (ii) and (iii) reject noise or fake hits in the calorimeters. The condition (iv) and (v) ensure the fiducial volume of ECL and BCL, respectively. We also remove clusters which associate with TPC tracks. When the distance between the BCL cluster and the point extrapolated from the TPC track is less than 15 cm, and the energy of cluster measured with BCL is less than 1 GeV, that cluster was regarded as the charged particle which has passed through the calorimeter depositing the minimum ionizing energy.

Using these "good" tracks and "good" clusters, we imposed the conditions as shown in the followings for the selection of the hadronic two-photon events ;

1. Number of the charged tracks in the TPC must be at least 4,

2. Visible energy ($E_{visible}$) :
$E_{visible} \leq 35\ GeV$,

3. Mass of the observed hadron system ($W_{visible}$) :
$2 \leq W_{visible} \leq 35\ GeV/c^2$,

4. Position of the event vertex, which is reconstructed from all charged tracks ($|Z_{vertex}|$, R_{vertex}) :
Z-direction : $|Z_{vertex}| \leq 3.0\ cm$,
X-Y plane : $R_{vertex} = \sqrt{X^2_{vertex} + Y^2_{vertex}} \leq 3.0\ cm$.

5. Energy of the most energetic cluster appearing in BCL, ECL and FCL must be less than $0.25 \times E_{beam}$, where E_{beam} is the beam energy.

In the calculation of $E_{visible}$ and $W_{visible}$, both charged tracks in TPC and neutral clusters in BCL and ECL are used. The pion mass is assigned to all charged tracks. With the criterion-1, we rejected low-multiplicity events such as lepton pair production. Hadronic events in e^+e^-annihilation process can be removed with the criterion-2. The criterion-3 removes low energy resonance-production events in $\gamma\gamma$ collision. To remove beam-gas backgrounds, we applied vertex cuts in the criterion-4. Fig.5.1 shows the Z_{vertex} distribution. In this figure a clear peak, caused by events from beam interaction above flat backgrounds, is observed. A selected region are shown by a single-hatched area. The criterion-5 ensures the

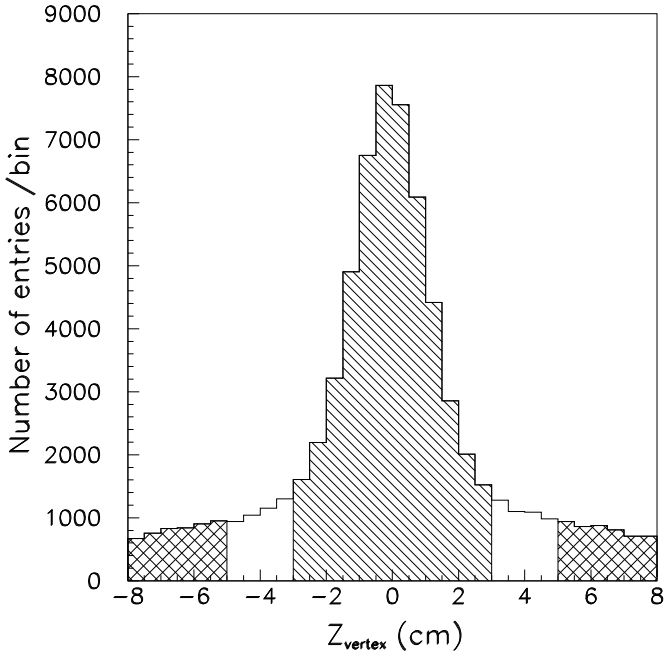

Figure 5.1: Z distribution for the reconstructed event vertex. The singly-hatched area is a signal region and the double hatched areas show the regions used to estimate beam-gas backgrounds.

anti-tag condition of the scattered electrons. This condition limits the scattering angles of the beam electrons to be less than 3.2°, which corresponds to the maximum virtuality of the photon $(Q^2) \sim 4\ (GeV/c)^2$. This condition ensures that selected hadronic samples come from the (quasi-) real $\gamma\gamma$ collisions. This removes the sample from deep inelastic $\gamma\gamma$ scattering.

The numbers of events which survived at each selection cut are summarized in Table 5.1. Finally, 285,941 of anti-tag hadronic events have passed all the criteria. An example of the typical hadronic event which remained in the above criteria is shown in Fig.5.2. As can be seen from this figure, relatively small number of reconstructed tracks and clusters are observed. In $\gamma\gamma$ collision, the final hadrons are one-sided ($-Z$ side in this example), but are roughly back-to-back in X-Y plane. These configurations are due to unbalanced momenta which are carried away by the beam electron.

Selection item	Number of passed events
Number of tracks ≥ 4	573,681
$E_{visible} \leq 35\ GeV$	572,688
$2 \leq W_{visible} \leq 35\ GeV/c^2$	515,331
Vertex Cut : $R_{vertex} \leq 3\ cm$	513,375
Vertex Cut : $\lvert Z_{vertex} \rvert \leq 3\ cm$	303,301
Anti-tagged of : BCL and ECL	298,551
Anti-tagged of : FCL	285,941

Table 5.1: The numbers of survived events at each selection cut.

5.2 Annihilation Event Selection

We also used e^+e^-annihilation events for the study of jet profile in the later section. We then describe criteria used to select hadronic events produced in e^+e^-annihilation process. We adopted the standard hadronic selection criteria, which have been frequently used in the TOPAZ collaboration [60]. We cite here the selection criteria for the e^+e^-annihilation process as follows ;

1. There are at least 5 charged tracks in TPC. The charged track must satisfy following conditions ;

   - $r < 5\ cm$ and $\lvert z \rvert < 5\ cm$ at the closest point to the beam axis.

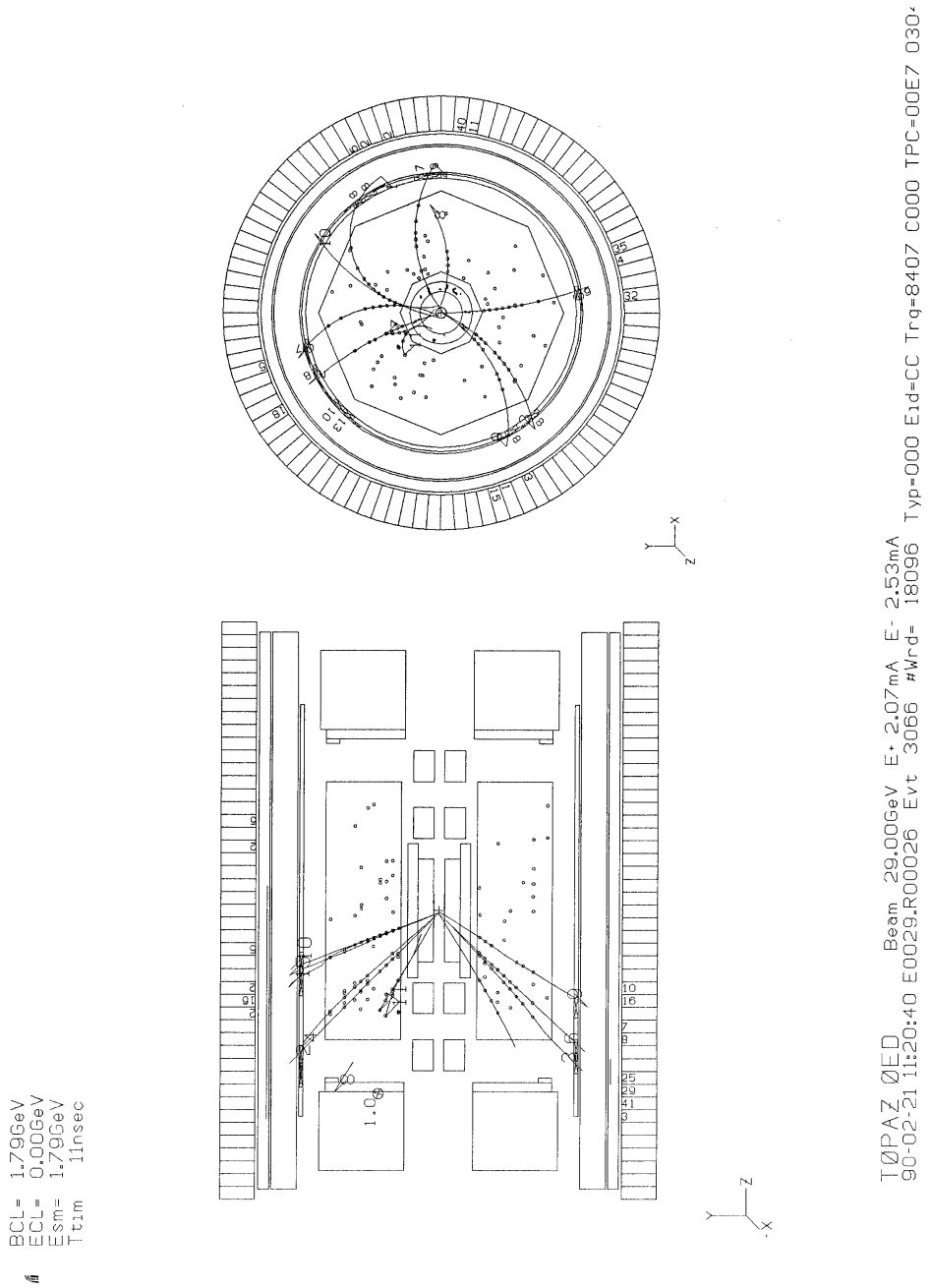

Figure 5.2: A typical jet production in two-photon event. Left side is Y-Z view and right side is X-Y view. Detectors are indicated to BCL. Solid lines from beam interaction point are reconstructed tracks.

- The momentum projection onto X-Y plane (P_T) is greater than 0.15 GeV/c.
- The absolute value of cosine of the polar angle of TPC track is less than 0.83.

2. Visible energy $E_{visible}$ is greater than the beam energy, E_{beam}. Where, $E_{visible}$ is defined as the sum of the energy of BCL, the energy of ECL and the energy of TPC tracks (passed through cut 1). TPC tracks are assumed to be pions.

3. Balance of the momentum projected onto the beam axis is less than 0.4 ;

$$\frac{\sum p_Z}{E_{visible}} < 0.4$$

4. Larger invariant mass of two hemisphere is greater than 2.5 GeV/c^2. Where, two hemisphere is divided by a plane perpendicular to thrust axis. The thrust T is defined as ;

$$T = max \left[\frac{\sum_i |\vec{p_i} \cdot \vec{n}|}{\sum_i |\vec{p_i}|} \right]$$

and the unit vector $\vec{n}$ is called thrust axis.

5. The number of the electromagnetic clusters which have the energies greater than half of the beam energy $E_{beam}/2$ is less than 2.

Above criteria were applied to 278.0 pb^{-1} of TOPAZ data and finally, 29,184 hadronic events in e^+e^-annihilation process remained.

5.3 Jet Selection

In the real experiment, one can not directly measure the final state of the quark and gluon due to the QCD color confinement. Only final state hadrons, which are color neutral, can be measured in the experiment. However, it is well known that the final state in hard scattering exhibits a jet-like shape (*i.e.* a collimated particle flows) in the approximately same direction of the parton produced in hard scattering sub-processes. Therefore observation of jets is a direct evidence that the reaction caused by a hard parton-parton scattering. In Fig.5.2, jet-like structures are clearly seen. In order to study jet-like structure quantitatively, there exist several definition of the jet as described in the following subsection.

5.3.1 Jet Finding Algorithm

There can be categorized globally into two kinds of jet finding algorithms which have been currently used in high energy experiments. One is the "cluster algorithm", and the other is the "cone algorithm".

The idea of the cluster algorithm is that the iteration of merging two close clusters results in several well-separated jets. There are famous two cluster algorithms : one is called k_T algorithm [62] [63], and the other is JADE type algorithm [61]. For the JADE type algorithm, for examples, squared invariant mass is chosen as a measure in the distance. The cluster algorithm has an advantage that any particle is finally assigned to one of some jets. However, in case that the event contains photon remnants or underlying events, the reconstruction is distorted by particles from these final states.

On the other hand, the principle of the cone algorithm is to define a jet within a given cone. Usually the cone is expressed by a circle in the η-ϕ space, and the maximum transverse energy (E_T) is searched for within the cone. Here, η is the pseudo-rapidity[†] and ϕ is the azimuthal angle. Hence the cone algorithm is invariant to the boost along the beam axis and has been mainly developed and used in hadron-hadron collider experiments.

In this analysis, we adopted the cone algorithm to search for jet production in $\gamma\gamma$ collisions. A detailed cone algorithm used in this analysis is as follows ;

1. Search for a seed particle which has the maximum transverse energy (E_T). This particle is regarded as the temporary center of a cone.

2. Particle which satisfies the following condition is inside the cone.

$$\sqrt{(\eta^{jet} - \eta^{particle})^2 + (\phi^{jet} - \phi^{particle})^2} \leq R,$$

where η^{jet} and ϕ^{jet} is the jet axis and R is cone radius. Particles within a cone are gathered and formed a jet. The transverse energy of the jet (E_T^{jet}) is conventionally calculated by summing up transverse energy ($E_{T_i} = E_i \cdot sin\theta_i$) of all particles within a jet cone of radius R [64]. η^{jet} and ϕ^{jet} are determined by taking a weighted average of the transverse energy of each particle (E_T).

$$E_T^{jet} = \sum_i^{particle} E_{T_i}$$

$$\eta^{jet} = \frac{\sum_i^{particle} E_{T_i} \cdot \eta_i}{\sum_i^{particle} E_{T_i}}$$

$$\phi^{jet} = \frac{\sum_{i}^{particle} E_{T_i} \cdot \phi_i}{\sum_{i}^{particle} E_{T_i}}$$

3. New cone around new axis is formed and the procedure of step 2 is repeated.

The iteration is stopped when particles contained in the jet are not changed to the next iteration. In case when the plural jets overlap each other, the particles in the overlapped region were assigned to the higher E_T^{jet} jet. Finally, if E_T^{jet} is greater than a certain threshold the candidate is defined as a jet.

In the later section, we used jet threshold of 1.0 GeV to select jet loosely. But while in detailed analysis of dijet events, we used threshold at 3.0 GeV for the highest E_T jet and 2.0 GeV for the second highest E_T jet. The radius of jet cone was set to 1.0.

5.3.2 Jet E_T Correction

Detectors generally have finite resolution and limited acceptance, and these effects are different for each detector. In order to compare our results with those of other experiments or with theoretical predictions, we have to make correction of detector effects to get the original distribution. In this analysis, the correction of detector responses is made up by two parts : at first the correction of the jet quantities (E_T^{jet}, η^{jet} and ϕ^{jet}) is performed, and then the other remaining corrections (acceptance and so forth) are carried out to the distribution based on the corrected jet. In this subsection, the procedure of the jet correction is explained. Other corrections will be described in section 7.2.

As described in section 4.1, the current theoretical framework generally describes the formation of the hadronic final state in three steps - (1) calculation of the cross section in the parton level, (2) creation of the parton shower and (3) hadronization. In addition there is one more step that the detector smears the original hadronic final state. At first, we need to determine to which level the detector information is corrected.

1. partons from the calculation of the matrix element (parton level),

2. partons after the parton shower (parton shower level),

†pseudo-rapidity is defined as $\eta \equiv -ln\ tan(\theta/2)$, where θ is the scattered angle.

3. hadrons after the hadronization (hadron level),

4. the detector response (observed level).

The step 1, 2 and 3, generally, depend on theoretical models and Monte-Carlo programs we use. However in the step 4, the detector response is a property of the detector itself. In this analysis, only the detector effects have been corrected and the distributions at the hadron level are presented as measured quantities. This is the most model independent way of data presentation. The data from HERA experiment are also presented this way.

In order to study the detector effect, we study the correlation of the jet quantities (E_T^{jet}, η^{jet} and ϕ^{jet}) between the hadron level and the observed level by using Monte-Carlo simulation.

As the Monte-Carlo simulator, the PYTHIA generator with GRV-LO photon structure function has been used. In this study, jets at the hadron level and the observed level are reconstructed with the same cone algorithm with the cone radius $R = 1.0$. Correlations of jet quantities E_T^{jet}, η^{jet} and ϕ^{jet} are then checked for jets with $E_T^{jet} \geq 1.0\ GeV$ and $|\eta^{jet}| \leq 1.0$ conditions. The correspondence between jets at the hadron level and the observed level is determined from their jet directions (η, ϕ). The nearest ones at the hadron level and the observed level are chosen. And if that difference $r_{min} = \sqrt{(\eta^{jet}_{hadron} - \eta^{jet}_{observed})^2 + (\phi^{jet}_{hadron} - \phi^{jet}_{observed})^2}$ is larger than 0.2, we regarded there are no corresponding jets. Fig.5.3 shows the distribution of r_{min}.

Figs.5.4 show correlations of various jet quantities between the hadron level and the observed level. Fig.5.4(a) is the correlation of number of reconstructed jets. Almost all event has two jets at both level. Fig.5.4(c) and Fig.5.4(d) are η^{jet} and ϕ^{jet} correlations, respectively. The distributions of η^{jet} and ϕ^{jet} show quite good correlations at the hadron and the observed level, so that we did not correct η^{jet} and ϕ^{jet}. The resolutions of η^{jet} and ϕ^{jet} are about 0.09 and 0.19 $radian$, respectively and these values are comparable with their bin widths. On the other hand, E_T^{jet} correlation, given in Fig.5.4(b) shows more broad distribution than that of η^{jet} and ϕ^{jet}.

We determined the correction factor for $E^{jet}_{T\,observed}$ by the following method ;

1. Divide $E^{jet}_{T\,hadron}$ region into several sub-regions in Fig.5.4(b).

2. In each $E^{jet}_{T\,hadron}$ sub-region, the distribution is projected onto the $E^{jet}_{T\,obserbed}$ axis.

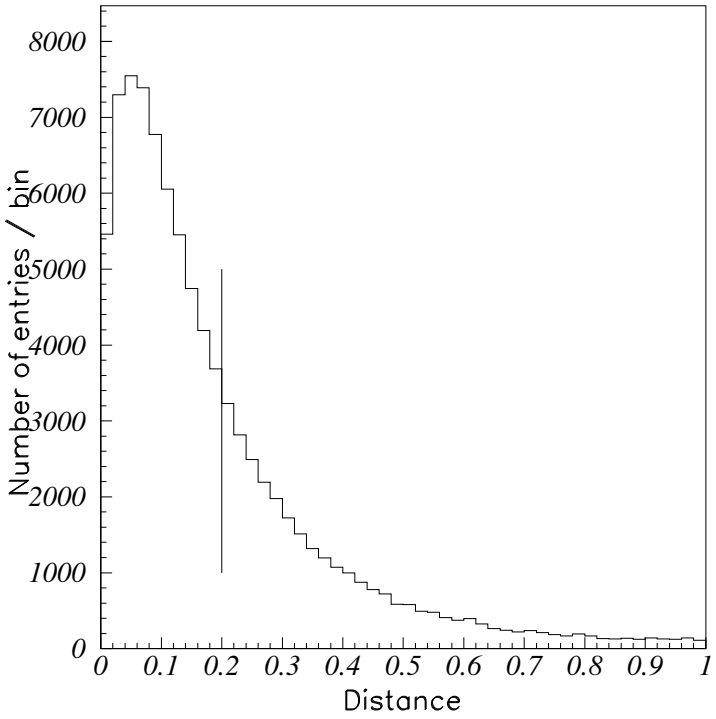

Figure 5.3: The distance between the hadron jet and the observed jet in $\eta - \phi$ plane.

3. In each $E_{T\,hadron}^{jet}$ sub-region, the projected distribution of $E_{T\,observed}^{jet}$ is fitted by a single Gaussian and each mean value is obtained. The $E_{T\,observed}^{jet}$ distribution in each $E_{T\,hadron}^{jet}$ sub-region is shown in Figs.5.5.

4. Mean value in each $E_{T\,hadron}^{jet}$ sub-regions is plotted against $E_{T\,observed}^{jet}$.

The results of the correlations between $E_{T\,hadron}^{jet}$ and $E_{T\,observed}^{jet}$ are shown in Fig5.8. In this figure, the correlation has been studied by using jets in the $\gamma\gamma$ collisions with $E_{T\,observed}^{jet} < 9\ GeV$ and in the annihilation events ($e^+e^- \rightarrow q\bar{q}$) with $E_{T\,observed}^{jet} > 9\ GeV$.

E_T^{jet} correlation in annihilation process

We also checked the E_T^{jet} correlation at higher E_T^{jet} region using the $e^+e^- \rightarrow q\bar{q}$ process. Fig.5.6 shows the E_T^{jet} correlation in the $e^+e^- \rightarrow q\bar{q}$ process. At the hadron level, $E_{T\,observed}^{jet}$ distribution has long tail due to the detector resolution. The distributions of $E_{T\,observed}^{jet}$ in each $E_{T\,hadron}^{jet}$ sub-region are shown in Fig.5.7. By using Monte-Carlo simulation, we studied the correlation up to $E_{T\,hadron}^{jet} = 50$ GeV.

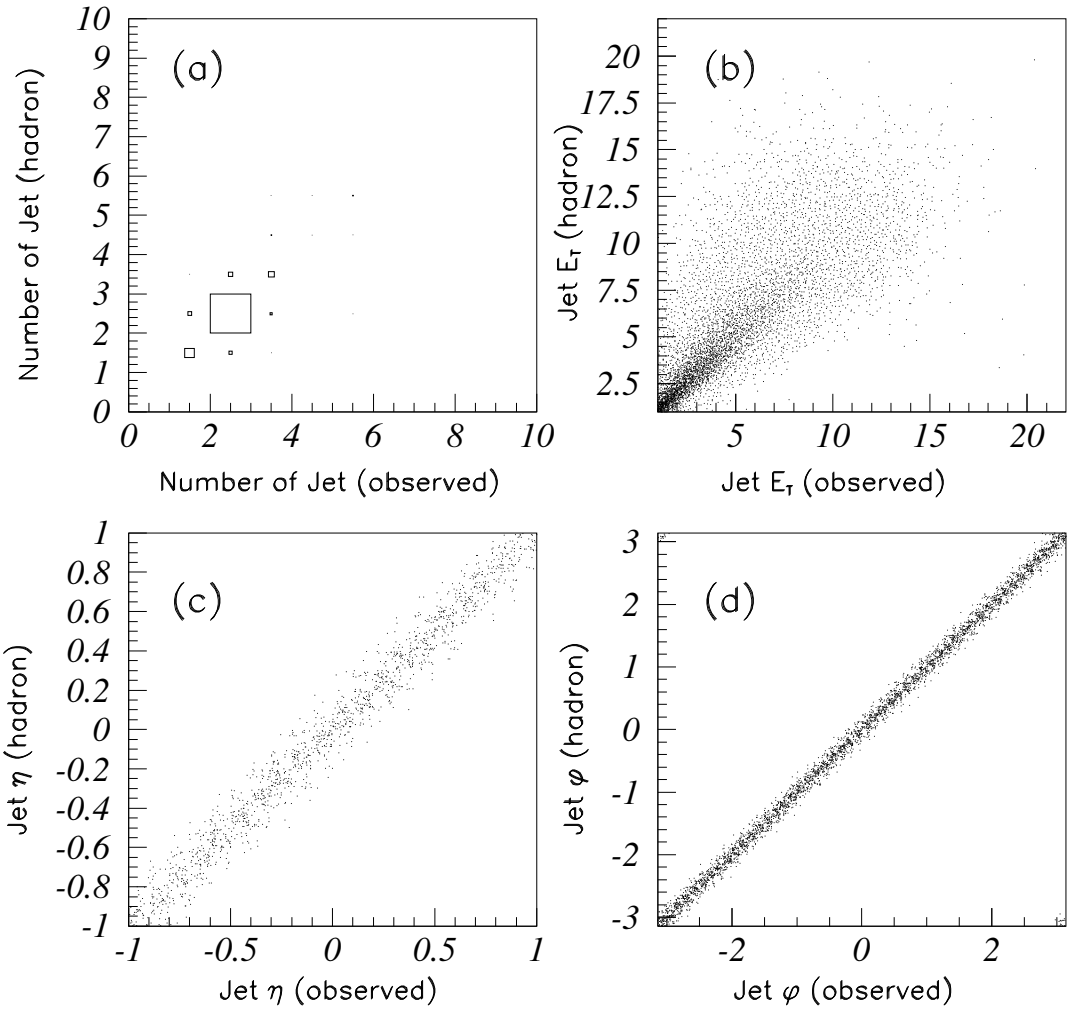

Figure 5.4: Various correlations of jet quantities at hadron level and detector level. (a), (b), (c) and (d) is the number of jet, E_T^{jet}, η^{jet} and ϕ^{jet} correlation, respectively.

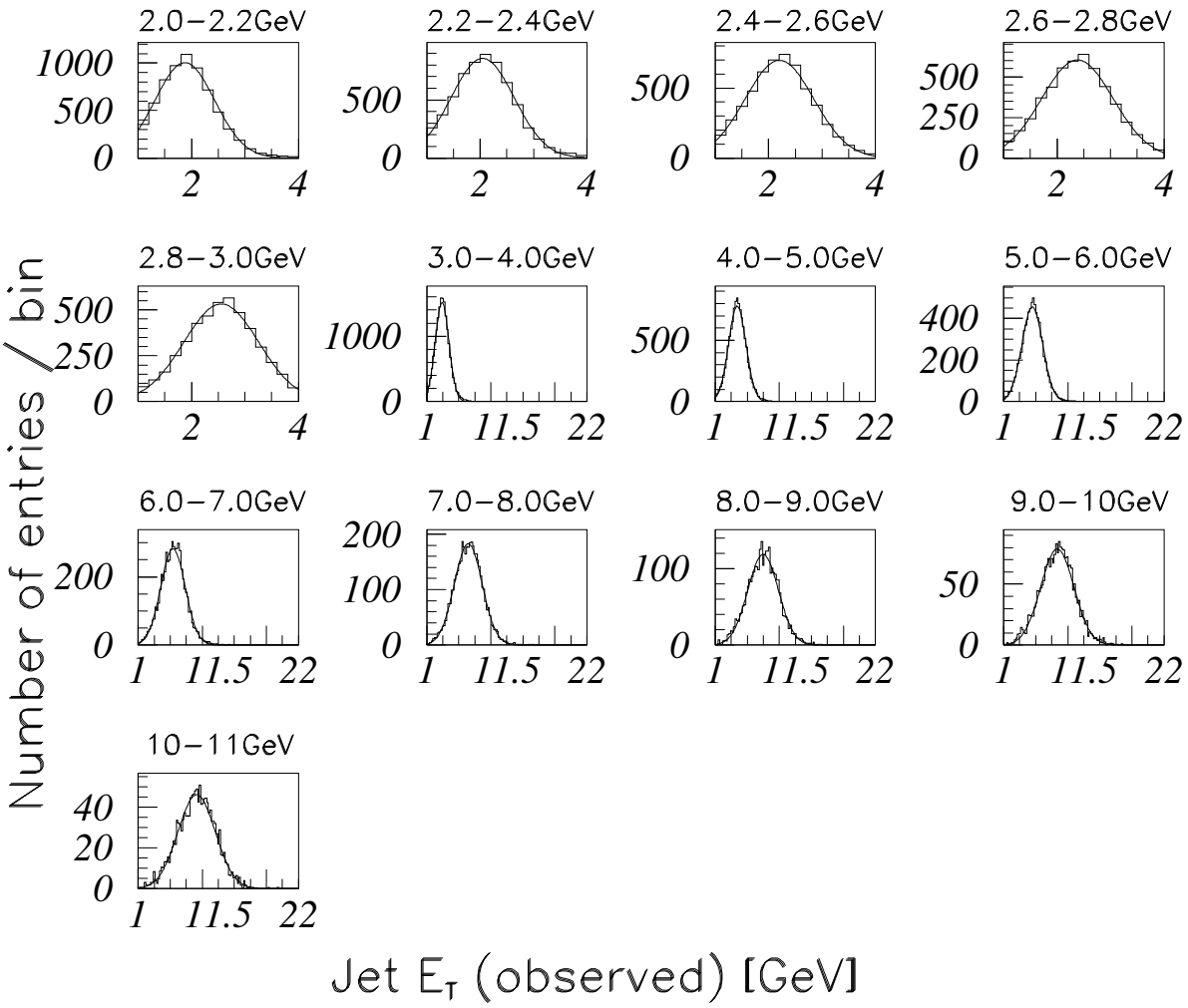

Figure 5.5: $E_{T\,observed}^{jet}$ distribution is fitted by Gaussian function in each $E_{T\,hadron}^{jet}$ sub-region. Notice that below and above 3.0 GeV of $E_{T\,hadron}^{jet}$, the horizontal scale is changed.

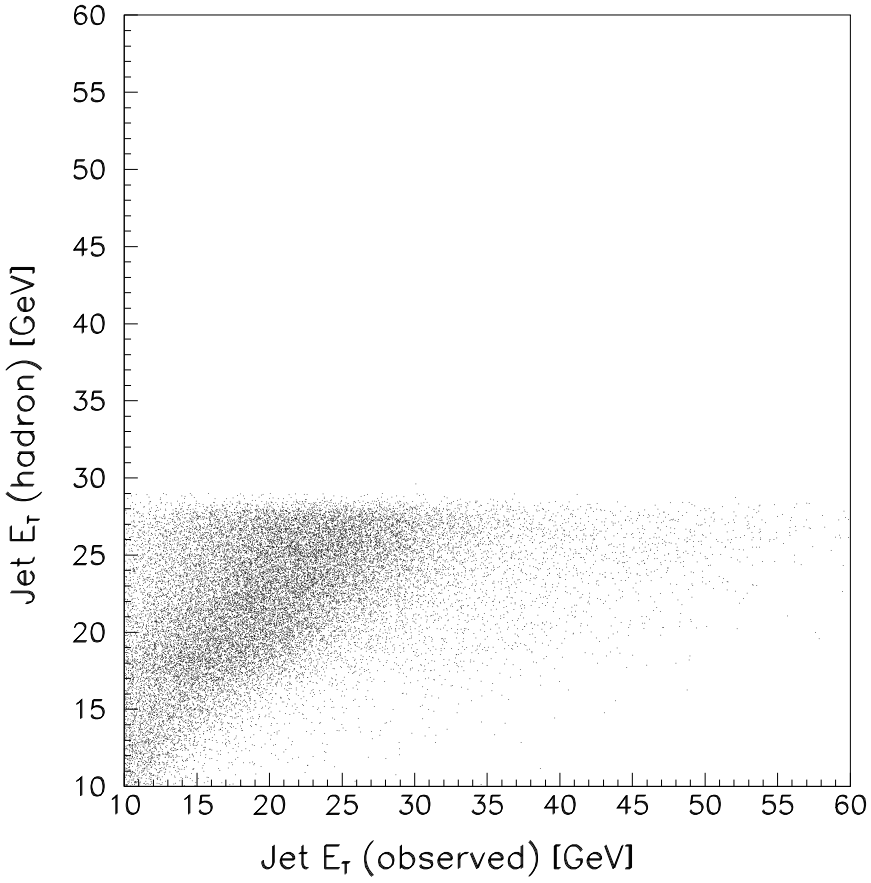

Figure 5.6: The E_T^{jet} correlation in $e^+e^- \rightarrow q\bar{q}$ process ($E_{beam} = 29\ GeV$).

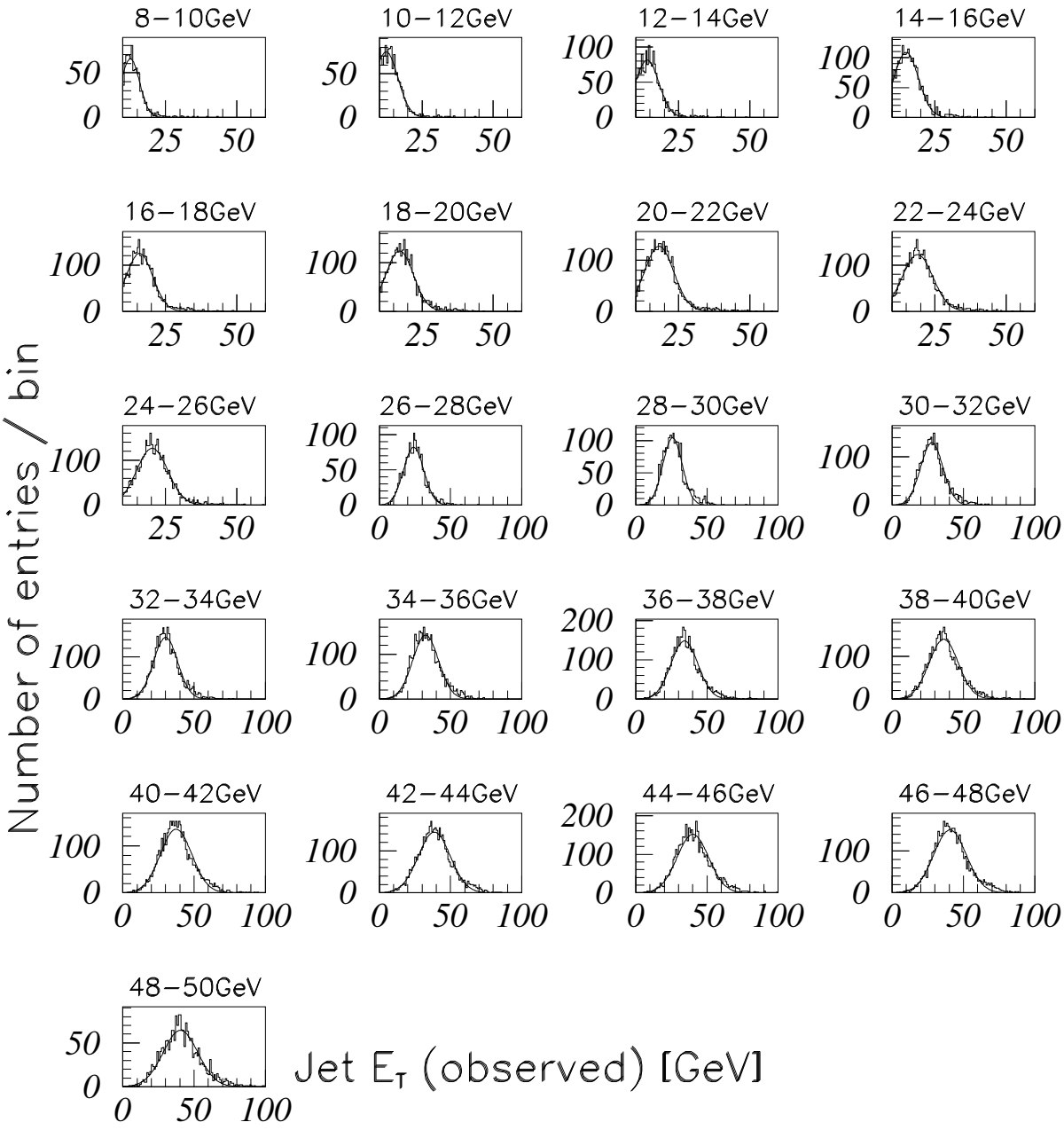

Figure 5.7: $E^{jet}_{T\,observed}$ distribution is fitted by Gaussian function in each $E^{jet}_{T\,hadron}$ sub-region ($e^+e^- \rightarrow qq$ sample). Notice that below and above 26 GeV of $E^{jet}_{T\,hadron}$, the horizontal scale is changed.

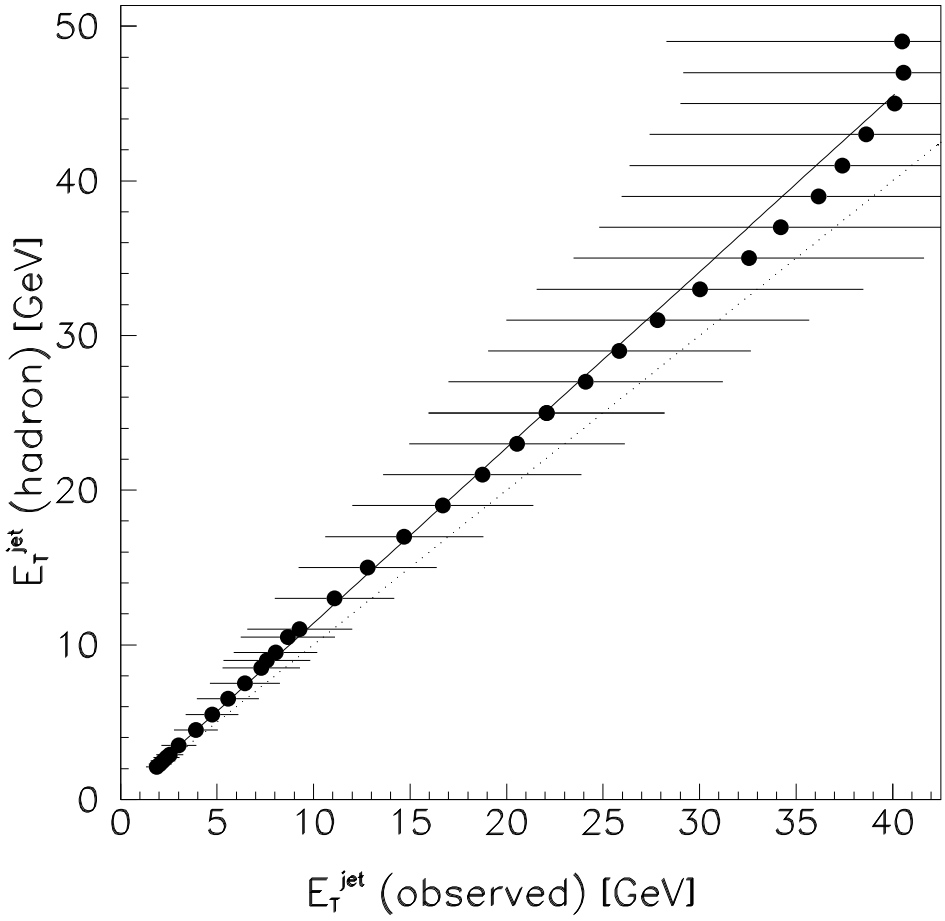

Figure 5.8: The E_T^{jet} correlation between the hadron level and the observed level. The horizontal bars represent the resolution of $E_{T\,observed}^{jet}$. The dotted line corresponds to the case of $E_{T\,hadron}^{jet} = E_{T\,observed}^{jet}$. The solid line is a fit by a linear function.

In Fig.5.8, we fitted the relation of $E_{T\,hadron}^{jet}$ and $E_{T\,observed}^{jet}$ by a linear function. The result is given by

$$E_{T\,hadron}^{jet}(GeV) = 1.136 \times E_{T\,observed}^{jet}(GeV) \; - \; 0.026(GeV). \qquad (5.1)$$

This result means that the correction is about 13% for E_T^{jet}, and is applicable to the jets with 2 $GeV < E_T^{jet}$ 40 GeV, which covers all necessary region for jets in the $\gamma\gamma$ and the annihilation events. Hereafter, jets are corrected according to this function.

5.3.3 Jet and Dijet Event Selection

As described in section 5.1, total 285,941 hadronic two-photon events have been selected. We searched for jets included in those hadronic events by using the cone algorithm explained in 5.3.1 and then, we corrected jet E_T by the procedure described in 5.3.2. As a result, 57,779 (39,829) jets were found with the condition of $E_T^{jet} \geq 2.0\ GeV$ and $|\eta^{jet}| \leq 1.0$ (0.7), respectively as summarized in Table 5.2.

Selection item	Number of jets
$E_T^{jet} \geq 2.0\ GeV$, $\lvert\eta^{jet}\rvert \leq 1.0$	57,779
$E_T^{jet} \geq 2.0\ GeV$, $\lvert\eta^{jet}\rvert \leq 0.7$	39,829

Table 5.2: The number of jets in $\gamma\gamma$ collision at each selection cut.

The dijet event is then selected by taking a event with two or more jets with fulfilling the highest E_T^{jet} is greater than 3.0 GeV and the second highest E_T^{jet} is greater than 2.0 GeV. Here, the highest E_T jet is named "the first jet" and its quantities are denoted as E_T^{jet1}, η^{jet1} and ϕ^{jet1} for convenience. Similarly, the second highest E_T jet is named "the second jet" and its quantities are denoted as E_T^{jet2}, η^{jet2} and ϕ^{jet2}. The threshold of $E_{T\,cut}^{jet1}$ is set not equal to that of $E_{T\,cut}^{jet2}$ in order to avoid a theoretical difficulty to calculate a higher order cross section near threshold region [65]. On the pseudo-rapidity condition, we basically chose loose cut when investigating distributions concerning with η. The number of dijet events with condition of $|\eta^{jet1,jet2}| \leq 1.0$ (0.7) is 6,999 (3,582), respectively as summarized in Table 5.3.

For the e^+e^-annihilation events, among 29,184 hadronic annihilation events, number of jets and dijet events are obtained by the same way. Number of jets

Selection item	Number of dijet events
$E_T^{jet1} \geq 3.0\ GeV$, $E_T^{jet2} \geq 2.0\ GeV$, $\lvert\eta^{jet1,jet2}\rvert \leq 1.0$	6,999
$E_T^{jet1} \geq 3.0\ GeV$, $E_T^{jet2} \geq 2.0\ GeV$, $\lvert\eta^{jet1,jet2}\rvert \leq 0.7$	3,582

Table 5.3: The number of dijet event in $\gamma\gamma$ collision at each selection cut.

and dijet events with each conditions of E_T^{jet} and η^{jet} are summarized in Table 5.4 and Table 5.5.

Selection item	Number of jets
$E_T^{jet} \geq 2.0\ GeV$, $\lvert\eta^{jet}\rvert \leq 1.0$	65,261
$E_T^{jet} \geq 2.0\ GeV$, $\lvert\eta^{jet}\rvert \leq 0.7$	50,319

Table 5.4: The number of jets in e^+e^-annihilation event at each selection cut.

Selection item	Number of dijet events
$E_T^{jet1} \geq 3.0\ GeV$, $E_T^{jet2} \geq 2.0\ GeV$, $\lvert\eta^{jet1,jet2}\rvert \leq 1.0$	27,918
$E_T^{jet1} \geq 3.0\ GeV$, $E_T^{jet2} \geq 2.0\ GeV$, $\lvert\eta^{jet1,jet2}\rvert \leq 0.7$	20,982

Table 5.5: The number of dijet events in e^+e^-annihilation event at each selection cut.

5.4 Background Estimation

The backgrounds contained in these sample come from various sources. Beam-gas backgrounds are estimated from data, and the other physical backgrounds are estimated by using Monte-Carlo simulation.

Since the beam-gas events are expected to be produced at all regions on the beam-line, they are estimated from the events located in the side band of Z_{vertex} distribution (double hatched area in Fig.5.1).

The contributions from the e^+e^-annihilation ($ee \to q\bar{q}(\gamma)$, $ee \to \tau\tau(\gamma)$) was estimated with the PYTHIA Monte-Carlo program. We also used the KORALZ 3.8 program code [66]. Both generator programs deal with initial state radiation

and give similar results for the $ee \to q\bar{q}(\gamma)$ process. The annihilation backgrounds dominate at higher E_T region above 10 GeV. The contributions from the lepton production in the two-photon process ($ee \to ee\tau\tau$, $ee \to eeee$) is calculated with PYTHIA.

Table.5.6, Table.5.7, Table.5.8 and Table.5.9 summarize the contributions from each background source for inclusive jet with $|\eta^{jet}| < 1.0$ and $|\eta^{jet}| < 0.7$, for dijet events with $|\eta^{jet1,jet2}| < 1.0$ and $|\eta^{jet1,jet2}| < 0.7$, respectively. The contamination from each background process is calculated as $\frac{N_{background}}{N_{data}}$, where $N_{background}$ stands for the number of dijet events from each background source and N_{data} is the total number of jets or dijet events. For the dijet events, the main backgrounds come from the e^+e^-annihilation process ($ee \to q\bar{q}(\gamma)$), and is $20\% \sim 25\%$. Other backgrounds are negligible. Hereafter, we subtracted these contributions from the data bin-by-bin bases in each histogram.

Background process	contamination	method/program name
Beamgas event	15.3 %	sideband of Z_{vertex}
$ee \to q\bar{q}(\gamma)$	11.7 and 11.1 %	KORALZ and PYTHIA
$ee \to \tau\tau(\gamma)$	0.20 %	PYTHIA
$ee \to ee\tau\tau$	1.11 %	PYTHIA
$ee \to eeee$	0.31 %	PYTHIA

Table 5.6: The background contribution to inclusive jet event (%). $E_T^{jet} \geq 2\ GeV$ and pseudo-rapidity condition is $|\eta^{jet}| \leq 1.0$.

Background process	contamination	method/program name
Beamgas event	11.2 %	sideband of Z_{vertex}
$ee \to q\bar{q}(\gamma)$	10.1 and 9.54 %	KORALZ and PYTHIA
$ee \to \tau\tau(\gamma)$	0.19 %	PYTHIA
$ee \to ee\tau\tau$	1.21 %	PYTHIA
$ee \to eeee$	0.28 %	PYTHIA

Table 5.7: The background contribution to inclusive jet event (%). $E_T^{jet} \geq 2\ GeV$ and pseudo-rapidity condition is $|\eta^{jet}| \leq 0.7$.

Background process	contamination	method/program name
Beamgas event	1.06 %	sideband of Z_{vertex}
$ee \to q\bar{q}(\gamma)$	26.9 and 25.0 %	KORALZ and PYTHIA
$ee \to \tau\tau(\gamma)$	0.68 %	PYTHIA
$ee \to ee\tau\tau$	2.50 %	PYTHIA
$ee \to eeee$	1.04 %	PYTHIA

Table 5.8: The background contribution to dijet event (%). $E_T^{jet1} \geq 3\ GeV$, $E_T^{jet2} \geq 2\ GeV$ and pseudo-rapidity condition is $|\eta^{jet1}| \leq 1.0$ and $|\eta^{jet2}| \leq 1.0$.

Background process	contamination	method/program name
Beamgas event	0.70 %	sideband of Z_{vertex}
$ee \to q\bar{q}(\gamma)$	19.6 and 18.4 %	KORALZ and PYTHIA
$ee \to \tau\tau(\gamma)$	0.61 %	PYTHIA
$ee \to ee\tau\tau$	2.48 %	PYTHIA
$ee \to eeee$	0.86 %	PYTHIA

Table 5.9: The background contribution to dijet event (%). The conditions of E_T^{jet} are same as the Table. 5.8. Pseudo-rapidity condition is $|\eta^{jet1}| \leq 0.7$ and $|\eta^{jet2}| \leq 0.7$.

Chapter 6

General Properties of Dijet Event

In this chapter, we study various properties of dijet events which were selected in the previous section. Dijet event, which has at least two high E_T jets, is the most fundamental event in $\gamma\gamma$ collisions. In the dijet sample, since both jets are measured, we can reconstruct the parton momentum fraction (x_γ) by using observables of jet. This observables provide a useful tool to study event properties by separating the event sample from direct and resolved processes. With the opening angle distribution of dijet events, we observed the higher order QCD effect and evaluated the parton transverse momentum distribution inside a photon.

6.1 x_γ Reconstruction from observables

As described in the previous section, 6,999 events has been selected as the dijet sample with the conditions $E_T^{jet1} \geq 3.0\ GeV$ and $E_T^{jet2} \geq 2.0\ GeV$. The pseudo-rapidities of the both jets, $|\eta^{jet1}|$ and $|\eta^{jet2}|$ are required to be less than 1.0. In this analysis, we use the transverse energy of the first jet E_T^{jet1} as the typical transverse energy of a dijet event.

Especially, events which have two jets in it offer the possibility to differentiate between direct and resolved interactions. A pair of variables, x_γ^+ and x_γ^- can be defined as a measure of the momentum fraction of the parton inside the photon in the hard interaction [67].

$$x_\gamma^{\mp} = \frac{\sum_j^{jet}(E \pm P_Z)_j}{\sum_i^{hadron}(E \pm P_Z)_i} \quad , \tag{6.1}$$

where, P_Z is the momentum component along the Z-axis of the detector and E is the energy of each particle. The numerator of Eq.(6.1) is the sum for particles within the jet cone while the denominator is the sum for all particles in a dijet event. At conventional TOPAZ coordinate, the direction of electron-beam is defined as positive direction of Z-axis. Thus x_γ^- indicates the parton momentum fraction in the photon radiated from the electron, while x_γ^+ is that from positron. The scatter plot of x_γ^- and x_γ^+ for the dijet sample is shown in Fig.6.1. A clear concentration is seen in the vicinity of 1.0 for both x_γ^- and x_γ^+ observables. This area corresponds to the sample from direct process.

In order to examine the data quantitatively, we introduce a variable x_γ^{min}, which is defined as a smaller value of x_γ^- and x_γ^+ as ;

$$x_\gamma^{min} \equiv Min\{x_\gamma^- \ , \ x_\gamma^+\} \ .$$

x_γ^{min} distribution for the same sample is shown in Fig.6.2 and is compared with the PYTHIA Monte-Carlo expectations. As shown in this figure, a clear peak

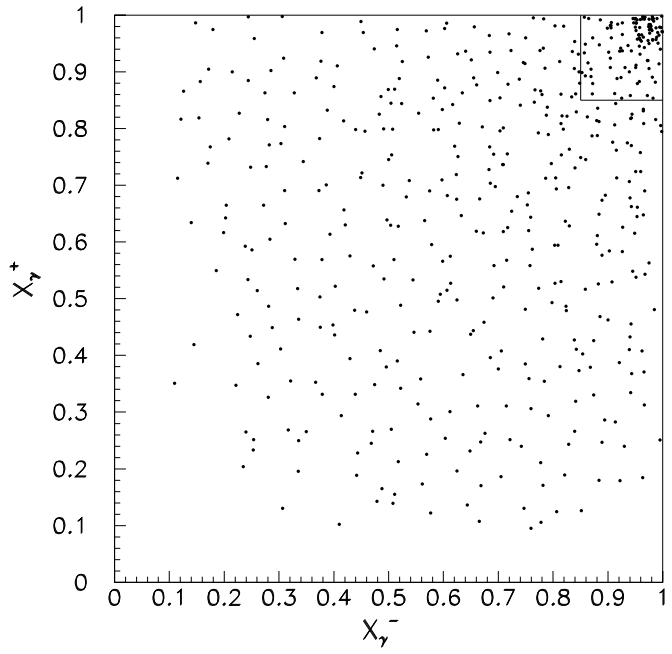

Figure 6.1: The correlation of x_γ^- and x_γ^+. Dots are the data.

in the vicinity of $x_\gamma^{min} \sim 1$ can well be explained from the direct component in the PYTHIA Monte-Carlo. Also at the region around $0.2 \leq x_\gamma^{min} \leq 0.8$, the experimental distribution is reproduced by the resolved component. The overall

shape as well as its magnitude are well explained by the PYTHIA Monte-Carlo prediction with GRV-LO photon structure function, though for the region around $0.2 \leq x_\gamma^{min} \leq 0.6$ the PYTHIA prediction are about 20% higher than the data.

In order to study the quantitative difference of the direct and resolved process with other observables, we separate the sample of direct-enriched and resolved-enriched sample at $x_\gamma^{min} = 0.85$. We call the events in $x_\gamma^{min} > 0.85$ as "direct-sample" and the one in $x_\gamma^{min} < 0.85$ as "resolved-sample". According to the PYTHIA Monte-Carlo simulation, about 67% of the events from the direct process are contained in $x_\gamma^{min} > 0.85$ region, while about 90% of the events from the resolved process are contained in $x_\gamma^{min} < 0.85$ region. Purities of the direct-sample and the resolved-sample are 70% and 89%, respectively. These values are summarized in Table 6.1.

	Direct-sample	Resolved-sample
Acceptance	67 %	90 %
Purity	70 %	89 %

Table 6.1: The acceptance and purity for each sample. (%).

6.2 Differences between direct and resolved processes

The most conspicuous difference between the direct process and the resolved process is the existence of the remnant-jet in the resolved process. We study the difference between the direct-sample and the resolved-sample for dijet events by using following observables ; transverse energy of jet ($\frac{dN}{dE_T^{jet}}$), transverse energy flows with respected to the jet axis ($\frac{1}{N}\frac{dE_T}{d\Delta\eta}$, $\frac{1}{N}\frac{dE_T}{d\Delta\phi}$) and opening angle between two jets ($\Delta\phi_{jj}$). The results are shown in Figs.6.3, Figs.6.5, Figs.6.6 and Figs6.7. In these figures, (a) and (b) are for $x_\gamma^{min} > 0.85$ and $x_\gamma^{min} < 0.85$ sample, respectively.

6.2.1 Transverse Energy of Jet Distribution

Figs.6.3 show the E_T^{jet} distributions. Here, E_T^{jet} represents the highest E_T^{jet} of dijet event and the jets are imposed with a condition of $|\eta^{jet}| < 0.7$. In this figure, only E_T^{jet} are corrected by the procedure described in 5.3.2. These distribution

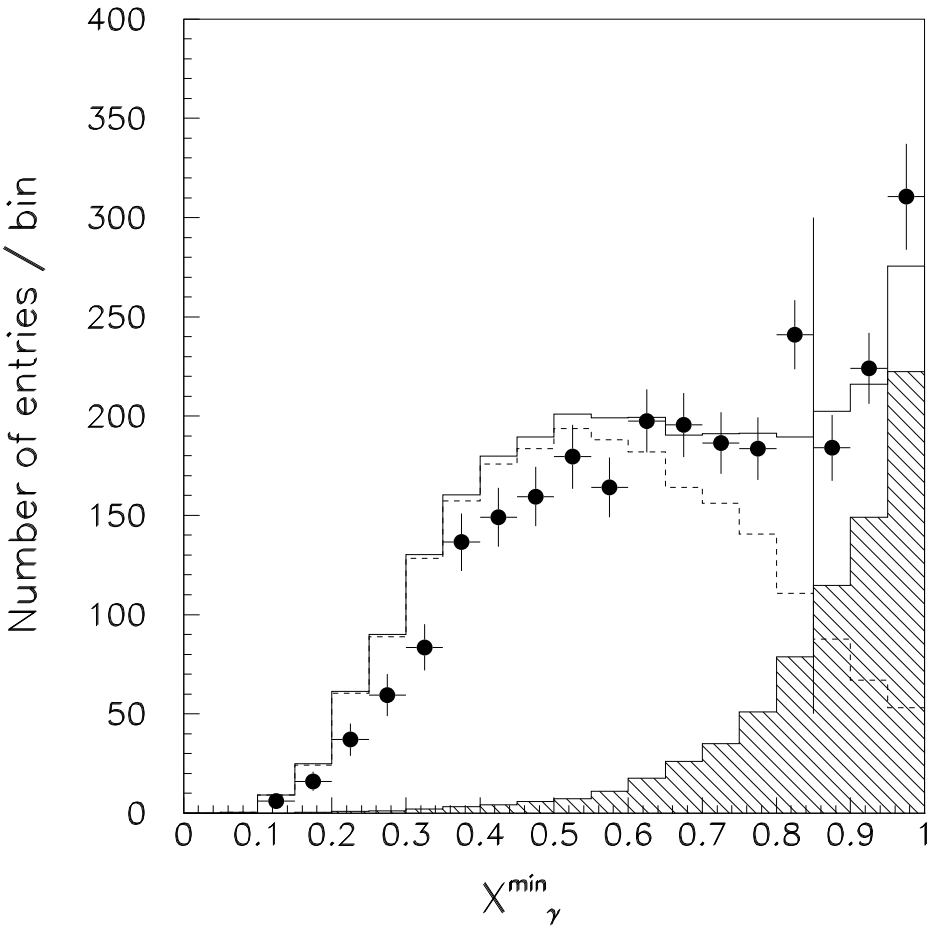

Figure 6.2: x_γ^{min} distribution for dijet events. Points with Error bars are data. Histograms are PYTHIA predictions with GRV-LO photon structure function. The hatched histogram is the contribution from direct process, and the dashed histogram is that from resolved process. The solid histogram is the sum of both processes.

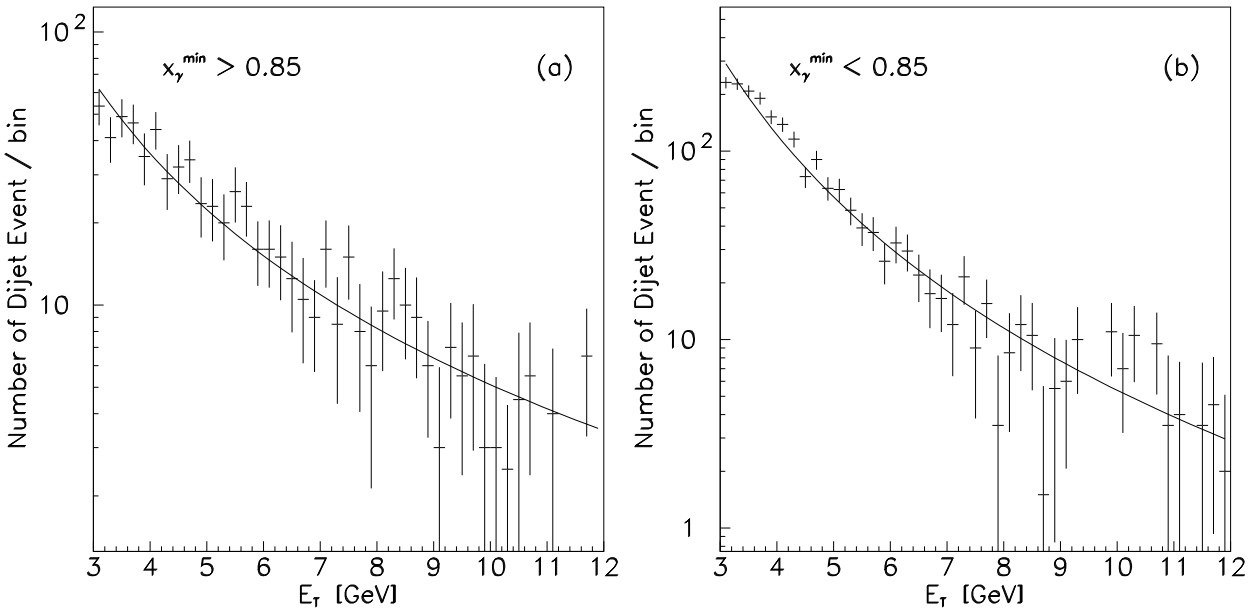

Figure 6.3: E_T^{jet} distributions for the data. The solid curves are fitting results using the formula (6.2). (a) is $x_\gamma^{min} > 0.85$ and (b) is $x_\gamma^{min} < 0.85$.

are expressed as

$$\frac{dN}{dE_T} \propto E_T^{-n}. \tag{6.2}$$

The fit with the form of Eq.(6.2) results $n = 2.13 \pm 0.10$ for the direct-sample ($x_\gamma^{min} > 0.85$) and $n = 3.41 \pm 0.07$ for the resolved-sample ($x_\gamma^{min} < 0.85$). The incline of distribution of resolved-sample is steeper than that of the direct-sample. Since all energies of the two photons can be used for hard scattering in the direct process, the transverse energy of the jet is relatively high. On the other hand, for the resolved process, only a part of photon energy contributes to the hard scattering. Thus E_T^{jet} of the resolved process is relatively lower and its distribution decreases rapidly as E_T^{jet} increases.

6.2.2 Transverse Energy Flow Distribution

The transverse energy flows with respected to the jet axis averaged over all related jets are shown as functions of $\Delta\eta$ and $\Delta\phi$ in Fig.6.5 and Fig.6.6, respectively.

Transverse Energy Flow Distribution against $\Delta\eta$

$\Delta\eta$ is the pseudo-rapidity difference of the particles with respect to the jet direction.

$$\Delta\eta \equiv k \cdot (\eta^{particle} - \eta^{jet}), \tag{6.3}$$

Here we introduced a factor $k = \pm 1$ for $\Delta\eta$ definition. The factor k is chosen to be $k = +1$ for the events with $x_\gamma^- > x_\gamma^+$ and $k = -1$ for the events with $x_\gamma^- < x_\gamma^+$. As illustrated in Fig.6.4, due to the choice of k, there is always more energy flow at $\Delta\eta < 0$ region where activity from remnant-jet are expected.

We used both jets with their pseudo-rapidities $|\eta^{jet1}|$ and $|\eta^{jet2}|$ to be less than 1.0 in the dijet sample, and each particle is assigned to the nearest jet (*i.e.* $|\phi^{particle} - \phi^{jet}| \leq \pi/2$). Figs.6.5 show the $\frac{1}{N}\frac{dE_T}{d\Delta\eta}$ distribution. For the direct-sample ($x_\gamma^{min} > 0.85$), the distribution is almost symmetric, while for the resolved-sample ($x_\gamma^{min} < 0.85$), enhanced energy flows are seen at $\Delta\eta < 0$ region, implying the contribution from the remnant-jet. The PYTHIA Monte-Carlo prediction can reproduce the data well.

Transverse Energy Flow Distribution against $\Delta\phi$

$\Delta\phi$ is defined as the azimuthal angle difference of the particles with respect to the jet direction.

$$\Delta\phi \equiv \phi^{particle} - \phi^{jet}. \tag{6.4}$$

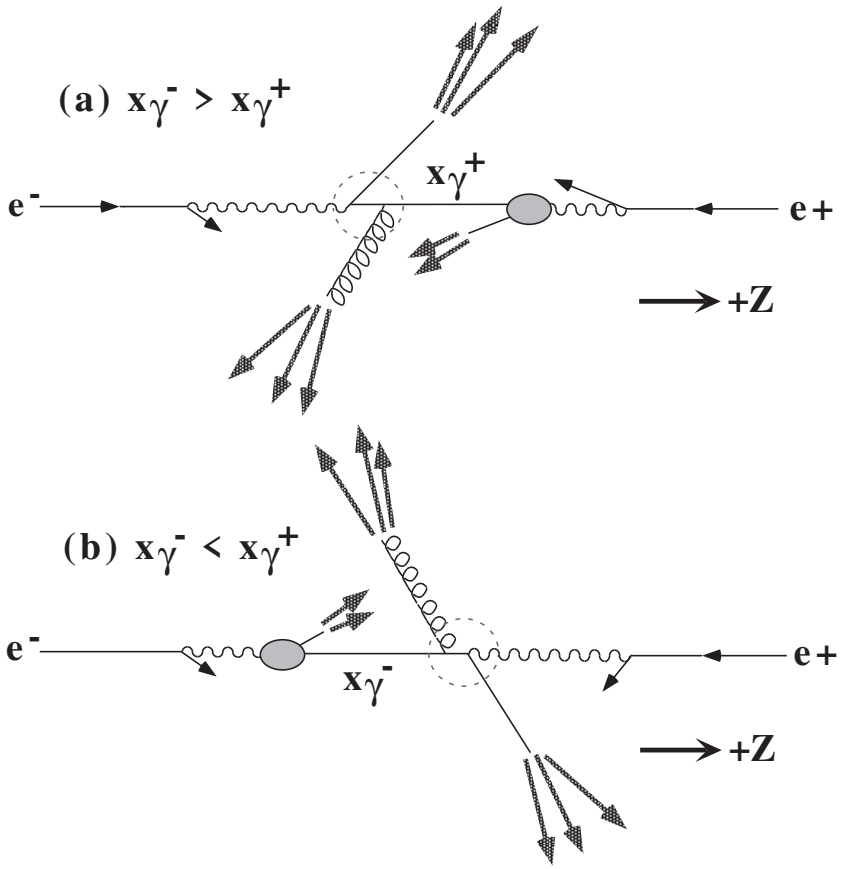

Figure 6.4: Two cases for choosing factor k. (a) is for $k = +1$ and (b) is for $k = -1$.

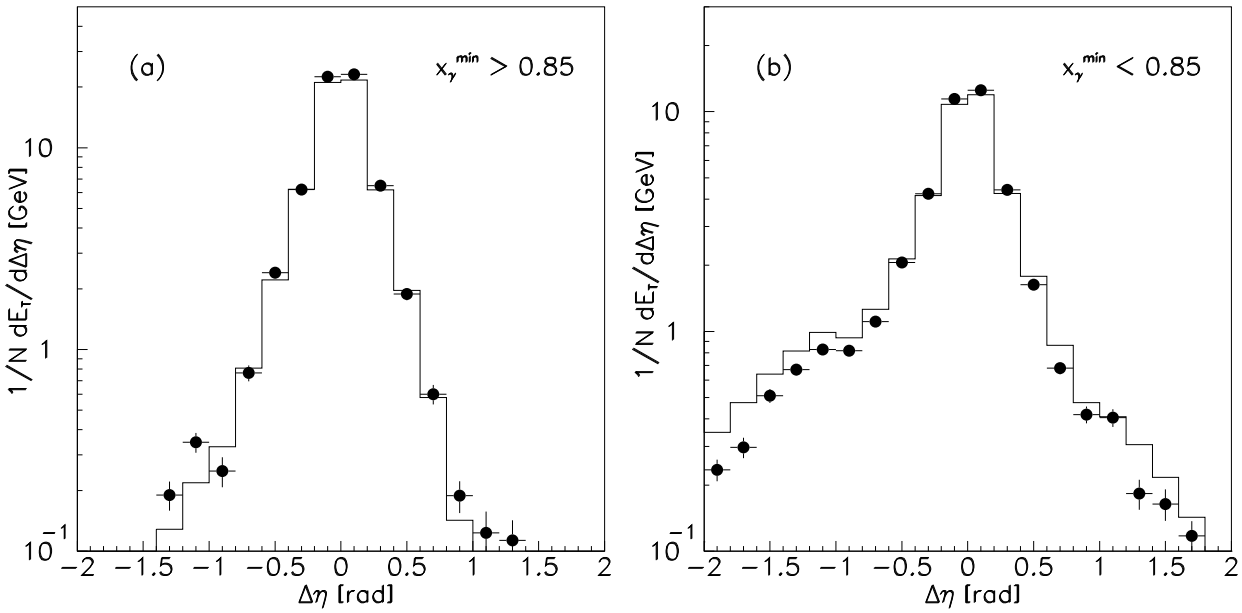

Figure 6.5: The transverse energy flows with respected to the jet axis as a function of the rapidity difference. The points with the error bars are the data. The histogram is Monte-Carlo prediction from PYTHIA with GRV-LO photon structure function. (a) is $x_\gamma^{min} > 0.85$ and (b) is $x_\gamma^{min} < 0.85$.

In the study of the $\frac{1}{N}\frac{dE_T}{\Delta\phi}$ distribution, two jets with their pseudo-rapidities $|\eta^{jet1}|$ and $|\eta^{jet2}|$ are limited to be less than 0.7 and the pseudo-rapidity of each particle is limited within 1.0 region. Figs.6.6 represent the transverse energy flows as a function of $\Delta\phi$ as an example in the range of $3.0\ GeV < E_T^{jet} < 4.0\ GeV$. In both figures of (a) and (b), the energy concentrates within $|\Delta\phi| < 1.0$. Another peaks at around $|\Delta\phi| \sim \pi$ correspond to the activity from other jets. For the direct-sample ($x_\gamma^{min} > 0.85$), energy flows from two jets are clearly separated, while for the resolved-sample ($x_\gamma^{min} < 0.85$) activities in the middle region between two jet are seen. The PYTHIA Monte-Carlo prediction reproduces the data reasonably well.

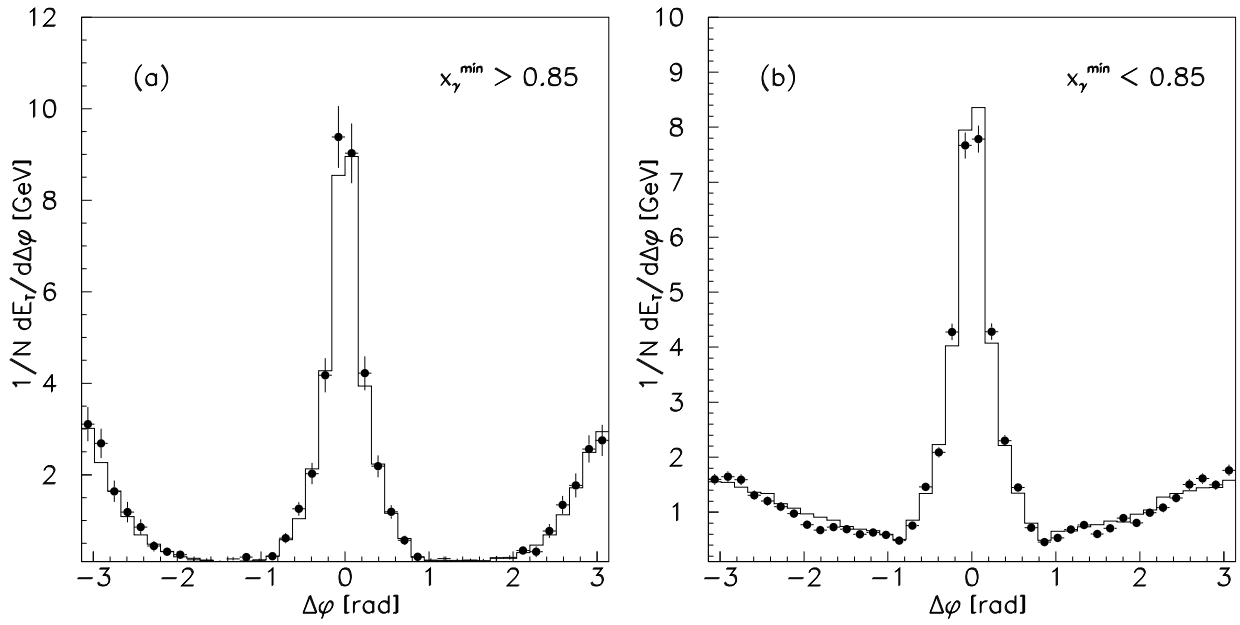

Figure 6.6: The transverse energy flows with respected to the jet axis as a function of the azimuthal angle difference. The points with the error bars are the data. The histogram is Monte-Carlo prediction from PYTHIA with GRV-LO photon structure function. (a) is $x_\gamma^{min} > 0.85$ and (b) is $x_\gamma^{min} < 0.85$.

6.2.3 Opening Angle between Dijet

The opening angle between the first jet and the second jet $\Delta\phi_{jj}$ is defined as the azimuthal angle difference ;

$$\Delta\phi_{jj} \equiv |\phi^{jet1} - \phi^{jet2}|.$$

Figs.6.7 show the $\Delta\phi_{jj}$ distribution. Here we limited the dijet sample with $|\eta^{jet1}| < 0.7$ and $|\eta^{jet2}| < 0.7$. For the direct-sample ($x_\gamma^{min} > 0.85$), almost of all dijet events have back-to-back two jets and distribution decreases rapidly as $\Delta\phi_{jj}$ decreases. On the contrary, for the resolved-sample ($x_\gamma^{min} < 0.85$), $\Delta\phi_{jj}$ distribution is more broader than that for the direct-sample.

In Leading-Order of the dijet production, the difference of azimuthal angle between the first jet and the second jet ($\Delta\phi_{jj}$) is ideally π *radian*. However in practice, the difference is not π *radian* because of the following reasons described in section 2.6 ; (1) detector resolution, (2) virtuality of a photon, (3) QCD initial state radiations at hard sub-process and (4) primordial transverse momentum (k_T) of parton inside a photon. The QCD initial state radiation and the definition of k_T are illustrated in Fig.2.8 and Fig.2.9, respectively. For the direct process, the reasons of (1) and (2) smear the $\Delta\phi_{jj}$ distribution from back-to-back configuration, while for the resolved process, all above effects contribute to the distribution.

In order to study these effects more quantitatively, we simulated various Monte-Carlo events by changing the condition of the QCD initial state radiations as well as the primordial k_T distribution of the parton inside a photon. k_T is defined as the transverse momentum of the remnant-jet with respect to the original photon direction. The experimental shape of the k_T distribution is not known at present.

Theoretically, there are two typical k_T distributions : one is the Gaussian type given in Eq.(6.5) and the other is the power-law type given in Eq.(6.6). It is expected that these two different distributions come from the different components of a quasi-real photon. As described in section 2.6, there might be two different kinds of $q\bar{q}$ state in the fluctuation from the photon (Fig.2.5). One is the VDM state where $q\bar{q}$ makes a bound state like usual hadrons, and the other is the anomalous state where $q\bar{q}$ is loosely bounded and those state can be calculable by a perturbative QCD.

If the photon fluctuates as the VDM state, the k_T distribution is expected to be the Gaussian type. On the other hand, when the photon fluctuates as the anomalous state, the k_T distribution behaves like power-law. We set the

parameters σ and k_T^0 to be 0.44 GeV/c and 0.66 GeV/c [68], respectively.

$$\frac{dN}{dk_T} \propto exp(-\frac{k_T^2}{2\sigma^2}) \tag{6.5}$$

$$\frac{dN}{dk_T} \propto \frac{1}{k_T^2 + (k_T^0)^2} \tag{6.6}$$

In Fig.6.7(b), the effect of the QCD-initial state radiation (ISR) can be seen by comparing the dashed line (ISR-on) with the dotted line (ISR-off). These two lines represent the Gaussian k_T assumption. At the region of $\Delta\phi_{jj} < 2.7$ $radian$, the number of the ISR-off event is less than that of the ISR-on and fails to reproduce the data.

The effect of k_T behavior can be checked by comparing the solid line (power-law k_T) with the dashed line (Gaussian k_T). Both of these two lines are ISR-on. The power-law k_T distribution creates more longer tail in lower $\Delta\phi_{jj}$ region. The data distribute between two lines at $\Delta\phi_{jj} < 2.5$ $radian$. However, at $\Delta\phi_{jj} > 2.5$ $radian$, it seems that power-law k_T is more consistent the the data. From this observation, photon is found to behave as the anomalous state predominanlty. That is, in the TRISTAN energy region, the $q\bar{q}$ pair fluctuated from photon is bounded more loosely rather than makes a hadron.

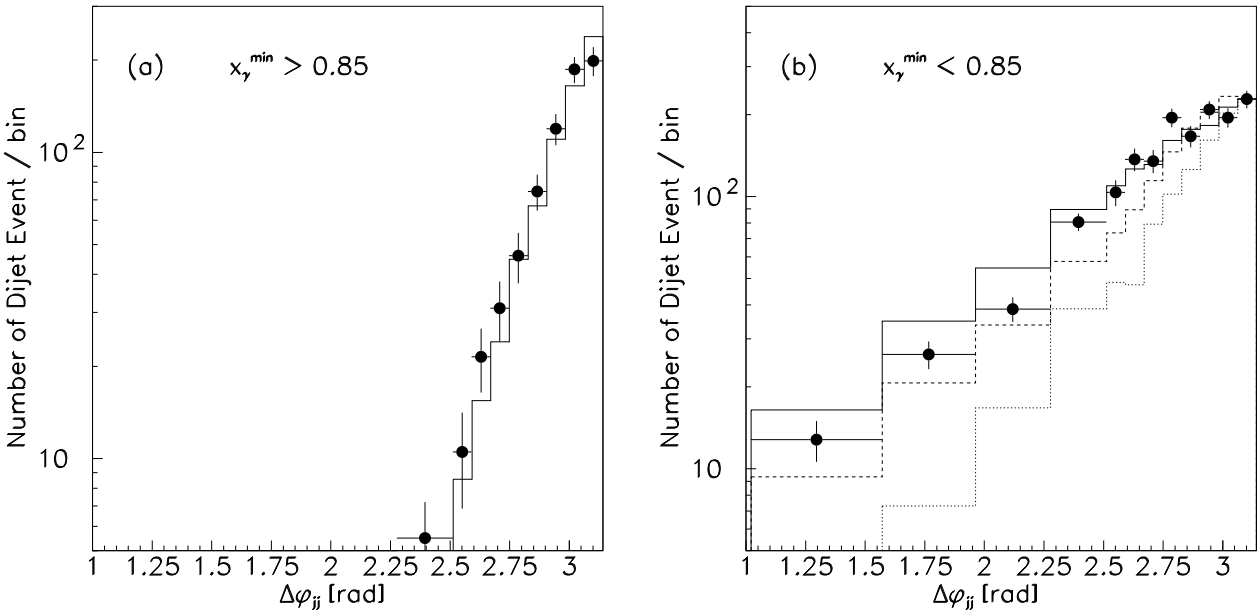

Figure 6.7: $\Delta\phi_{jj}$ distributions. (a) is $x_\gamma^{min} > 0.85$ and (b) is $x_\gamma^{min} < 0.85$. The points with the error bars are the data. The histogram at (a) is Monte-Carlo prediction from PYTHIA with GRV-LO photon structure function. In (b), the histograms are several Monte-Carlo predictions ; the solid line is with an initial state radiation and power-law k_T, the dashed line is with an initial state radiation and Gaussian k_T, and the dotted line is without an initial state radiation and Gaussian k_T. All histograms are normalized at rightmost bin.

Chapter 7

Jet Profile

Jet, a collimated hadron flow, is an universal phenomena in many kind of high energy reactions which contain hadrons in the final states. Clear jets can be seen in the final state in $p\bar{p}$ collider at TEVATRON and also e^+e^-annihilation processes at TRISTAN as well as at LEP. Recently the observation of jets are also reported in deep-inelastic ep collision as well as photoproduction process (γp) at HERA ep collider. In this chapter, we study the jet profile produced in $\gamma\gamma$ collision at TRISTAN e^+e^-collider. The jet width has been measured as a function of jet E_T and were compared them with that of jet from other reactions, including the e^+e^-annihilation events observed with the same TOPAZ detector. This is the first observation of the jet width for $\gamma\gamma$ collisions in the world.

7.1 Definition of Jet Width

In order to represent overall feature of the hadronic events or the profile of jets within an event, several kinds of shape variables have been proposed and been used in the analysis of high energy reactions. In this analysis, to compare the jet profile directly with different reactions , we use a simple quantity of jet width as a measure of the broadness of jets. The jet width is defined as the full width at half maximum in the distribution of the transverse energy flow with respect to the jet axis, as a function of azimuthal angle difference, $\Delta\phi$. The jet axis is determined by the cone algorithm and $\Delta\phi$ is defined in Eq.(6.4).

To measure a jet width of its core part, the transverse energy flow as a function of $\Delta\phi$ is chosen rather than the pseudo-rapidity difference $\Delta\eta$, which is defined in Eq.(6.3). Because for the latter case, there are non-negligible contribution from the remnant-jet as shown in Figs.6.5. In order to determine the jet width Γ from

the $\frac{1}{N}\frac{dE_T}{d\Delta\phi}$ distribution, we fitted the distribution with the same fitting function used in the H1 experiment [35].

$$f(\Delta\phi) = A \cdot exp\{-(\sqrt{|\Delta\phi + D|} + B)^4 + B^4\} + C, \tag{7.1}$$

where, A, B, C and D are free parameters. The parameter A represents the overall normalization factor and B is the parameter related to the jet width and C is a height of the base-line of the distribution. The parameter D is used to cancel the binning effects [35]. The jet width Γ can be obtained from the parameter B as

$$\Gamma = 2\{(ln2 + B^4)^{1/4} - B\}^2.$$

The transverse energy flow $\frac{1}{N}\frac{dE_T}{d\Delta\phi}$ for inclusive jet sample in $\gamma\gamma$ collisions are shown in Fig.7.1 for several E_T^{jet} ranges from 2.0 GeV to 9.5 GeV. Here the direction of the jet is limited to $|\eta^{jet}| < 0.7$ and only particles with $|\eta^{particle}| < 1.0$ are used for the calculation of the transverse energy flow $\frac{1}{N}\frac{dE_T}{d\Delta\phi}$. Notice that the range of $\Delta\phi$ is narrower than that in Figs.6.6 and only its cone part is shown. The same distributions of several E_T^{jet} ranges for dijet sample in $\gamma\gamma$ collisions are shown in Fig.7.2. Here the same cut of $|\eta^{jet1}| < 0.7$, $|\eta^{jet2}| < 0.7$ and $|\eta^{particle}| < 1.0$ are imposed. Each bin size of jet E_T was determined in consideration of the detector resolution as follows ;

$$\begin{aligned} 3.0 \leq \ & E_T^{jet} \ \leq 4.0\ GeV \\ 4.0 \leq \ & E_T^{jet} \ \leq 5.5\ GeV \\ 5.5 \leq \ & E_T^{jet} \ \leq 7.5\ GeV \\ 7.5 \leq \ & E_T^{jet} \ \leq 9.5\ GeV \end{aligned}$$

We also reconstructed jets in the e^+e^-annihilation events. The criteria on the event selection for the e^+e^-annihilation are already described in section 5.2. For the e^+e^-annihilation events, we applied the same cone algorithm to identify the jet and made a correction of E_T^{jet} to convert them to the value at the hadron level. E_T^{jet} regions were as follows ;

$$\begin{aligned} 10 \leq \ & E_T^{jet} \ \leq 15\ GeV \\ 15 \leq \ & E_T^{jet} \ \leq 40\ GeV \end{aligned}$$

The same transverse energy flow for the e^+e^-annihilation events are shown in Figs.7.3 and Figs.7.4 for inclusive jet sample and dijet sample, respectively.

The number of jets and the number of dijet events in each E_T^{jet} region are summarized in Table.7.1. In the highest E_T^{jet} region, the event sample of inclusive jet and dijet events are almost identical.

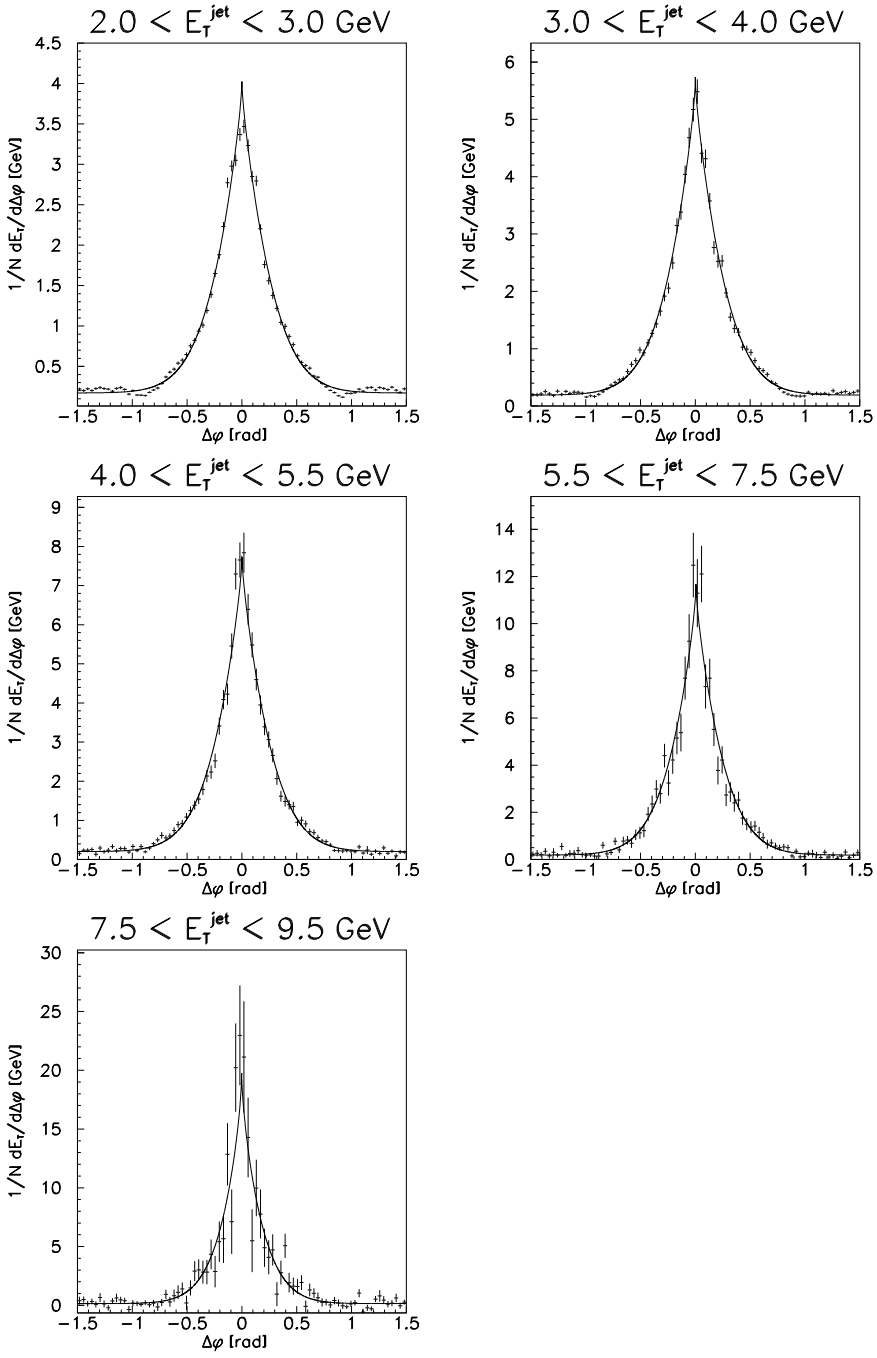

Figure 7.1: The transverse energy flows with respect to the jet axis for inclusive jet events in $\gamma\gamma$ collision (central part only). The points with the error bars are the data and the solid lines are the fitting results using the formula (7.1).

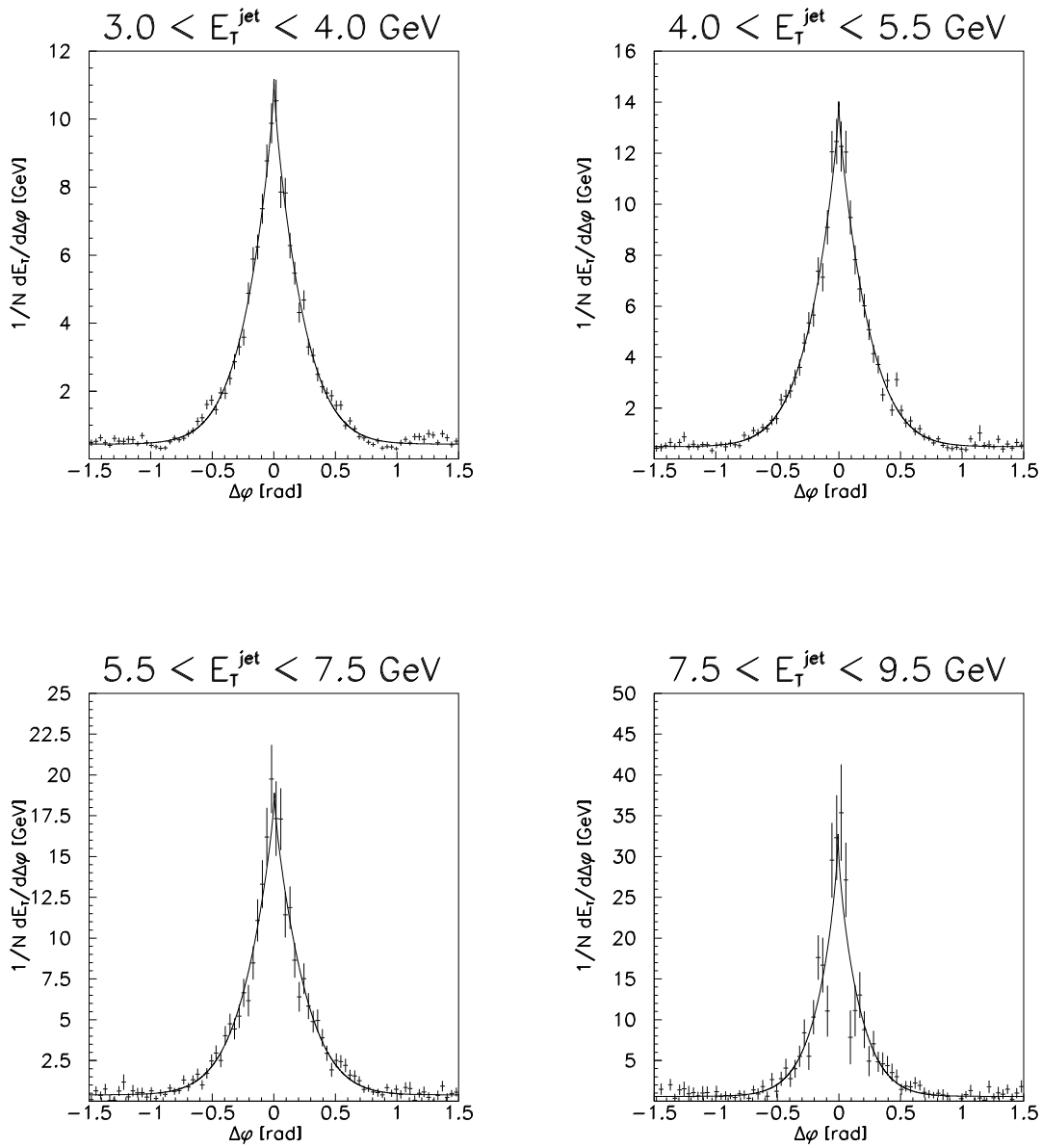

Figure 7.2: The transverse energy flows with respect to the jet axis for dijet events in $\gamma\gamma$ collision (central part only). The points with the error bars are the data and the solid lines are the fitting results using the formula (7.1).

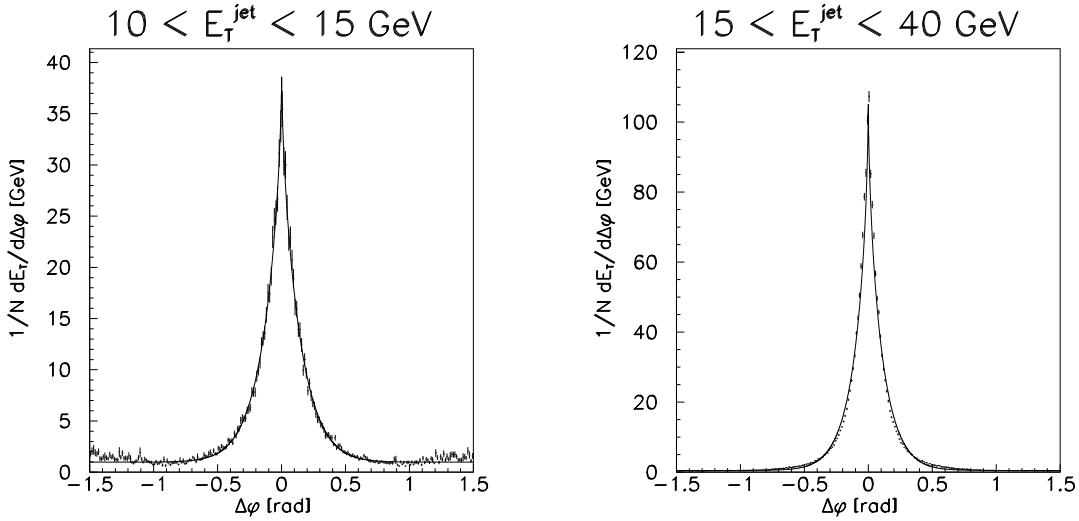

Figure 7.3: The transverse energy flows with respect to the jet axis for inclusive jet events in annihilation process (central part only). The points with the error bars are the data and the solid lines are the fitting results using the formula (7.1).

Process	E_T^{jet} region (GeV)	Number of jet	Number of dijet event
$\gamma\gamma$ collision	2.0 - 3.0	20,562	
	3.0 - 4.0	5,971	1,232
	4.0 - 5.5	2,674	832
	5.5 - 7.5	926	387
	7.5 - 9.5	293	152
e^+e^-annihilation	10 - 15	4,519	591
	15 - 40	36,108	17,873

Table 7.1: The number of jet and the number of dijet event detected in a each E_T^{jet} region.

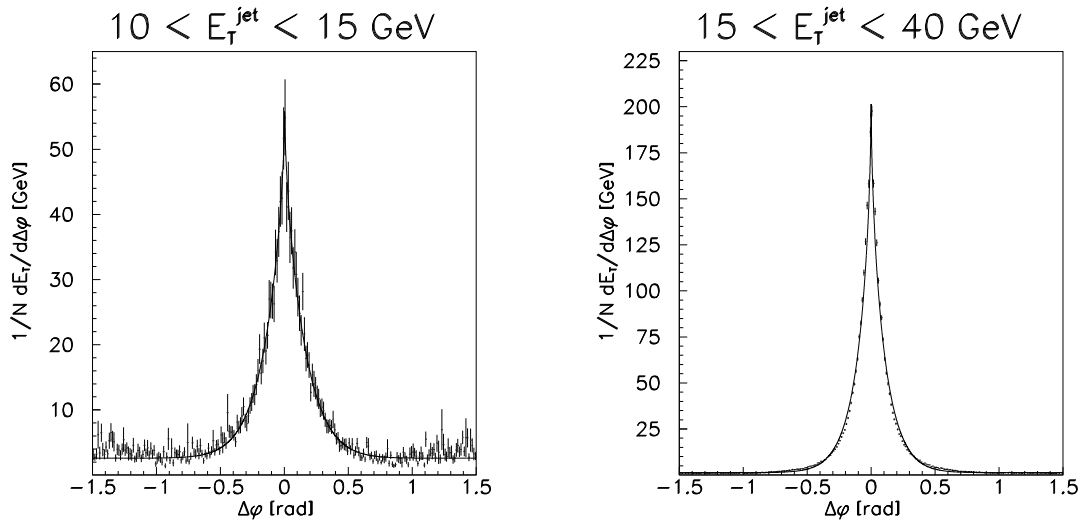

Figure 7.4: The transverse energy flows with respect to the jet axis for dijet events in annihilation process (central part only). The points with the error bars are the data and the solid lines are the fitting results using the formula (7.1).

As shown in Fig.7.1, Fig.7.2, Fig.7.3 and Fig.7.4, the jet widths become narrower as E_T^{jet} increases. The fitted results of the jet width in each E_T^{jet} bin are summarized at the column of Γ^{data} in Table 7.2 and Table 7.3 for inclusive jet sample and dijet sample, respectively.

For dijet events, we measured the averaged jet width for the first jet and the second jet. The reasons are explained as following. Fig.7.5 shows the jet width at the hadron level in Monte-Carlo simulation. Here, for the dijet event only the first jet (*i.e.* the highest E_T jet) was used. In this figure, we observed a systematic difference of the jet widths between the inclusive jet and the dijet event sample in particular high E_T^{jet} region at $15 \leq E_T^{jet} \leq 40\ GeV$, which corresponds to the e^+e^-annihilation events. In this region, the width of the first jet is larger than that of the inclusive jet by about 30%. When only the second jet (*i.e.* the second highest E_T jet) was taken at this region the width (shown by an open square) is narrower than that of the inclusive jet by about 30%.

However, this effect becomes unclear at the observed level because of the detector effects. Fig.7.6 shows the width at the observed level in the Monte-Carlo simulation. Also for the data, we could not observed significant difference of the first jet width and the averaged ones even in high E_T^{jet} region. This is the reason why we limited only to measure the averaged jet width of two highest E_T^{jet} jets for dijet samples.

7.2 Correction for Jet Width

Since the jet width is a measure of the event shape, it is expected that the distortion caused by a detector is small, but not negligible. A finite detection efficiency of the charged and neutral particles and their resolution might distort the original jet width at the hadron level. We correct these detector effects by using Monte-Carlo simulation and the jet width at the hadron level $\Gamma^{corrected}$ is obtained in each E_T^{jet} bin-by-bin from the formula (7.2),

$$\Gamma^{corrected} = \Gamma^{data} \times \frac{1}{\Gamma_{MC}^{observed}/\Gamma_{MC}^{hadron}}, \tag{7.2}$$

where Γ^{data} is the "raw" width measured in the data. $\Gamma_{MC}^{observed}$ and Γ_{MC}^{hadron} are estimated from the Monte-Carlo simulation at the observed and hadron level, respectively. The PYTHIA Monte-Carlo program is used to determine the correction factor, $\Gamma_{MC}^{observed}$ / Γ_{MC}^{hadron}. The correction factors are also summarized in Table 7.2 and Table 7.3 for inclusive jet sample and for dijet sample, respectively.

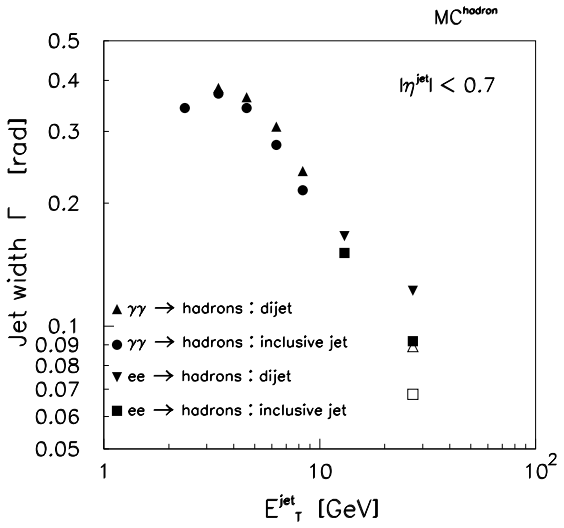

Figure 7.5: The jet width of the Monte-Carlo simulation at the hadron level. The solid circles and the solid triangles are from two-photon and the solid squares and the solid inverse triangles are the e^+e^-annihilation. For the dijet events at the highest E_T^{jet} bin, the width of the averaged and only the second jet are plotted with the open triangle and the open square, respectively. The errors are statistical only.

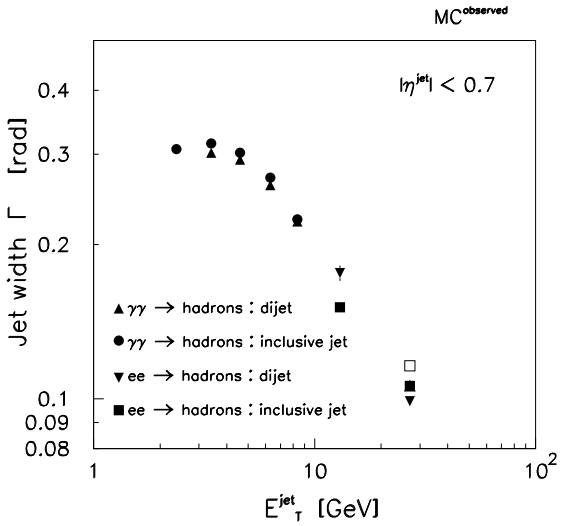

Figure 7.6: The jet width of the Monte-Carlo simulation at the observed level. The solid circles and the solid triangles are from two-photon and the solid squares and the solid inverse triangles are the e^+e^-annihilation. For the dijet events at the highest E_T^{jet} bin, the width of the averaged and only the second jet are plotted with the open triangle (hidden behind the solid square) and the open square, respectively. The errors are statistical only.

Here errors in both tables are statistical only. In these tables, the variation of the correction factors is from -15% to +15% depending on the E_T^{jet} region.

Process	E_T^{jet} region	Γ^{data}	$\Gamma_{MC}^{observed}/\Gamma_{MC}^{hadron}$
$\gamma\gamma$ collision	2.0 - 3.0	0.354±0.004	0.898±0.008
	3.0 - 4.0	0.352±0.007	0.849±0.011
	4.0 - 5.5	0.345±0.010	0.883±0.010
	5.5 - 7.5	0.318±0.017	0.971±0.013
	7.5 - 9.5	0.226±0.027	1.042±0.012
e^+e^-annihilation	10 - 15	0.153±0.002	1.001±0.015
	15 - 40	0.105±0.0005	1.155±0.005

Table 7.2: The correction factors for inclusive jet sample. The errors are statistical only.

Process	E_T^{jet} region	Γ^{data}	$\Gamma_{MC}^{observed}/\Gamma_{MC}^{hadron}$
$\gamma\gamma$ collision	3.0 - 4.0	0.304±0.009	0.871±0.016
	4.0 - 5.5	0.311±0.011	0.894±0.015
	5.5 - 7.5	0.320±0.018	0.951±0.018
	7.5 - 9.5	0.206±0.022	1.072±0.025
e^+e^-annihilation	10 - 15	0.172±0.006	1.116±0.036
	15 - 40	0.103±0.0005	1.180±0.006

Table 7.3: The correction factors for dijet sample. The errors are statistical only.

7.3 Systematic Errors

The various sources of the systematic error in the measurement of the jet width have been estimated. The main sources are given below.

7.3.1 Binning effect

The binning effect is estimated by changing the width of the histogram bin. The data in highest E_T^{jet} region (15-40 GeV) were used for this study. The standard bin width of 0.0125 *radian* has been used to measure the jet width as shown in

Figs.7.3 and Figs.7.4. We changed the bin size of the histogram by multiplying various factors, 1/5, 1/4, 1/2, 2.0, 5.0, 10.0 and 15.0. Fig.7.7 shows the effects of the change of bin size, where the vertical axis expresses the deviation of the jet width from that given from the default bin size. The jet width does not change drastically even the multiple factor is 15.0. Taking the range from 1/5 to 5.0, we estimated this error to be at most 3.0% conservatively.

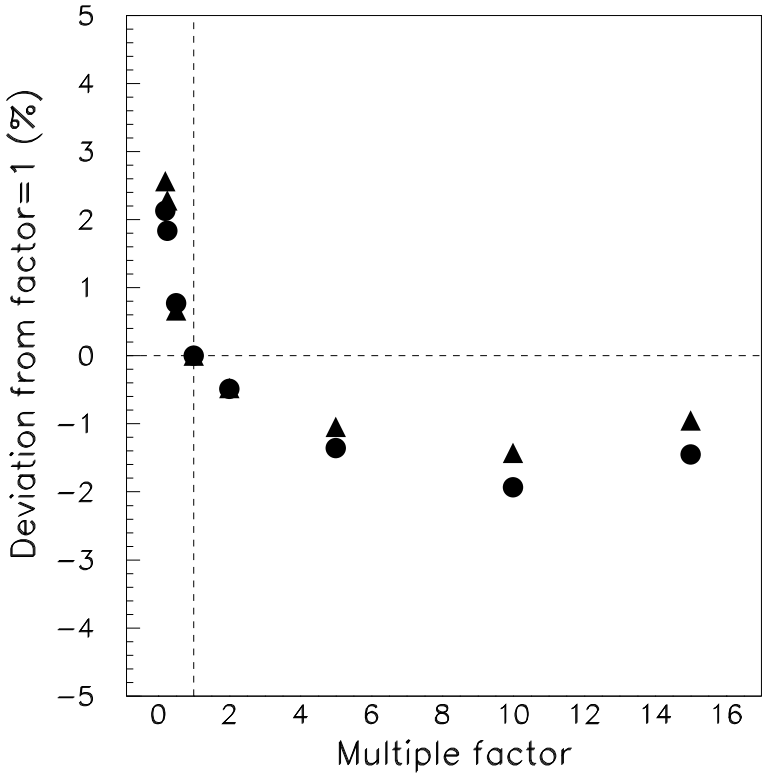

Figure 7.7: The binning effect. The triangles and the circles are the inclusive jet sample and the dijet sample, respectively. The vertical dashed line indicates factor = 1.0. The horizontal dashed line indicates no deviation from the jet width with factor = 1.0

7.3.2 E_T dependence

As described in section 5.3.2, the resolution of E_T is poor in particular at high E_T region in the e^+e^-annihilation process. This is the reason why we divided the

data into only two E_T^{jet} regions in the annihilation events ($10 \leq E_T^{jet} \leq 15\ GeV$ and $15 \leq E_T^{jet} \leq 40\ GeV$). The division into more regions has little meaning. The result of this study is shown in the followings.

Fig.7.8 shows the E_T^{jet} distribution for the e^+e^-annihilation event at the observed level. This distribution has a peak near the beam energy 29 GeV, but has a long tail in both side due to the detector resolution. In order to estimate the effect of the binning in E_T^{jet} region, we measured the jet width at following three regions ;

(i) $15\ GeV \leq E_T^{jet} < 29\ GeV$

(ii) $15\ GeV \leq E_T^{jet} < 40\ GeV$

(iii) $15\ GeV \leq E_T^{jet}$

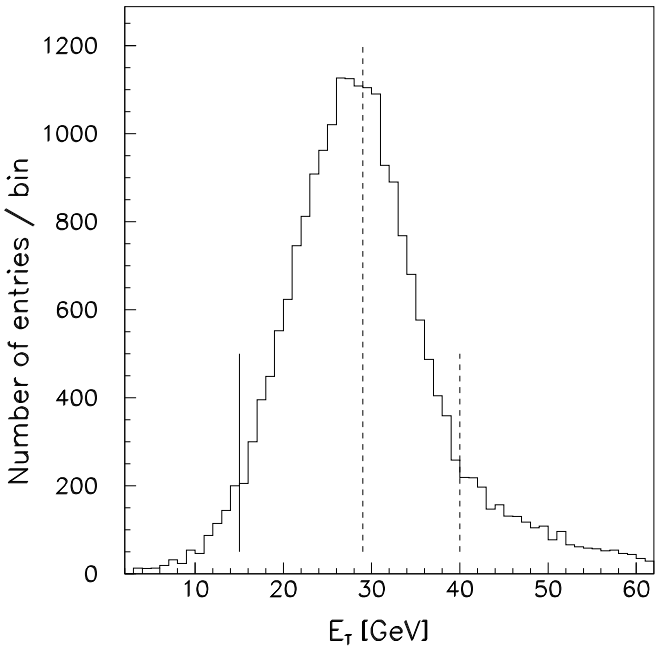

Figure 7.8: The observed E_T^{jet} distribution for the e^+e^-annihilation events.

We obtained the jet widths as summarized in Table 7.4. For Γ^{data} (*i.e.* the "raw" width from the data), there is at most $\sim 20\%$ difference among three regions, however, after making the correction of the detector effects, almost no difference is seen. As a result, the error from this source was conservatively estimated to be 2.2%.

E_T^{jet} region	15 - 29 GeV	15 - 40 GeV	$\geq$ 15 GeV
Γ^{data}	0.121	0.105	0.098
$\Gamma_{MC}^{observed}/\Gamma_{MC}^{hadron}$	1.315	1.152	1.087
$\Gamma^{corrected}$	0.092	0.091	0.090

Table 7.4: The jet widths measured for three different E_T^{jet} regions.

7.3.3 Model dependence

In order to check the effects of the Monte-Carlo model in the determination of the correction factors, we used two different Monte-Carlo programs, the PYTHIA and PHOJET programs. The difference of the correction factors from these two Monte-Carlo programs were found to be within 1%.

7.4 Results

Applying the above procedures and corrections, the jet widths at the hadron level were obtained in $\gamma\gamma$ collisions and e^+e^-annihilation process. The results are summarized in Table 7.5. In this table, the first errors are statistical and the second ones are systematic.

Process	E_T^{jet} region	$\Gamma^{corrected}$ inclusive	$\Gamma^{corrected}$ dijet
$\gamma\gamma$ collision	2.0 - 3.0	0.394 $\pm$ 0.006 $\pm$ 0.014	
	3.0 - 4.0	0.415 $\pm$ 0.010 $\pm$ 0.015	0.349 $\pm$ 0.012 $\pm$ 0.013
	4.0 - 5.5	0.391 $\pm$ 0.012 $\pm$ 0.014	0.348 $\pm$ 0.014 $\pm$ 0.013
	5.5 - 7.5	0.327 $\pm$ 0.018 $\pm$ 0.012	0.336 $\pm$ 0.020 $\pm$ 0.012
	7.5 - 9.5	0.217 $\pm$ 0.026 $\pm$ 0.008	0.192 $\pm$ 0.021 $\pm$ 0.007
e^+e^-annihilation	10 - 15	0.153 $\pm$ 0.003 $\pm$ 0.006	0.154 $\pm$ 0.007 $\pm$ 0.009
	15 - 40	0.091 $\pm$ 0.001 $\pm$ 0.003	0.087 $\pm$ 0.001 $\pm$ 0.003

Table 7.5: The corrected jet width. The first errors are statistical and the second ones are systematic.

Fig.7.9 shows the distribution of the jet width as a function of E_T^{jet}. In this figure, the errors in this figure include statistical and systematic errors added in quadrature. Solid symbols (circles, triangles, squares and inverse triangles) are

the results from this analysis. From these results we found out the following points ;

1. In the E_T^{jet} region below 4 GeV, the jet width of is almost constant and does not depend on the E_T^{jet}.

2. In the E_T^{jet} region above 4 GeV, the jet width becomes narrower as the E_T^{jet} increases.

3. The widths from $\gamma\gamma$ collisions and that from e^+e^-annihilation seem to be on a same line within the error bars.

The open circles indicate the jet widths in the γp collisions at HERA ep collider measured with H1 detector [35]. The open square and triangles are that of $p\bar{p}$ collisions at $\sqrt{s_{p\bar{p}}} = 540\ GeV$ [36] and $\sqrt{s_{p\bar{p}}} = 630\ GeV$ [37] measured with UA1 detector, respectively. As can be seen from this figure, at $E_T^{jet} = 8\ GeV$, for example, the width of jet in γp collision measured with H1 detector is three or more times larger than that of $\gamma\gamma$ collision at TRISTAN e^+e^-collider.

According to the suggestion by G.Kramer et al., [30] [31], we plot the jet width as a function of $x_T \equiv 2E_T^{jet}/\sqrt{s}$ as shown in Fig.7.10. Where $\sqrt{s}$ represents the center-of-mass energy of initial particle (*i.e.* the beam) collisions. $\sqrt{s_{ep}} = 297$ GeV is taken for H1 γp data. $\sqrt{s_{\bar{p}p}} = 540\ GeV$ and $630\ GeV$ is taken for UA1 $p\bar{p}$ data. $\sqrt{s_{e^+e^-}}$ is taken for $\gamma\gamma$ (e^+e^-) TOPAZ data. The notations in this figure are same as those in Fig.7.9. The observed x_T range in this analysis is extended to higher region with H1 result. From this figure, we can conclude that all the data can be displayed on a "universal line" if these are plotted as a function of $x_T = 2E_T^{jet}/\sqrt{s}$, although the initial states and energies are quite different. This is a strong indication of the existence of a simple scaling law for all these interactions. That is, the jet width is determined by some common mechanism independent of the detailed mechanism of the way for parton production in each interaction.

7.5 Discussions

We have measured the jet width and observed the "simple scaling law" as shown in Fig.7.10. In this section, we compare our results with two Monte-Carlo predictions.

Fig.7.11 shows the jet width of the TOPAZ data compared with that of the PYTHIA Monte-Carlo simulation. For the PYTHIA Monte-Carlo, the jet width is determined by both effects of parton-shower evolution and the hadronization. The

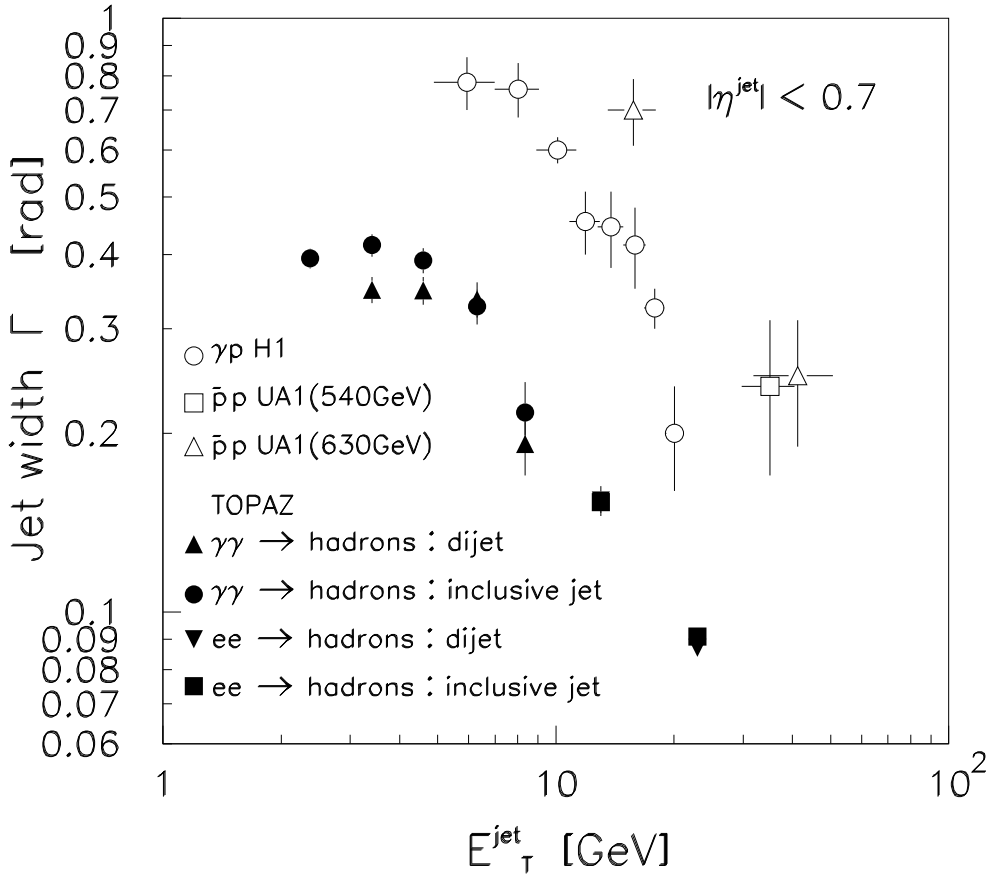

Figure 7.9: The distribution of the jet width as a function of E_T^{jet}. The solid circles and the solid triangles are from two-photon data, and the solid squares and the solid inverse triangles are e^+e^-annihilation data. The open circles, open square and open triangle are H1, UA1 ($\sqrt{s} = 540\ GeV$) and UA1 ($\sqrt{s} = 630\ GeV$), respectively. The errors include statistical and systematic errors added in quadrature.

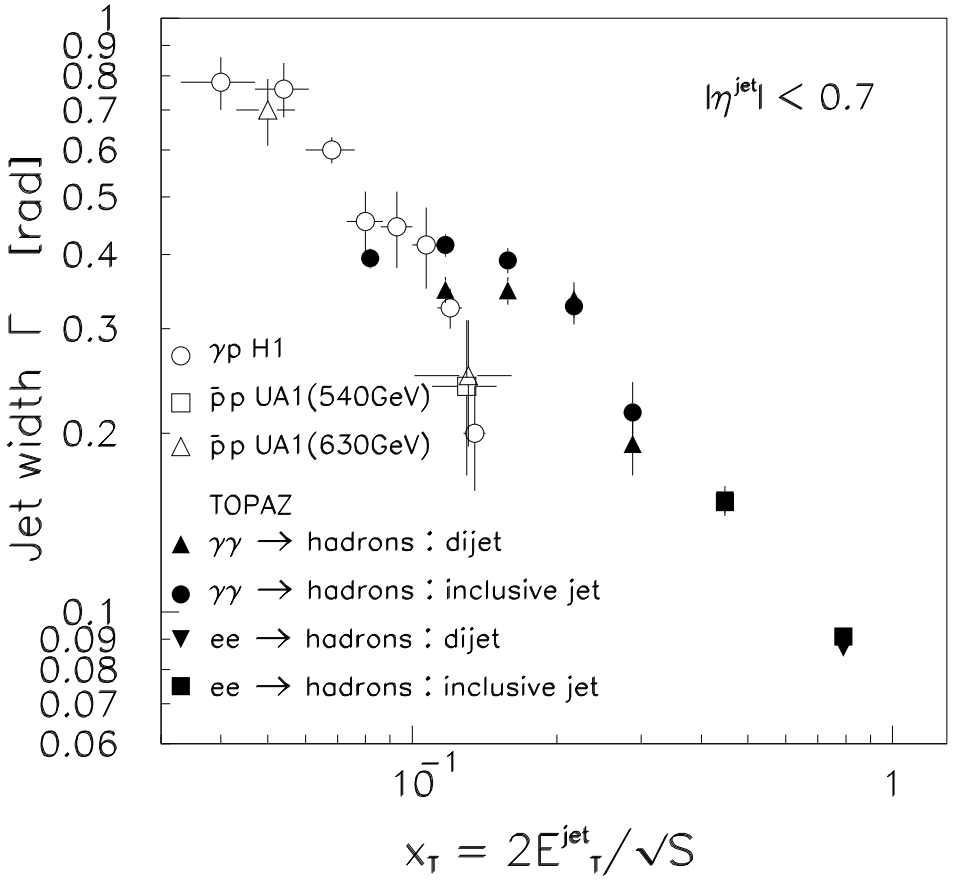

Figure 7.10: The distribution of the jet width as a function of $x_T \equiv 2E_T^{jet}/\sqrt{s}$, where $\sqrt{s}$ represents the center-of-mass energy of initial collisions. The solid circles and the solid triangles are from two-photon data, and the solid squares and the solid inverse triangles are the e^+e^-annihilation data at $\sqrt{s_{e^+e^-}} = 58\ GeV$. The open circles are H1 data at $\sqrt{s_{ep}} = 297\ GeV$. The open square and open triangle are UA1 data at $\sqrt{s} = 540\ GeV$ and $\sqrt{s} = 630\ GeV$, respectively. The errors include statistical and systematic errors added in quadrature.

open circles are the predictions including both effects, while the open triangles are that from only hadronization. As can be seen in this figure, the jet width below $E_T^{jet} \sim 3\ GeV$ can be explained only by the hadronization effects. However in the region above $E_T^{jet} \sim 4\ GeV$, the PYTHIA shows that the parton showers play an important role in the calculation of the jet width and are agree well with the data.

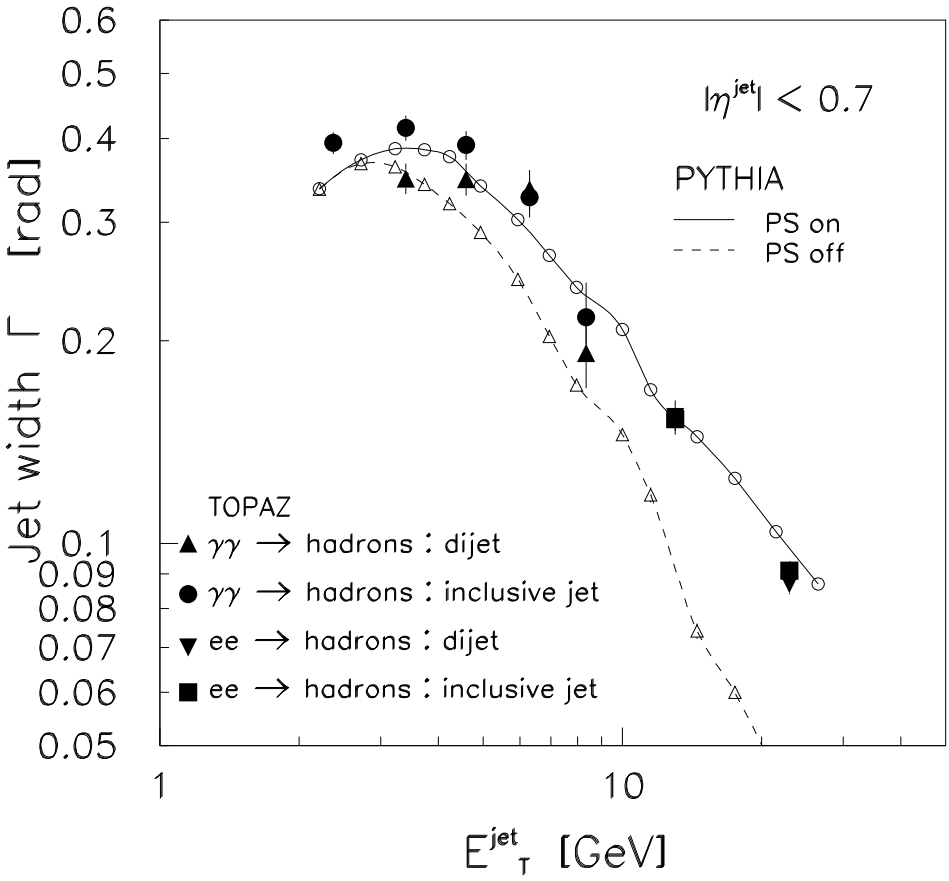

Figure 7.11: Comparison of TOPAZ data with the PYTHIA predictions. The solid circles and the solid triangles are from two-photon data, and the solid squares and the solid inverse triangles are the e^+e^-annihilation data. The solid line with open circles is a PYTHIA prediction with the parton shower. The dashed line with open triangles is the same prediction without the parton shower.

The TOPAZ data are also compared with the PHOJET Monte-Carlo simulation as shown in Fig.7.12. PHOJET Monte-Carlo deals with the same hadroniza-

tion procedure as that for the PYTHIA, and includes soft process by more sophisticated way. However, the agreement between the data and the PHOJET is poorer than that with the PYTHIA.

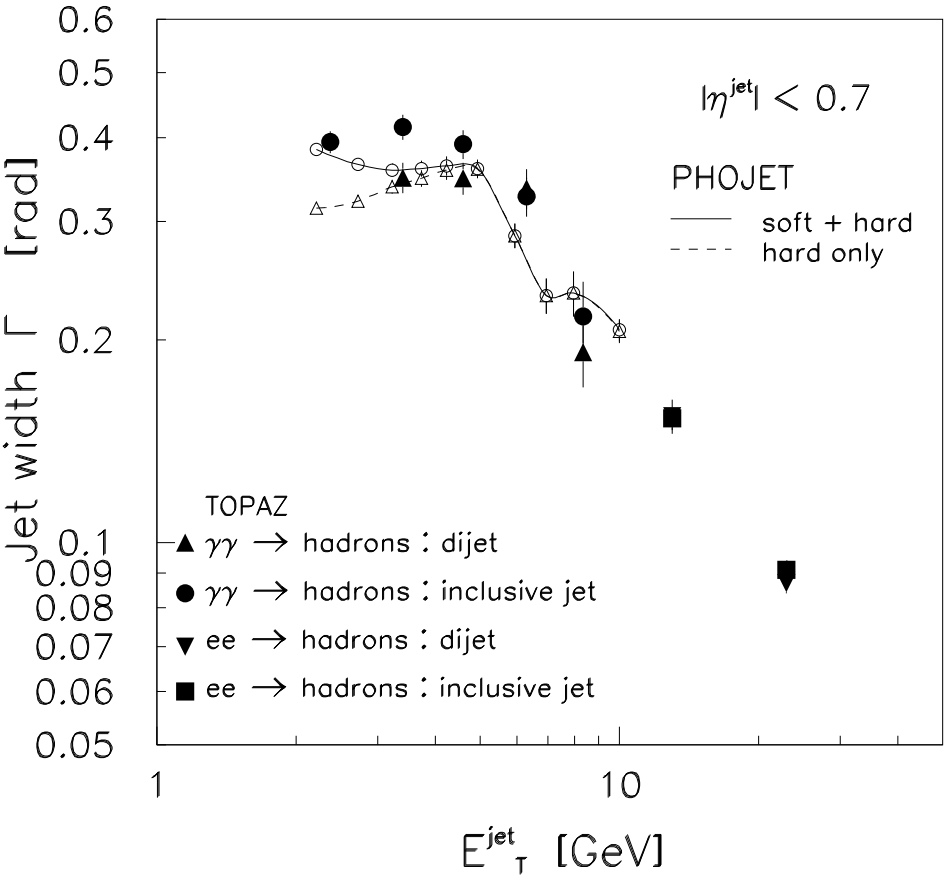

Figure 7.12: Comparison of TOPAZ data with the PHOJET predictions. The solid circles and the solid triangles are from two-photon data, and the solid squares and the solid inclusive triangles are the e^+e^-annihilation data. The solid line with open circles is PHOJET predictions included the soft components. The dashed line with the open triangles is the same predictions without the soft components (*i.e.* the hard process only). The error bars of open symbols are statistical only.

Chapter 8

Conclusion

We have studied the jet production in the quasi-real $\gamma\gamma$ collisions with the TOPAZ detector at the TRISTAN e^+e^-collider. The data correspond to the integrated luminosity of 287.8 pb^{-1} at the center-of-mass energy ($\sqrt{s}$) of 58 GeV. The jets used in this analysis were reconstructed with "cone algorithm".

In this thesis, detailed analyses were carried out to study mainly the following two issues ;

1. Intrinsic features of quasi-real photon,

2. Universality of jet profile.

For the first item, we used dijet events in the $\gamma\gamma$ collision and for the second item, all jets in the $\gamma\gamma$ collisions and in the e^+e^-annihilations were used. Here we conclude these items.

Intrinsic features of quasi-real photon

The dijet event, which has at least two high E_T jets, is the most fundamental event in $\gamma\gamma$ collisions. The momentum fraction of parton inside a photon (x_γ) can be reconstructed only in the dijet event. We succeeded to separate the direct process and the resolved process from the dijet event well. This good separation is the first time for e^+e^-collider experiments. Especially resolved sample is important to study the quasi-real photon, and its purity of almost 90% was achieved in this study.

Using the resolved sample, we examined mainly the following two points ;

- Effect of the gluon radiation at initial state in hard sub-process (QCD initial state radiation),

- The shape of the primordial transverse momentum (k_T) of the parton inside a photon.

In particular, k_T directly relates to the intrinsic structure of photon.

As a result, we could observe the important effect of the QCD initial state radiation. And the $q\bar{q}$ pair fluctuated from photon is bounded more loosely rather than makes a hadron in the energy region of TRISTAN.

Universality of jet profile

A precise measurement of jet profile can give information about the higher order QCD cross section. In this thesis, the jet width in the $\gamma\gamma$ collisions, as well as in the e^+e^-annihilation process, has been studied for the first time. The transverse energy (E_T^{jet}) dependence of the jet width was found to be quite universal regardless of the system of jet production. These are the first measurements which provided us the jet width in the wide range of the variable x_T up tp $x_T \sim 1$.

We further compared the jet widths with those in other experiments, such as γp collision and $p\bar{p}$ collision as a function of x_T. We found that a "simple scaling law" which has been applied to γp and $p\bar{p}$ experiments can be extended to the jet width in the $\gamma\gamma$ collisions and the e^+e^-annihilation. From this result, we could conclude that the jet width may be determined by some common mechanism which is independent of the detailed way of the parton production in each interaction.

Appendix A

Cross Section Formula for Sub-Processes

Here, we summarize below the cross section formula for the sub-processes relevant in the $\gamma\gamma$ collisions. In the formula below, $\hat{\theta}$ is a scattering angle in the center-of-mass system and $\hat{s}$, $\hat{t}$ and $\hat{u}$ are Mandelstam variables. The suffixes for q indicate the quark flavor, e_q is a quark charge, and $\hat{\beta}$ is a quark velocity : $\hat{\beta} = \sqrt{1 - 4m_q^2/\hat{s}}$. Note that the formula (A.4) includes the factors of 2 since we integrate all polar angle range.

$\underline{\gamma\gamma \to q_i\bar{q}_i}$

$$\begin{aligned}\frac{d\sigma}{d\cos\hat{\theta}} &= \frac{3\pi\alpha^2 e_q^4\hat{\beta}}{\hat{s}}\left[\frac{m_q^2-\hat{t}}{m_q^2-\hat{u}}+\frac{m_q^2-\hat{u}}{m_q^2-\hat{t}}+4\left(\frac{m_q^2}{m_q^2-\hat{t}}+\frac{m_q^2}{m_q^2-\hat{u}}\right)\right.\\ &- \left. 4\left(\frac{m_q^2}{m_q^2-\hat{t}}+\frac{m_q^2}{m_q^2-\hat{u}}\right)^2\right]. \qquad \text{(A.1)}\end{aligned}$$

$\underline{\gamma q_i \to q_i g}$

$$\frac{d\sigma}{d\cos\hat{\theta}} = -\frac{4\pi\alpha e_q^2\alpha_S}{3\hat{s}}\left(\frac{\hat{t}}{\hat{s}}+\frac{\hat{s}}{\hat{t}}\right) \qquad \text{(A.2)}$$

$\underline{\gamma g \to q_i\bar{q}_i}$

$$\begin{aligned}\frac{d\sigma}{d\cos\hat{\theta}} &= \frac{\pi\alpha e_q^2\alpha_S\hat{\beta}}{2\hat{s}}\left[\frac{m_q^2-\hat{t}}{m_q^2-\hat{u}}+\frac{m_q^2-\hat{u}}{m_q^2-\hat{t}}+4\left(\frac{m_q^2}{m_q^2-\hat{t}}+\frac{m_q^2}{m_q^2-\hat{u}}\right)\right.\\ &- \left. 4\left(\frac{m_q^2}{m_q^2-\hat{t}}+\frac{m_q^2}{m_q^2-\hat{u}}\right)^2\right]. \qquad \text{(A.3)}\end{aligned}$$

$\underline{q_i + q_i \rightarrow q_i + q_i}$

$$\frac{d\sigma}{d\cos\hat{\theta}} = \frac{\pi\alpha_S^2}{4\hat{s}}\left[\frac{4}{9}\left(\frac{\hat{s}^2+\hat{u}^2}{\hat{t}^2}+\frac{\hat{s}^2+\hat{t}^2}{\hat{u}^2}\right)-\frac{8}{27}\frac{\hat{s}^2}{\hat{u}\hat{t}}\right] \tag{A.4}$$

$\underline{q_i + q_j \rightarrow q_i + q_j}$

$$\frac{d\sigma}{d\cos\hat{\theta}} = \frac{\pi\alpha_S^2}{2\hat{s}}\left[\frac{4}{9}\frac{\hat{s}^2+\hat{u}^2}{\hat{t}^2}\right] \tag{A.5}$$

$\underline{q_i + \bar{q}_i \rightarrow q_i + \bar{q}_i}$

$$\frac{d\sigma}{d\cos\hat{\theta}} = \frac{\pi\alpha_S^2}{2\hat{s}}\left[\frac{4}{9}\left(\frac{\hat{s}^2+\hat{u}^2}{\hat{t}^2}+\frac{\hat{t}^2+\hat{u}^2}{\hat{s}^2}\right)-\frac{8}{27}\frac{\hat{u}^2}{\hat{s}\hat{t}}\right] \tag{A.6}$$

$\underline{q_i + \bar{q}_i \rightarrow q_j + \bar{q}_j}$

$$\frac{d\sigma}{d\cos\hat{\theta}} = \frac{\pi\alpha_S^2\hat{\beta}}{2\hat{s}}\frac{4}{9}\left[\frac{(m_q^2-\hat{t})^2+(m_q^2-\hat{u})^2+2m_q^2\hat{s}}{\hat{s}^2}\right] \tag{A.7}$$

$\underline{q_i + \bar{q}_j \rightarrow q_i + \bar{q}_j}$

$$\frac{d\sigma}{d\cos\hat{\theta}} = \frac{\pi\alpha_S^2}{2\hat{s}}\frac{4}{9}\left[\frac{\hat{s}^2+\hat{u}^2}{\hat{t}^2}\right] \tag{A.8}$$

$\underline{q_i + \bar{q}_i \rightarrow g + g}$

$$\frac{d\sigma}{d\cos\hat{\theta}} = \frac{\pi\alpha_S^2}{2\hat{s}}\left[\frac{32}{27}\frac{\hat{u}^2+\hat{t}^2}{\hat{u}\hat{t}}-\frac{8}{3}\frac{\hat{u}^2+\hat{t}^2}{\hat{s}^2}\right] \tag{A.9}$$

$\underline{q_i + g \rightarrow q_i + g}$

$$\frac{d\sigma}{d\cos\hat{\theta}} = \frac{\pi\alpha_S^2}{2\hat{s}}\left[-\frac{4}{9}\frac{\hat{u}^2+\hat{s}^2}{\hat{u}\hat{s}}+\frac{\hat{u}^2+\hat{s}^2}{\hat{t}^2}\right] \tag{A.10}$$

$\underline{g + g \to q_i + \bar{q}_i}$

$$\begin{aligned}\frac{d\sigma}{d\cos\hat{\theta}} &= \frac{\pi\alpha_S^2\hat{\beta}}{32\hat{s}}\left[12\frac{(m_q^2-\hat{t})(m_q^2-\hat{u})}{\hat{s}^2}+\frac{8}{3}\frac{(m_q^2-\hat{t})(m_q^2-\hat{u})-2m_q^2(m_q^2+\hat{t})}{(m_q^2-\hat{t})^2}\right.\\ &+ \frac{8}{3}\frac{(m_q^2-\hat{t})(m_q^2-\hat{u})-2m_q^2(m_q^2+\hat{u})}{(m_q^2-\hat{u})^2}-\frac{2}{3}\frac{m_q^2(\hat{s}-4m_q^2)}{(m_q^2-\hat{t})(m_q^2-\hat{u})}\\ &- 6\frac{(m_q^2-\hat{t})(m_q^2-\hat{u})+m_q^2(\hat{u}-\hat{t})}{\hat{s}(m_q^2-\hat{t})}\\ &- \left.6\frac{(m_q^2-\hat{t})(m_q^2-\hat{u})+m_q^2(\hat{t}-\hat{u})}{\hat{s}(m_q^2-\hat{u})}\right] \qquad \text{(A.11)}\end{aligned}$$

$\underline{g + g \to g + g}$

$$\frac{d\sigma}{d\cos\hat{\theta}} = \frac{\pi\alpha_S^2}{4\hat{s}}\frac{9}{2}\left[3-\frac{\hat{u}\hat{t}}{\hat{s}^2}-\frac{\hat{u}\hat{s}}{\hat{t}^2}-\frac{\hat{s}\hat{t}}{\hat{u}^2}\right] \qquad \text{(A.12)}$$

Appendix B

Parton Density Function inside a Photon

In the deep inelastic $e\gamma$ scattering in e^+e^- colliders, the virtual photon γ^* emitted from tagged electron can act as a point-like probe and test the quark contents in the quasi-real target photon γ (shown in Fig. B.1).

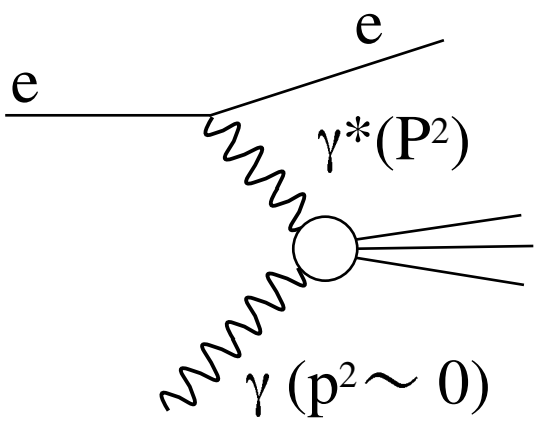

Figure B.1: Generic Feynman diagram for deep-inelastic $e\gamma$ scattering: A probing photon with large virtuality $P^2 \equiv -q^2$ scatters off the (quasi-) real target photon (with virtuality $p^2 \simeq 0$) to produce a hadronic final state.

In deep-inelastic $e\gamma$ scattering, measurement of the differential cross section of Q^2 and the parton fractional momentum x_γ gives the structure function of the (quasi-) real photon:

$$\frac{d^2\sigma}{dx_\gamma dQ^2} = \frac{4\pi\alpha^2}{x_\gamma Q^4}\left(1 - y + \frac{y^2}{2}\right) F_2^\gamma(x_\gamma, Q^2) \tag{B.1}$$

Here α is the fine structure constant and y denotes the scaled photon energy. y is related to Q^2 and x_γ via $Q^2 = x_\gamma y s_{ee}$ where $\sqrt{s_{ee}}$ is the e^+e^- center-of-mass energy.

A compilation of all F_2^γ measurements, available in 1994, is shown in Fig. B.2(from [69]). The data cover the photon virtuality in the range $0.7 < Q^2 < 100\mathrm{GeV}^2$ and the parton momentum fraction up to $x_\gamma = 0.9$. The data appear essentially flat in x_γ, but show a significant rise with increasing Q^2.

The F_2^γ is related to the quark densities in the photon $q_i^\gamma(x, Q^2)$. In leading order, it is given by:

$$F_2^\gamma(x, Q^2) = 2x \sum_i e_{q_i}^2 q_i^\gamma(x, Q^2), \tag{B.2}$$

where the sum runs over flavors, e_{q_i} is the electric charge of quark q_i, and the factor of 2 takes care of anti-quarks.

Theoretically, the structure function include all contributions of the diagrams shown in Figs. B.3([16]), Where the flavor non-singlet (NS) sector and singlet sector are treated separately. As shown in Fig. B.3(d), there also exist the non-perturbative contributions described by VDM.

Since the non-perturbative contribution is included, only the Q^2 dependence can be determined from the theory as same as the case of nucleon structure function. The Q^2-dependence of the parton density function$q^\gamma(x = x_\gamma, Q^2)$ is given by the inhomogeneous Altarelli-Parisi(AP) equations. In LO, they read [17] :

$$n\frac{dq_{\mathrm{NS}}^\gamma(x, Q^2)}{d\log Q^2} = \frac{\alpha_{\mathrm{em}}}{2\pi} k_{\mathrm{NS}}^\gamma(x) + \frac{\alpha_s(Q^2)}{2\pi} \left(P_{qq} \otimes q_{\mathrm{NS}}^\gamma\right)(x, Q^2); \tag{B.3}$$

$$\frac{d\Sigma^\gamma(x, Q^2)}{d\log Q^2} = \frac{\alpha_{\mathrm{em}}}{2\pi} k_\Sigma^\gamma(x) + \frac{\alpha_s(Q^2)}{2\pi} \left[\left(P_{qq} \otimes \Sigma^\gamma\right)(x, Q^2) + \left(P_{qG} \otimes G^\gamma\right)(x, Q^2)\right]; \tag{B.4}$$

$$\frac{dG^\gamma(x, Q^2)}{d\log Q^2} = \frac{\alpha_s(Q^2)}{2\pi} \left[\left(P_{Gq} \otimes \Sigma^\gamma\right)(x, Q^2) + \left(P_{GG} \otimes G^\gamma\right)(x, Q^2)\right], \tag{B.5}$$

where $P \otimes q$ is a convolution integral defined as,

$$\left(P \otimes q\right)(x, Q^2) \equiv \int_x^1 \frac{dy}{y} P(y) q(\frac{x}{y}, Q^2). \tag{B.6}$$

$P_{ij}(y)$ is the (LO) $j \to i$ splitting function, which represents the probability that the daughter parton i carries a fraction y of the momentum of the parent parton j [18]. Quark,gluon splitting functions are given by

$$P_{qq}(z) = \frac{4}{3}\left[\frac{1+z^2}{(1-z)_+} + \frac{3}{2}\delta(1-z)\right], \tag{B.7}$$

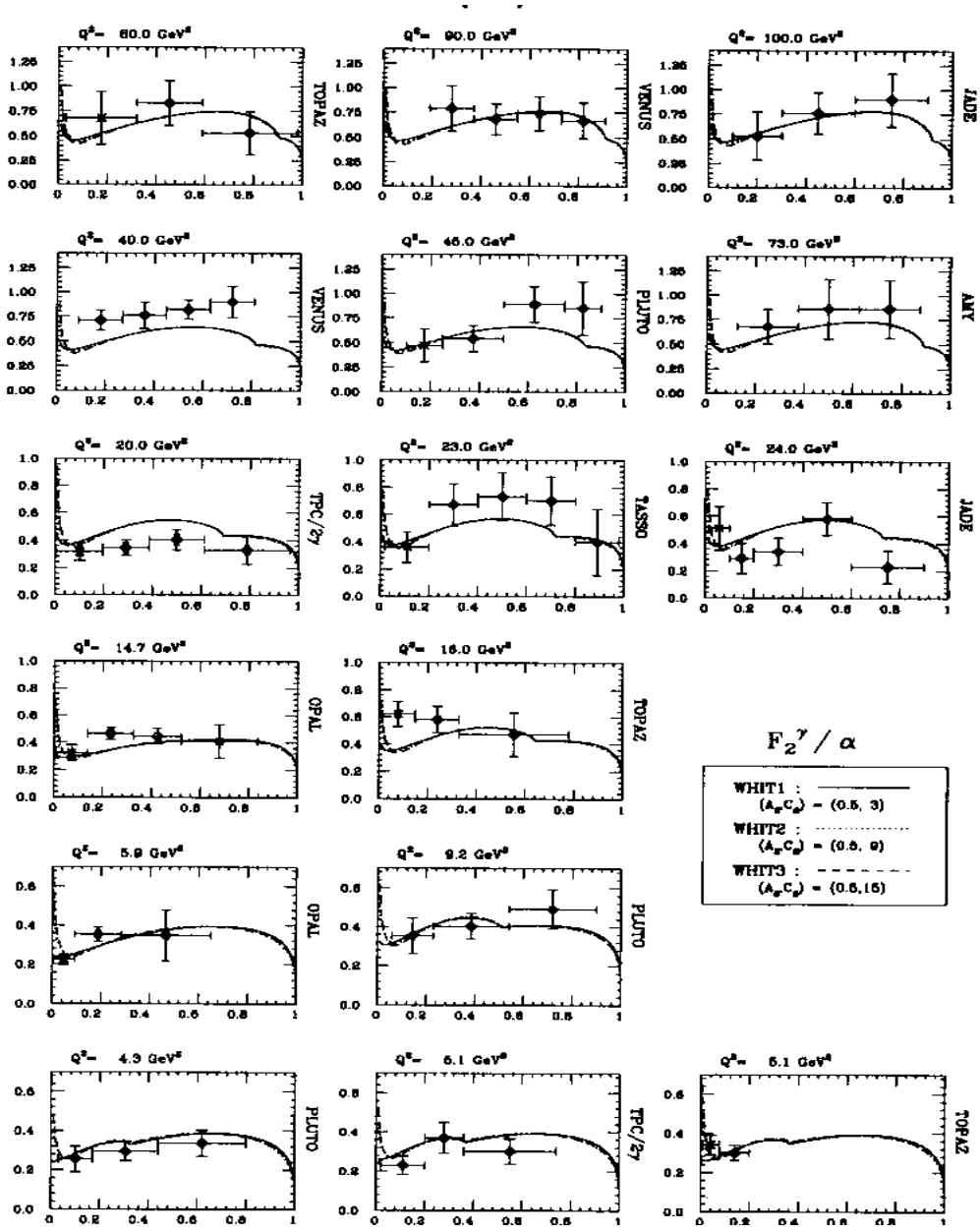

Figure B.2: Measurements of the photon structure function F_2^γ/α. The data(full symbol) are drawn as a function of the parton momentum fraction x_γ(ref.[69]).

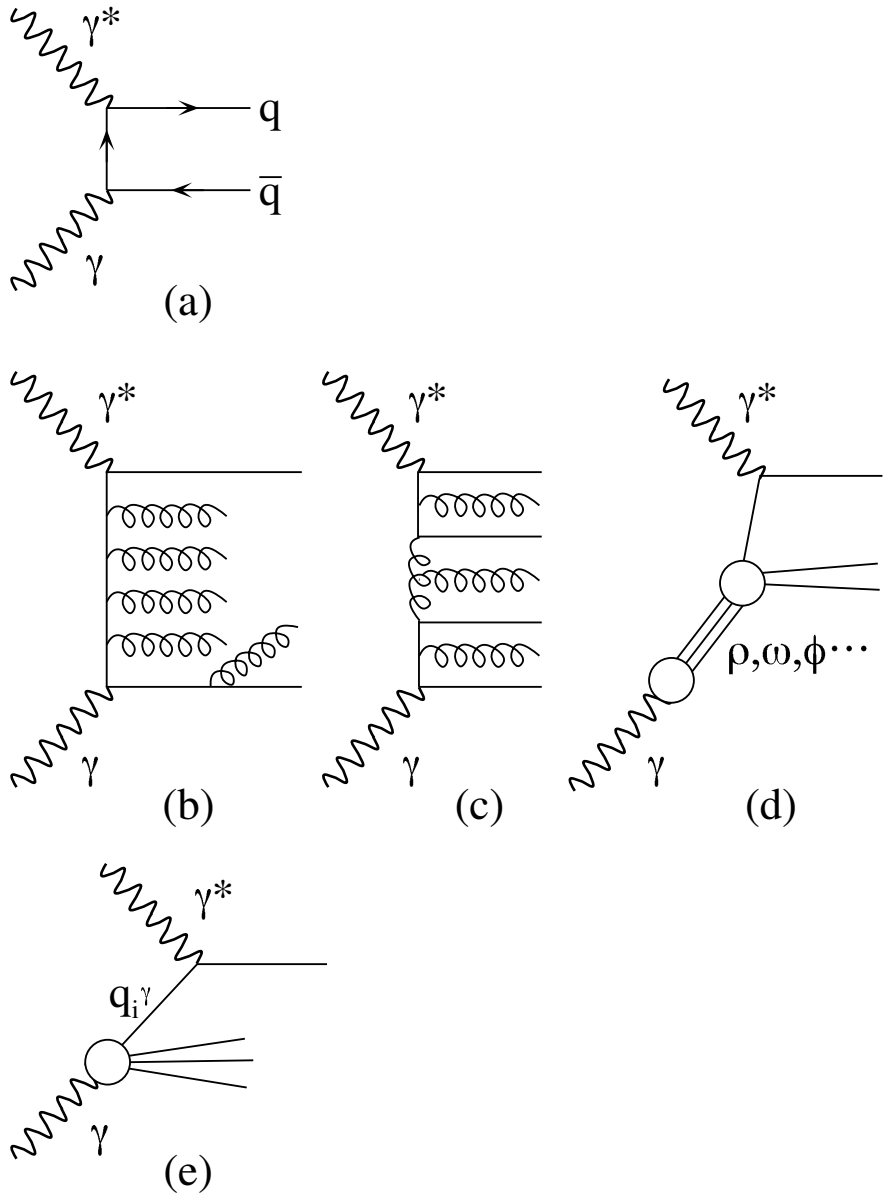

Figure B.3: Feynman diagrams that contribute to $\gamma^*\gamma$ scattering. (a) a lowest order (QPM) contribution, (b) and (c) are examples of perturbative QCD corrections in the flavor non-singlet and singlet sector, respectively, and (d) non-perturbative contributions described by the VDM. All these contributions are formally summed in (e).

$$P_{gq}(z) = \frac{4}{3}\frac{1+(1-z)^2}{z}, \tag{B.8}$$

$$P_{qg}(z) = \frac{1}{2}\left[z^2+(1-z)^2\right], \tag{B.9}$$

$$P_{gg}(z) = 6\left[\frac{z}{(1-z)_+}+\frac{(1-z)}{z}+z(1-z)+\left(\frac{11}{12}-\frac{n_f}{18}\right)\delta(1-z)\right] \tag{B.10}$$

While the inhomogeneous term of the photon splitting functions k_i^γ reads

$$k_{q_i}^\gamma(z) = 3e_{q_i}^2\left[z^2+(1-z)^2\right]. \tag{B.11}$$

This term describes $\gamma \to q\bar{q}$ splitting, *i.e.* the diagram of Fig. B.3(a).

The equation (eqB.3) describes the evolution of the non-singlet distributions, i.e. resume only the type of the diagrams shown in Fig. B.3(b). While equations of (eqB.4) and (eqB.5) describe the evolution of the singlet sector ($\Sigma^\gamma \equiv \sum_i q_i^\gamma + \bar{q}_i^\gamma$), which includes the diagrams of the kind shown in Fig. B.3(c). In this sector, A gluon density inside the photon $G^\gamma(x,Q^2)$ is required.

Using given input distributions taken from experimental data and above equations, it is possible to determine the absolute prediction of $F_2^\gamma(x,Q^2)$. Since the experimental has still large errors, the gluon density function in particular, is essentially unconstrained by the deep inelastic $e\gamma$ data.

Appendix C

Raw Data Processing

C.1 Data Processing Flow

The flow of the TOPAZ offline analysis is sketched in Fig.C.1. The data transferred from the VAX are temporarily copied on the disk buffer of the FACOM M-780. These data are recorded on magnetic cassette tapes, each of which has $\sim$ 280 *Mbytes* capacity. An automatic mounting system (CTL) is employed for the cassette tapes, which ensures quick and easy access to a large amount of data. The data are converted to the TOPAZ standard data format to match out data handling system called TRISTAN Bank System (TBS). The formatted data are stored as raw data.

The contents of the raw data are direct log of readout electronics such as Analogue-to-Digital Converters (ADC) and Time-to-Digital Converters (TDC). For physics analysis, on the other hand, we need essentially only two physical observables, p^μ and x^μ, for each track. These informations are reconstructed from the raw data in the following two steps, "reduction" and "production".

In the reduction step, the raw data are reduced in size and channel by channel dependence inherent are removed by calibration. Calibration corrects for electronics nonlinearity and pedestals, etc. Obviously non-physics events such as beam-gas events are rejected here to make the data size reasonable and consequently to save the CPU time for the production step. The data which passed the reduction filters proceed to the production step which converts the reduced data to the following physical observables:

- the vertex position and momentum for each charged track,

- particle species for each charged track, and

- energy cluster in the calorimeters,

and produces Data Summary Tapes (DST) carrying these informations. The DST's are also handled by the CLS system.

C.2 Event Reconstruction

The raw data are then calibrated for the channel-to-channel variations and the non-linearity of the electronics. The pattern recognition of the event is performed using the TPC pad signals. First the spatial positions of 'hits' found in the TPC are determined. The tracks of charged particles are searched for among the positions of hits. Each track found is fitted to a helix and the charge and the momentum are assigned. After the track reconstruction, particle identity is determined for each track by the dE/dX measurements in the TPC.

After charged tracks are reconstructed in the TPC, the signals from calorimeters are examined and the position and energy of photons and electrons in the BCL, ECL and FCL are calculated.

C.2.1 Track Reconstruction

As shown in Fig.C.2, the global coordinate in the TOPAZ detectors is defined with the X, Y, and Z. The origin of the coordinate is the detector center. Another coordinate system fixed on the TPC sector is defined as shown in Fig.C.2. The ξ-axis is along the sense wire direction, the η-axis points in the radial direction at the center line of the sector, and the ζ-axis is along the beam line.

The TPC track reconstruction can be divided into three steps, namely, the reconstruction of the hit positions, the track finding and the track refinement. These steps are schematically shown in Fig.C.3. The detail of each step is described in the following subsections.

Reconstruction of Space Points

The reconstruction of hit points in the TPC begins by grouping pad signals into clusters. The pad signals are calibrated for electronics variation in Charge Coupled Device (CCD) bucket-by-bucket basis prior to this step.

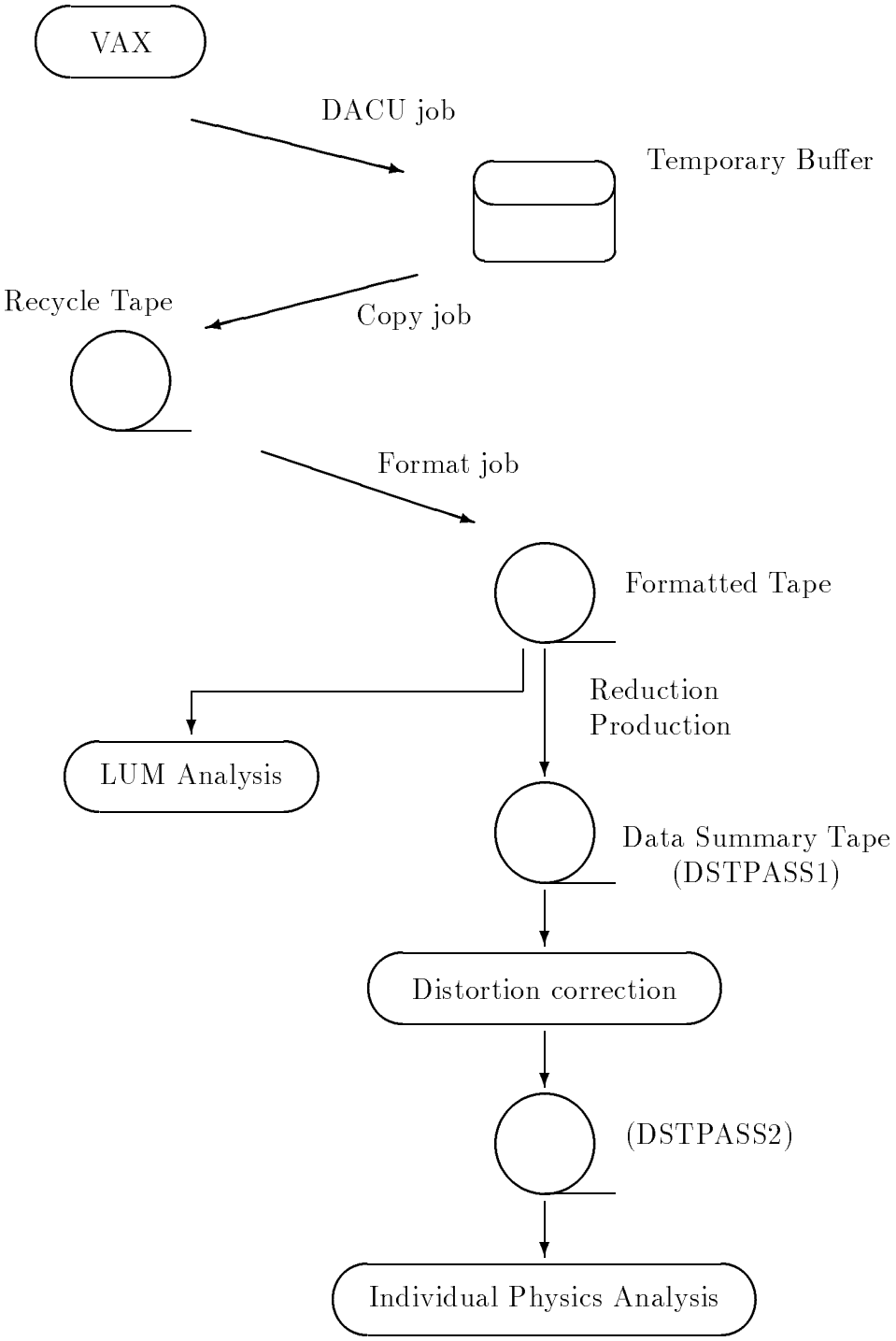

Figure C.1: A flow chart of TOPAZ offline analysis system.

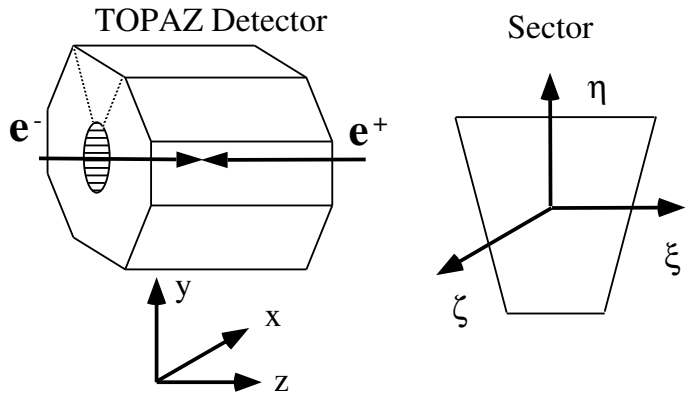

Figure C.2: TPC sector coordinate.

In this first stage of the pad clustering, the output signal of each channel is examined as a function of the CCD bucket number. The contiguous signals are combined to form ζ hits. the peak pulse height and the ζ position of each cluster are determined by fitting the highest three CCD buckets to a parabola. Clusters are then searched in the ξ direction. If hits in contiguous pads have roughly the same ζ position, i.e., within 1 cm, these hits are combined to a cluster.

After a cluster is found, the η position of the cluster is determined. The position is equal to the radial position of the pad row containing the cluster, but the position is corrected for the Landau fluctuation of wire signals since the five wires nearest the pad row contributes the pad pulse height.

The ξ positions of a cluster are calculated by fitting the highest three pad pulse heights to a Gaussian shape. If only two pad signals are above threshold, pre-determined width of the Gaussian is used for the fit. The ζ position is also determined in the same way as the ξ position. The three dimensional space point of each hit is determined in this way.

Track Finding

To find tracks from the reconstructed space points of hits, all the points are first filled in a two dimensional histogram with ϕ and $Z(R_{ref})$ axes, where,

$$\begin{aligned} \phi &= tan^{-1}(\frac{X}{\sqrt{X^2+Y^2}}) \\ Z(R_{ref}) &= Z \times (\frac{R_{ref}}{R}) \end{aligned}$$

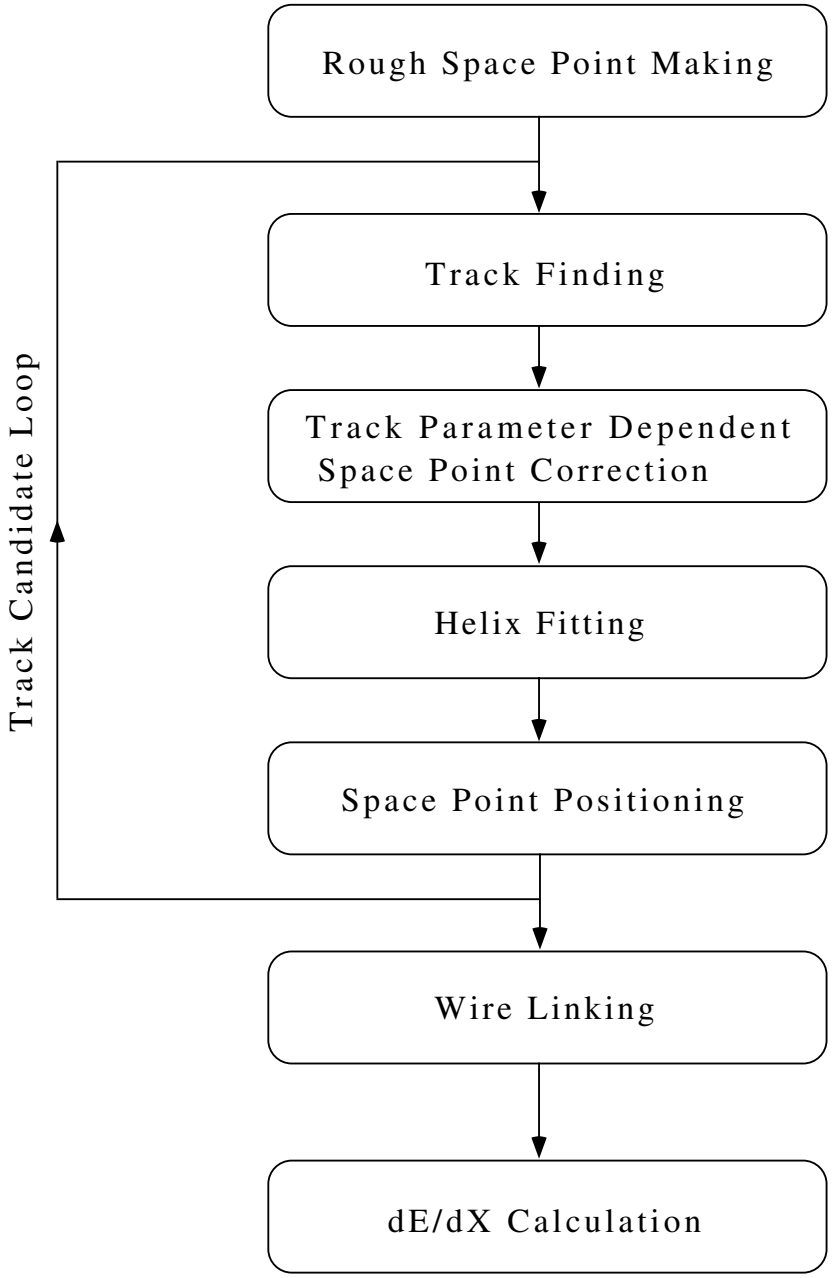

Figure C.3: The flow chart of TPC track reconstruction.

R_{ref} is the radial position of the fixed reference point. The space points on a track from the origin with relatively high momentum are clustered in a bin in this histogram [47]. To find tracks, bins containing space points more than a threshold number are searched for. At the beginning, the threshold is set at 9 corresponding to 10 pad row hits, and then lowered by 1 when all bins above the current threshold are found. The lowering of the threshold is repeated until the threshold becomes 2.

If a bin with space points more than the threshold number is found, the space points are tested to form a track or not. From the space points, three points are chosen to span the largest lever arm and checked if they are on a helix function (called the "test helix"). If the space points are on the helix, the expected point from the helix function are calculated for each pad row and tested if they can be associated with the space points in the bin. If enough number of the space points are associated, they are recognized to form a track and fitted to a helix function.

Before the helix fitting, the space points are corrected for known dependences on the track angle to the sectors using the "test helix" parameters. The helix function is parametrized as follows;

$$\begin{aligned} X &= X_0 + d\rho \cdot cos\phi_0 + \frac{\alpha}{\kappa}(cos\phi_0 - cos(\phi + \phi_0)) \\ Y &= Y_0 + d\rho \cdot sin\phi_0 + \frac{\alpha}{\kappa}(sin\phi_0 - sin(\phi + \phi_0)) \\ Z &= Z_0 + dZ - \frac{\alpha}{\kappa} \cdot \phi \cdot tan\lambda. \end{aligned} \tag{C.1}$$

The parameters in Eqs.(C.1) are summarized in Table C.1. The parameters to be fitted are $d\rho$, ϕ_0, κ, dZ, and $tan\lambda$. These definitions are shown in Fig.C.4.

The fitting of the helix is carried out by minimizing the χ^2 defined as:

$$\chi^2 = \sum_i ((\frac{\xi_i - \xi(\eta_i)}{\sigma_{\eta_i}})^2 + (\frac{Z_i - Z(\eta_i)}{\sigma_{Z_i}})^2),$$

where ξ_i and Z_i are the measured position in the i-th pad row and $\xi(\eta_i)$ and $Z(\eta_i)$ are the expected position by the helix. We checked this χ^2 and made the final decision to recognize the space points as a track or not.

After all histogram bins forming tracks are found, the space points which are not recognized as tracks are then examined. From the remaining histogram bins, the bin containing the largest number of space points is searched for. The inner-most space point in the bin is chosen to be the origin (pivot) of the new histogram. The new histogram is defined with wider bins so that space points of

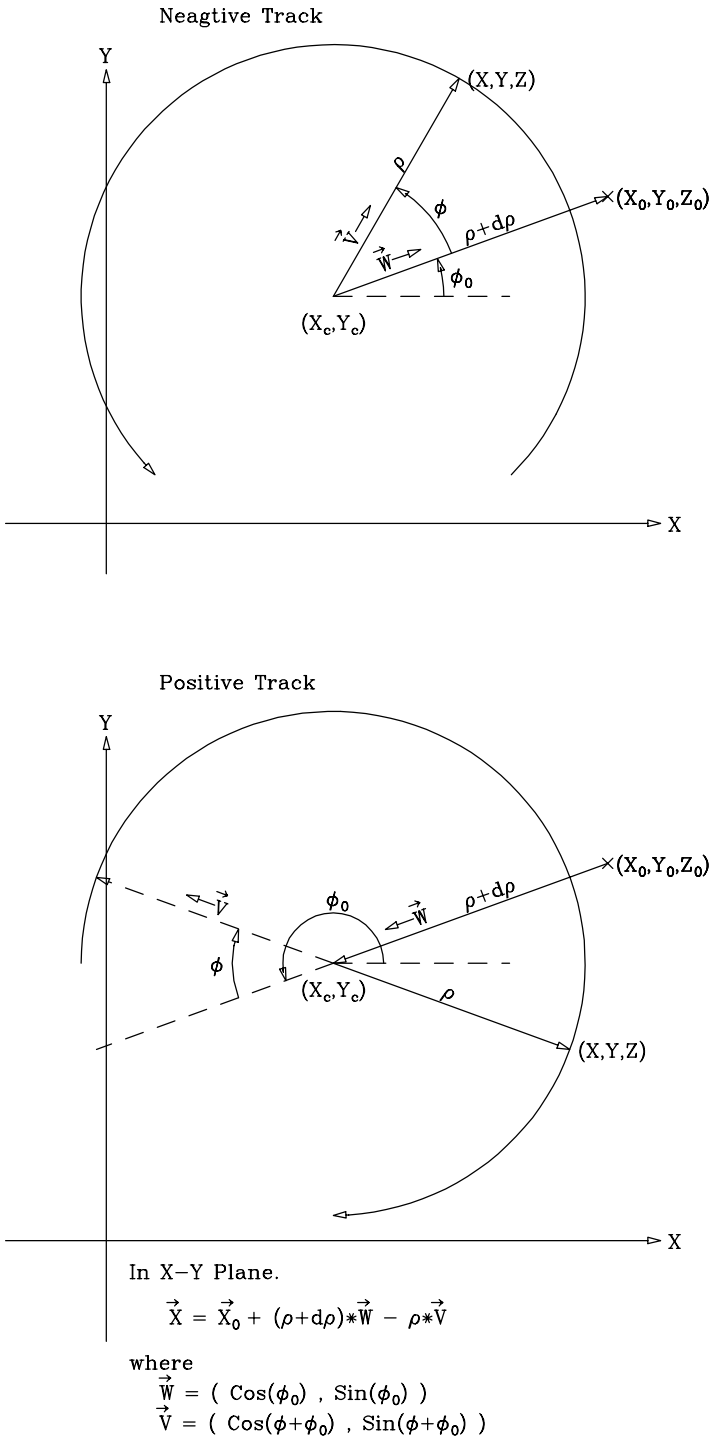

Figure C.4: The helix parametrization of the charged track by TPC.

Parameter	Description
X_0, Y_0, Z_0	position of the pivot
κ	inverse of the transverse momentum to the beam axis
$d\rho$	distance of the pivot from the true trajectory in the X-Y plane
dZ	distance of the pivot from the true trajectory along the Z-axis
ϕ_0	angle of the pivot from the true trajectory from the X-axis
λ	angle which track makes with the X-Y plane
α	constant to convert curvature to momentum
	$(=\frac{1}{cH})$; c : light velocity, H : magnetic field strength

Table C.1: The parameters in the helix function.

a low momentum track can be clustered in a bin as new a track candidate, The bins are tested in the same way as described above.

Track Refinement

After all tracks are found, the space points of each track are corrected for the distortions and re-fitted to a helix to assign the charge and the momentum to the track.

Although the gating grid prevents the feed-back of positive ions into the drift space and reduces the distortion in the electric field in the TPC, a small amount of distortion still remains resulting in the systematic shift in the space point determination. The dielectric material in the TPC, such as field cages, are also the source of the distortion.

In addition to the electro-static distortion, the spatial positions of TPC sectors may be deviated from the designed position. This also causes the shift in the determination of space points.

These displacements are parametrized in an empirical formula and the space points are corrected using the formula. The parameters in this formula were determined by the cosmic ray data.

Finally, the space points are fitted to a helix again to assign the charge and the momentum to the track. The momentum in the X-Y plane (P_T) and along Z-axis (P_L) are expressed using the helix parameters as

$$\begin{aligned} P_T &= |\frac{1}{\alpha\kappa}| \\ P_L &= P_T \cdot tan\lambda, \end{aligned}$$

where

$$\alpha \equiv \frac{1}{cH} = 333.56\ cm \cdot GeV^{-1}$$

c is the light velocity and H is the strength of magnetic field (=1.0 $Tesla$). The charge of the track is determined from the sign of κ.

The performance of the track reconstruction was studied by using the simulation. The tracking efficiency for hadronic events is 92.5% with no P_T cut and 94.2% with P_T cut at 0.2 GeV/c. The efficiency plateau did not reach 100% because of the sector boundaries and the shallow tracks as well as nearby tracks giving overlapping pad hits.

C.2.2 Cluster Reconstruction

Since the electromagnetic showers in the calorimeter, which were made by electrons, positrons and photons, explain in several counters, we can measure the energy deposits in these counters. In order to know the energy and position for incident particles, we have to reconstruct energy clusters from the energy deposit. In the following, we describe the reconstruction method for BCL, ECL and FCL.

Cluster Reconstruction for BCL

The raw data from BCL are digitized pulse heights from lead glass counters. In the reduction step, each digitized value is converted into energy deposit for each counter. These converted data are reconstructed to the energy and position data using following methods:

1. We searched the counter B_1 which have the largest deposit energy of E_1;

2. If the counter B_2 neighboring to B_1 had the deposit energy of E_2, it was added as the same cluster including B_1;

3. If the counter B_3 neighboring to B_2 with the deposit energy of E_3 satisfied the conditions:

$$E_2 > C_1 E_1$$

or

$$E_3 > C_2 E_1 \quad \text{and} \quad E_3 < C_3 E_2,$$

B_3 was considered to belong to the same cluster. Here C_1, C_2, and C_3 are constants optimized so that electrons and photons to be well reconstructed.

Using Monte-Carlo simulation, the constants were decided to be 0.65, 0.08, and 1.20 for C_1, C_2, and C_3, respectively.

The procedure was repeated for all counters with energy of greater than 45 MeV.

The average cluster position in Z-ϕ plane was determined by the energy-weighted mean of the counter positions:

$$X = \frac{\sum_i X_i \cdot E_i^p}{\sum_i E_i^p} \tag{C.2}$$

where X_i denotes the Z or ϕ coordinate of i-th lead glass counter defined at the front face, and E_i is the energy deposited in the i-th counter. The parameter p was optimized to be 0.26 and 0.34 for Z and ϕ, respectively, by the EGS4 simulation[48]. The r coordinate of the cluster was determined at the depth of the shower maximum with assuming the cluster to be a photon which coming from the interaction point.

Cluster Reconstruction for ECL

The raw data of ECL consist of digitized pulse heights counts of towers. In the reduction step, these digitized data are converted into deposit energies tower-by-tower. The clustering method for ECL is simpler than that of BCL.

1. Find the tower with the maximum energy deposit.

2. The towers within an angle of 0.16 *radian* around the highest tower are grouped into the same cluster of the highest one.

This procedure is repeated until all towers whose energy deposit are greater than 50 MeV are used.

The cluster position is determined by the same method as that of BCL, using eq.(C.2). Here, X_i is the coordinate of i-th tower in the θ-ϕ plane and the parameter p is set to be 1 for both the θ and ϕ directions.

Cluster Reconstruction for FCL

The raw data of FCL are the digitized pulse heights from BGO crystal and Si-strip detectors. They are converted into energy deposits in the reduction step. The clustering method is different from that for BCL and ECL. The consecutive BGO counters whose energy deposits are greater than $E_{threshold}$ are grouped in

the same clusters. The threshold energy $E_{threshold}$ is set to be 150 MeV, which is three times higher than the noise level.

The position of the BGO cluster is determined after BGO clustering. The procedure is as follows:

1. Find the BGO counter which has the maximum energy deposit.
2. Check the Si-strip hit in front of that BGO counter;
   (a) If there is no Si-strip hit, the center position of that BGO is given as the cluster position.
   (b) If there is only one Si-strip hit, its position is given as the cluster position.
   (c) If there are odd Si-strip hits, the position of the central strip is given as the cluster position.
   (d) If there are even Si-strip hits, the central two strips is used at random to determine the cluster position. The position of the cluster is the center value of (r, ϕ, Z), and their errors are determined by the width of the strip and the counter.

Bibliography

[1] S. Weinberg, Phys. Rev. Lett. **19** (1967) 1264.

[2] A. Salam, in Elementary Particle Theory, Relativistic Groups and Analyticity (Nobel Symp. No.8) (1968) 361.

[3] S. L. Glashow, Nucl. Phys. **B22** (1961) 1579.

[4] P. Aurenche et al., Prog. Theo. Phys. **92** (1994) 175.

[5] J.J.Sakurai and D.Schildknecht, Phys. Lett. **B40** (1979) 121, I.F.Ginzburg and V.G.Selbo, Phys. Lett. **B109** (1982) 231.

[6] S.J.Broadsky, T.A.DeGrand, J.F.Gunion and J.H.Weis. Phts. Rev. Lett. **41** (1978) 672, Phys. Rev. **D19** (1979) 1418, G.H.Llewellyn-Smith, Phys. Lett. **B79** (1978) 83, H.Terazawa, J. Phys. Soc. of Japan **47** (1979) 355, K.Kajanite and R.Raitio, Nucl. Phys. **B159** (1979) 528.

[7] PLUTO Collaboration Ch.Berger et al., Z. Phys. **C29** (1985) 499, Z. Phys. **C33** (1987) 351.

[8] TPC/2γ Collaboration H.Aihara et al., Phys. Rev. **D41** (1990) 2667.

[9] CELLO Collaboration H.J.Behrend et al., Z. Phys. **C51** (1991) 365.

[10] AMY Collaboration R.Tanaka et al., Phys. Lett. **B277** (1992) 215.

[11] AMY Collaboration B.J.Kim et al., Phys. Lett. **B325** (1994) 248.

[12] H1 Collaboration T.Ahmed et al., Phys. Lett. **B297** (1992) 205, ZEUS Collaboration M.Derrick et al., Phys. Lett. **B297** (1992) 404.

[13] M.Dress and R.M.Godbole, Nucl. Phys. **b339** (1990) 355.

[14] C.F. v. Weizsäcker, Z. Phys. **88** (1934) 612, E.J. Williams, Phys.Rev.**45** (1934) 729, for a recent treatment, see e.g. S.Frixione, M.L.Mangano, P.Nason and G.Ridolfi, Phys. Lett. **B319** (1993) 339, and references therein.

[15] L.E.Gordon and J.K.Storrow, Z. Phys. **C56** (1992) 307.

[16] M.Glück and E. Reya, Phys. Rev. **D28** (1983) 2749.

[17] E.Witten, Nucl. Phys. **B120** (1977) 189, R.J.deWitt, L.M.Jones, J.D.Sullivan, D.E.Willen and H.W.Wyld, Phys. Rev. **D19** (1979) 2046.

[18] G.Altareli and G.Parisi, Nucl. Phys. **B126** (1977) 298.

[19] H. Plothow-Besch, Comput. Phys. Commum. 75(1993)396

[20] T. Sjostrand, J. K. Storrow, A. Vogt, J. Phys. G22(1996)893.

[21] M.Dress and K.Grassie, Z. Phys. **C28** (1985) 451.

[22] M.Glück, E.Reya, A.Vogt, Phys. Rev. **D46** (1992) 1973.

[23] M.Glück, E.Reya, A.Vogt, Phys. Rev. **D48** (1990) 471.

[24] M.Glück, E.Reya, A.Vogt, Phys. Rev. **D53** (1992) 651.

[25] G.A.Schuler and T.Sjöstrand, Z. Phys. **C68** (1995) 607

[26] M.Dress, proceedings of the Aspen conference on Multiparticle Dynamics, Aspen, Colorado (1993) 110, and preprint MAD/PH/797.

[27] G.A.Schler and T.Sjöstrand, Nucl. Phys. **B407** (1993) 539.

[28] J.Chỳla, Phys. Lett. **B320** (1994) 186.

[29] G.A. Schuler and T. Sjostrand, CERN-TH/96-119, hep-ph/9605240.

[30] G.Kramer, S.G.Salesch, Phys. Lett. **B333** (1994) 519.

[31] M.Klasen, G.Kramer, Phys. Rev. **D56** (1997) 2702.

[32] M.H.Seymour, preprint RAL-97-026, `hep-ph/9707338`.

[33] S.G.Salesh, DESY report (December 1993) 196.

[34] M.Erdmann, The Partonic Structure of the Photon (Springer Tracts in Modern Physics 138) (1997) 57.

[35] H1 Collaboration, S.Aid et al., Z. Phys. **C70** (1996) 17.

[36] UA1 Collaboration, G.Arnison et al., Phys. Lett. **B132** (1983) 214.

[37] UA1 Collaboration, C.Albajar et al., Nucl. Phys. **B309** (1988) 405.

[38] TOPAZ Collaboration, H.Hayashii et al., Phys. Lett. **B314** (1993) 149.

[39] S.Söldner-Rembold, Proc. of the 28th International Conference on High Energy Physics, Warsaw, Poland (1996).

[40] TRISTAN project group, KEK Report 86-14 (1986).

[41] H.Hayashii et al., Nucl. Inst. and Meth. **A316** (1992) 202.

[42] K.Fujii et al., Nucl. Inst. and Meth. **A236** (1985) 55, J.Fujimoto et al., Nucl. Inst. and Meth. **A256** (1987) 449.

[43] S.Kawabata et al., Nucl. Inst. and Meth. **A270** (1988) 419.

[44] T.Kamae et al., Nucl. Inst. and Meth. **A252** (1986) 423.

[45] S.Noguchi et al., Nucl. Inst. Meth. **A271** (1988) 464.

[46] T.Tsukamoto et al., Nucl. Inst. and Meth. **A297** (1990) 148.

[47] K.Fujii et. al., KEK Preprint 87-24(1987).

[48] W.Nilson et al., SLAC-Report(1987)265.

[49] G.A.Schuler and T.Sjöstrand, Phys. Lett. **B300** (1993) 169.

[50] T.Sjöstrand, Com. Phys. Comm. **82** (1994) 74, T.Sjöstrand, Lund University report LU TP 95-20 (1995).

[51] R.Engel, University Siegen preprint 95-05.

[52] T.Sjöstrand, Com. Phys. Comm. **39** (1986) 347, T.Sjöstrand and M.Bengtsson, Com. Phys. Comm. **43** (1987) 367,

[53] T.Sjöstrand, Phys. Lett. **157B** (1985) 321, M.Bengtsson, T.Sjöstrand and M.Van.Zijl, Z. Phys. **C32** (1986) 67.

[54] M.Bengtsson and T.Sjöstrand, Phys. Lett. **B185** (1987) 435, Nucl. Phys. **B289** (1987) 810.

[55] C.Peterson, D.Schlatter, I.Schmitt and P.Zerwars, Phys. Rev. **D27** (1983) 105.

[56] R.Engel, Z. Phys. **C66** (1995) 203

[57] H.Fesefeldt, PITHA 85/02 (1985).

[58] E.Longo and L.Luminari, Nucl. Inst. Meth. **A239** (1985) 506.

[59] R.Itoh et al., IEEE Trans. on Nucl. Sci. **NS-34** (1987) 533.

[60] I.Adachi et al., Phys. Lett. **B234** (1990) 525.

[61] JADE Collaboration, W.Bartel et al., Zeit. Phys. **C33** (1986) 23, S.Bethke et al., Phys. Lett. **B213** (1988) 235.

[62] S.Catani, Yu.L.Dokshiser, M.Olsson, G.Turnock and B,R,Webber, Phys. Lett. **B269** (1991) 432.

[63] M.H.Seymour, Nucl. Phys. **B421** (1994) 545.

[64] S.Ellis, Z.Kunszt, D.E.Soper, Phys. Rev. **D40** 2188.

[65] S.Frixione, G.Ridolfi, preprint ETH-TH/97-21, GEF-TH-8/1997, `hep-ph/9707345`.

[66] S.Jadach, B.F.L.Ward amd Z.Was, Com. Phys. Comm. **66** (1991) 276.

[67] L.Lönnblad and M.Seymour (convenors), $\gamma\gamma Event Generators$, in "Physics at LEP2", CERN 96-01, Vol.2 (1996) 187.

[68] ZEUS Collaboration, M.Derrick et al., Phys. Lett. **B354** (1995) 163.

[69] K. Hagiwara,M. Tanaka, and I. Watanabe, Phys. Rev. **D51** (1997) 3197.